Operational Stability and Charge Transport in Fullerene-Based Organic Solar Cells

by

Quinn C. Burlingame

A dissertation submitted in partial fulfillment
of the requirements for the degree of
Doctor of Philosophy
(Electrical Engineering)
in The University of Michigan
2018

Doctoral Committee:

Professor Stephen R. Forrest, Chair
Professor L. Jay Guo
Professor Wei D. Lu
Professor Max Shtein

ORCID iD: 000-0002-4511-2271

qcb@umich.edu

For Bryn Marie

ACKNOWLEDGEMENTS

As I look back over the series of events that brought me to this dissertation, I'm overcome with gratitude to the people who have helped me along the way and I'm humbled by how lucky I've been. My thesis advisor Stephen Forrest has been a lodestar for me as a scientist and a thinker over the past 5 years. His mentorship and advice have been invaluable, and his humor and penchant for story telling made the time fly by.

Perhaps the best perk of working with Professor Forrest has been the remarkable group of lab mates I've been surrounded by during my time here. I'm particularly thankful for my cohort: Caleb Coburn, Yue Qu, Anurag Panda, Xiao Liu, Amy Che, Byeongseop Song, and Kan Ding who have been my dear friends and occasional collaborators during my time at the University of Michigan. I was lucky enough to have tremendous mentors in Jeramy Zimmerman, Michael Slootsky, Xiaoran Tong, and Nana Wang as a newly-minted Ph.D. student, and I've had the opportunity to teach and collaborate with a series of excellent undergraduate and graduate student mentees in Peter Su, Shahar Dror, Claire Arneson, Changyeong Jeong, Joosung Moon, Boning Qu, Lise Wei, Xiaheng Huang, and Hafiz Sheriff. I simply cannot count the number of wacky administrative issues Eva Ruff has helped me untangle over the past 5 years, and I'm grateful to her for copyediting this dissertation.

Years before my doctoral studies began, Professor Qiming Zhang went out of his way to give me an opportunity as a researcher in his group during my master's degree, and his students—particularly Shan Wu, Xinyu Li, and Xiaoshi Qian were incredible

friends and mentors to me during my early years as a graduate student. The friendly mentorship and guidance of Professor Chris Giebink was instrumental in charting my path into the world of organic optoelectronics and Professor Forrest's group.

Jeanne Hankett and Professor Zhan Chen were invaluable collaborators when studying the photochemical degradation of organic materials and Rasha Hamze and Professor Mark Thompson designed the compound proposed in Chapter VIII of this work. Vladimir Melnichak, Pilar Herrera-Fierro, Mike Manley, and Sean Campbell provided essential technical support for the experimental realization of this thesis. I am forever grateful to Professor Eugene Katz for enabling the outdoor and concentrated solar measurements in this work and for hosting me at his laboratory in Sede Boqer, Israel. I'm also thankful to Laura Ciammaruchi and Gloria Zanotti who were outstanding collaborators and hiking companions during my trip.

My family has been a source of unending support and love over the last 25 years of my education. To my wonderful grandmothers Margaret and Patrica, to my parents Philip and Susan, to my sister Katherine (and Jochanan), and to my in-laws Tim, Elona, Kelsey, Brad, Marie, Linda, and Robert—thank you. Finally, to my wife Bryn: this is for you. I'm so grateful to have you as a partner and a friend. None of this would exist without your love, patience, and understanding. I don't know what lies ahead as we enter the next chapter of our lives, but I look forward to finding out together.

TABLE OF CONTENTS

LIST OF FIGURES

Figure

LIST OF TABLES

Table

LIST OF ABBREVIATIONS

AFM atomic force microscopy

BIPV building integrated photovoltaics

CCD charge-coupled device

CCT correlated color temperature

CT charge transfer

CW continuous-wave

DI deionized

DSC differential scanning calorimetry

DSSC dye-sensitized solar cell

DFT density functional theory

EF-CBL electron-filtering compound buffer layer

EL electroluminescence

EQE external quantum efficiency

FF fill factor

FoM figure of merit

FTIR Fourier transform infrared

FWHM full width at half maximum

GDM Gaussian disorder model

GUI graphical user interface

HJ heterojunction

HOMO highest occupied molecular orbital

IoT internet of things

I.P. ionization potential

IPES inverse photoelectron spectroscopy

IR infrared

ISC intersystem crossing

J_{SC} short-circuit current

J–V current density–voltage

LCD liquid crystal display

L_D diffusion length

LDI-TOF laser desorption ionization time-of-flight

LED light emitting diode

LUMO lowest unoccupied molecular orbital

MPP maximum power point

ND neutral density

NIR near infrared

NMR nuclear magnetic resonance

NFA non-fullerene acceptor

OD optical density

OLED organic light emitting diode

OPA optical parametric amplifier

OPV organic photovoltaic

OVPD organic vapor phase deposition

PCB printed circuit board

PCE power conversion efficiency

PID proportional–integral–derivative

PL photoluminescence

PLQY photoluminescence quantum yield

PMHJ planar-mixed HJ

QCM quartz crystal microbalance

QD quantum dot

R2R roll-to-roll

RMS root-mean-square

SEM scanning electron microscopy

SMU source measurement unit

TCO transparent conducting oxide

$\boldsymbol{T_G}$ glass-transition temperature

TGA thermogravimetric analysis

TOF-SIMS time-of-flight secondary ion mass spectroscopy

UPS ultraviolet photoelectron spectroscopy

UV ultraviolet

UV-vis ultraviolet-visible

$\boldsymbol{V_{OC}}$ open-circuit voltage

VTE vacuum thermal evaporation

$\boldsymbol{WVTR}$ water vapor transmission rate

XRD x-ray diffractometry

XPS x-ray photoelectron spectrosopy

LIST OF CHEMICALS

3TPYMB *tris*[2,4,6-trimethyl-3-(pyridine-3-yl)phenyl]borane

Alq_3 tris-(8-hydroxyquinoline)aluminum

ATP adenosine triphosphate

BAlq bis(8-hydroxy-2-methylquinoline)-(4-phenylphenoxy)aluminum

BCP bathocuproine

BP4mPy 3,3',5,5'-tetra[(m-pyridyl)- phen-3-yl]biphenyl

BPhen bathophenanthroline

C_{60} fullerene carbon-60

C_{70} fullerene carbon-70

CIGS copper indium galium selenide

CuPc copper phthalocyanine

DBP tetraphenyldibenzoperiflanthene

DTDCPB 2-[(7-(4-[*N*,*N*-bis(4-methylphenyl)amino]phenyl)-2,1,3-benzothiadiazol-4-yl)methylene]propane-dinitrile

DTDCTB 2-((7-(5-(dip-tolylamino)thiophen-2-yl)benzo[c][1,2,5]thiadiazol-4-yl) methylene)malononitrile

FTO flourinated tin oxide

ITO indium tin oxide

IZO indium zinc oxide

P3HT poly(3-hexylthiophene-2,5-diyl)

Pc phthalocyanine

PC polycarbonate

$PC_{61}BM$ phenyl-C_{61}-butyric acid methyl ester

$PC_{71}BM$ phenyl-C_{71}-butyric acid methyl ester

PTCBI 3,4,9,10-perylenetetracarboxylic bisbenzimidazole

SubPc boron subphthalocyanine chloride

TPBi 2,2',2"-(1,3,5-benzenetriyl tris-[1-phenyl-1H-benzimidazole]

ABSTRACT

Organic photovoltaic cells are approaching commercially-viable levels of performance for a variety of applications—particularly those which make use of the unique transparency, flexibility, and ultra-thin form factor that organic solar cells can achieve. With state-of-the-art solar to electric power conversion efficiencies now exceeding 15%, operational stability of organic photovoltaics is perhaps their most significant remaining challenge, as the presence of intrinsic photochemical and morphological degradation modes have thus far limited device lifetimes to several years or months. Thermally evaporable fullerenes (C_{60} and C_{70}), with their remarkable optical and semiconducting properties, have enabled many of the most efficient and reliable organic photovoltaic cells over the past 15 years and remain central to state-of-the-art devices today.

After introducing the fundamentals of organic photovoltaic cell operation and characterization, this thesis focuses on the discovery and exploration of extremely long-range electron diffusion currents in fullerene-based organic heterostructures. It is shown that an energy barrier can be used to confine photogenerated electrons to a thin channel of C_{60} or C_{70}, where they can persist for several seconds. During this time, the electrons can diffuse laterally over centimeters, which allows for unprecedented study of charge diffusion processes in an organic semiconductor. Organic photovoltaic cells are demonstrated that make use of these channels to achieve high transparency by employing a C_{60} layer to collect and transport electrons to a sparse metal grid in

place of a conventional continuous metal electrode.

The remainder of this dissertation explores the reliability of fullerene-based organic solar cells by monitoring their performance during long-term aging, and studying the stability of the individual layers which comprise the cells. The performance of organic solar cells with planar C_{60} layers degrades rapidly under illumination, which is found to result from photo-oligomerization of adjacent C_{60} monomers. An analytical model based on reduced exciton diffusion length in the oligomerized C_{60} layer is developed to describe the device degradation, which fits the observed loss. Blending C_{60} with a second material and replacing C_{60} with C_{70} are both found to effectively stabilize photovoltaic performance.

The stability of blended tetraphenyldibenzoperiflanthene (DBP):C_{70}-based organic photovoltaics is found to follow the morphological stability of the device's non-photoactive cathode buffer layer. Stable cathode buffer layers based on 2,2',2"-(1,3,5-benzenetriyl tris-[1-phenyl-1H-benzimidazole] (TPBi):C_{70} are developed, which produce the most robust organic photovoltaics reported to-date. Even under constant simulated illumination at temperatures up to 130°C, no performance degradation is observed over more than 2500 hours. Under exposure to high intensity illumination (up to 37 suns equivalent), the devices degrade slowly, with an extrapolated outdoor lifetime of 54 ± 14 years.

CHAPTER I

Introduction

Optoelectronic semiconductor devices are now ubiquitous in applications from computing, lighting, and power generation to medicine and the arts. The active materials of these technologies are comprised almost entirely of inorganic semiconductors (Si, GaN, InP, etc.), which are inflexible, brittle, and opaque. Recently however, optoelectronic devices based on organic semiconductors have made significant inroads into commercial markets, and continue to be improved by a thriving global research community.[1] Unlike their inorganic counterparts, thin films of organic semiconductors can be deposited at low temperatures on flexible substrates, and can be made transparent. Owing to these advantages, organic light emitting diodes (OLEDs) are poised to overtake liquid crystal displays (LCDs) as the dominant information display technology, and organic photovoltaics (OPVs) are approaching market-viable levels of power generation performance for smart windows, building integrated photovoltaics (BIPV), and low-power internet of things (IoT) devices and may eventually become a cost-competitive technology.

To realize the promise of OPVs however, several key technological challenges remain. The three most critical of these are improving their solar-to-electric power conversion efficiency (PCE), extending device reliability, and scaling production to large area photovoltaic modules with high quality encapsulation via roll-to-roll (R2R)

processing. Thus far, efficiency has garnered significantly greater attention from the research community, resulting in decades of gradual improvement from $PCE \approx 1\%$ in 1986, when C.W. Tang (1986)[2] demonstrated the first OPV to $PCE > 15\%$ in 2018,[3,4] at the time of this writing. As a result, OPVs now rank among the most efficient thin-film solar cell technologies,[5] including dye-sensitized solar cells (DSSCs) ($PCE = 13\%$),[6] quantum dot (QD) solar cells ($PCE = 9.9\%$),[7] amorphous-Si cells ($PCE = 11.4\%$),[8] perovskite solar cells ($PCE > 22\%$),[9] copper indium galium selenide (CIGS) solar cells ($PCE > 21.7\%$),[10] and CdTe solar cells ($PCE > 21.5\%$). Solar cells based on crystalline inorganic semiconductors, such as Si ($PCE = 26\%$)[11] and GaAs ($PCE = 27.6\%$[5], $PCE = 28.9\%$ (Alta Devices)), remain significantly more efficient but are inflexible or expensive, and cannot be made semi-transparent like OPVs, which have so-far demonstrated near infrared (NIR) absorbing cells with *PCE*s greater than 7% with 43% visible transmittance.[12]

In terms of scalable production, small molecule OPVs have the advantage of leveraging the industrial success of OLED displays that require similar fabrication conditions. Indeed, OPVs are much simpler to pattern than OLEDs, which are comprised of micron-scale pixels. However, OPVs must also occupy much larger device areas than OLEDs, cost significantly less per unit area, and remain robustly encapsulated for years under exposure to the elements. In order to fabricate such large area devices on inexpensive substrates, R2R processing almost certainly must be employed. Fabrication of solution-processed R2Rs OPVs has been demonstrated at the laboratory-scale with modest *PCE*s[13,14] and by companies including *infinityPV* and *Konarka*. Vacuum-deposited R2R OPVs were recently demonstrated by B. Qu *et al.* (2018)[15] and have been commercially produced by *Heliatek*. Low-cost, reliable encapsulation of these R2R-fabricated cells remains a significant challenge for the commercialization of OPVs.[16]

The third pillar of OPV technology—operational stability, will be the focus of the

last six chapters of this thesis.

1.1 Fundamentals of organic photovoltaics

1.1.1 Organic molecules, solids, and semiconductors

Strictly speaking, an organic molecule is one that contains a chemical bond between carbon and hydrogen. This class of compounds spans a wide range of complexities as shown in Fig. 1.1, from simple monomers (e.g. tetracene), to polymers with many repeating units (e.g. poly(3-hexylthiophene-2,5-diyl) (P3HT)) and biological molecules (e.g. adenosine triphosphate (ATP), proteins, nucleic acids, etc.). A subset of these monomeric and polymeric compounds have been shown to have semiconducting electrical and optical properties conducive for integration into active optoelectronic devices such as OPVs,[2] OLEDs,[17] photodetectors,[18] and lasers.[19] This thesis will primarily focus on OPV cells comprised of monomers, which are often called small molecular weight organics or small molecules.

The unique properties of organic solids arise from their bonding. Strong covalent bonds join the atoms within each molecule, while molecules are bound to one another only through dipole-dipole and induced dipole (so-called van der Waals) interactions.

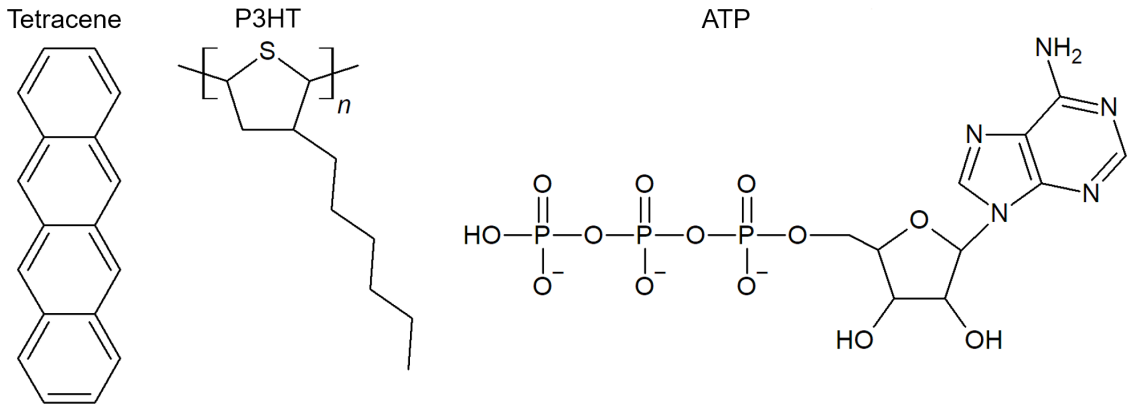

Figure 1.1: **Organic molecules with increasing complexity** | Molecular structural formulae of tetracene, P3HT, and ATP

Interaction between the atomic nuclei and valence electrons within each molecule produce spatially-distributed molecular electron orbitals with discrete energy levels. When the molecule is in its ground state, the highest energy molecular orbital that contains an electron is called the highest occupied molecular orbital (HOMO)—analogous to the valence band in inorganic semiconductors. The energy of the HOMO, E_{HOMO}, is typically referenced to the vacuum energy, E_{vac}, thus E_{HOMO} is equivalent to the ionization potential (*I.P.*) of the molecule. The energy level directly above the HOMO is the lowest unoccupied molecular orbital (LUMO), which contains no electrons when the molecule is in its ground state. The HOMO and LUMO comprise the frontier energy levels of the molecule, and are separated by a forbidden energy gap, E_g, as shown in Fig. 1.2.

As a result of these molecular orbitals and weak intermolecular interactions, organic molecules typically interact strongly with light (absorption coefficients $> 10^5$ cm^{-1}), melt/evaporate/sublime at low temperatures ($T < 300°C$), are poor charge conductors ($\mu < 10$ $cm^2V^{-1}s^{-1}$), and can be formed into flexible thin films. Furthermore, organics are often amenable to chemical modification, which allows for application-specific tuning of their properties.

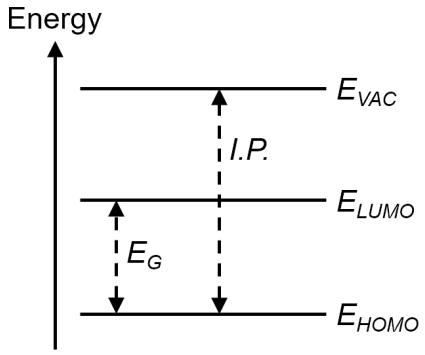

Figure 1.2: **Simplified molecular energy diagram** | Frontier energy levels of an organic molecule referenced to the vacuum energy

1.1.2 Excitons

An exciton is an excited electron-hole pair that is bound due to the Coulombic interaction between the constituent particles. In organic semiconductors, these quasiparticles are the primary species of excitation and energy transfer. If the hole is assumed to be fixed with respect to the electron, the exciton radius (a_0) and Coulombic binding energy (E_B) can be approximated using the Bohr model of a hydrogen atom:

$$a_0 = \frac{\epsilon_r \epsilon_0 \hbar^2}{q^2 m_e^*} \tag{1.1}$$

and

$$E_B = \frac{q^2}{4\pi\epsilon_r \epsilon_0 a_0}, \tag{1.2}$$

where ϵ_r is the relative dielectric constant of the medium at high frequency, ϵ_0 is the permittivity of vacuum, $\hbar$ is the reduced Planck constant, q is the charge of an electron, and m_e^* is the effective mass of the electron.

Compared with conventional inorganic semiconductors (e.g. Si, GaAs, InP, etc.), the high-frequency dielectric constant of organic semiconductors is low ($\epsilon_r \approx 3$), and the effective mass of electrons is high due to poor intermolecular coupling. As a result, their excitons are typically tightly bound ($E_B \approx$ 0.1-1 eV) and localized on a single molecule $a_0 < 1$, while the excitons in semiconductors with high polarizabilities and light effective masses delocalize over many lattice sites, and are typically unstable at room temperature as $E_B < k_B\mathrm{T} = 25.6$ meV where k_B is Boltzmann's constant and T = 300K. The tightly bound excitons found in organics are called Frenkel excitons or Frenkel states, while loosely bound excitons that delocalize over many lattice sites are called Wannier-Mott excitons. A third type of exciton called a charge transfer (CT) exciton is formed when the electron and hole occupy different molecules or lattice sites. While all excitons are charge neutral quasiparticles, CT excitons have a static dipole due to the persistent spatial separation of the electron and hole.

As electrons are fermions, their spin is $\frac{1}{2}$ with a projection onto the z-axis of either $\uparrow$ or $\downarrow$. Due to the Pauli exclusion principle, electrons are disallowed from occupying the same quantum state simultaneously. Thus the wavefunction, $\Psi(r_1, r_2)$, of a two-electron system such as an exciton must be anti-symmetric with respect to exchange of the particles *i.e.*, $\Psi(r_1, r_2) = -\Psi(r_2, r_1)$. This wavefunction can be broken into a spatial component, ψ, and a spin component, σ. Thus, for the total wavefunction to remain anti-symmetric, one of these components must be anti-symmetric and the other must be symmetric. Three of the possible spin states have a total spin of $S = 1$, and are symmetric under particle exchange. These states are called triplets:

$$Triplets\ (S=1) \quad \begin{cases} \Psi(r_1, r_2) = \psi_{anti-sym} \times \sigma_\uparrow(1)\sigma_\uparrow(2) \\ \Psi(r_1, r_2) = \psi_{anti-sym} \times \sigma_\downarrow(1)\sigma_\downarrow(2) \\ \Psi(r_1, r_2) = \psi_{anti-sym} \times \frac{1}{\sqrt{2}}[\sigma_\uparrow(1)\sigma_\downarrow(2) + \sigma_\downarrow(1)\sigma_\uparrow(2)] \end{cases} . \quad (1.3)$$

A fourth anti-symmetric spin state with $S = 0$ is called the singlet:

$$Singlet\ (S=0) \quad \begin{cases} \Psi(r_1, r_2) = \psi_{symmetric} \times \frac{1}{\sqrt{2}}[\sigma_\uparrow(1)\sigma_\downarrow(2) - \sigma_\downarrow(1)\sigma_\uparrow(2)] \end{cases} . \quad (1.4)$$

The molecular ground state, denoted S_0, is inherently a singlet state as the outermost valence electrons share the HOMO, and must therefore have different spin projection directions. It follows that optical excitation produces mostly singlet excitons. Optical transitions between S_0 and triplet excitons are possible in systems with strong spin-orbit coupling,[20] but they are not a significant source of excitation in OPVs. More commonly, triplets are formed by intersystem crossing (ISC) from singlet excitons with a characteristic rate k_{ISC}. Similarly, fluorescent emission from singlet excitons occurs with a much faster rate, k_F, than phosphorescent emission from triplet excitons, k_{PH}. Efficient phosphorescent emitters therefore require that $k_{ISC} > k_F$. Figure 1.3 shows the transition rates between the first excited singlet

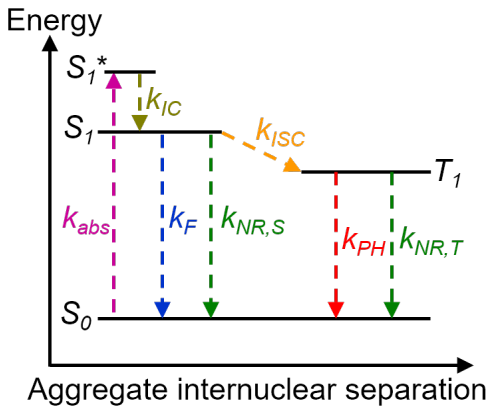

Figure 1.3: **Excitonic state diagram** | Transfer rates between the excited singlet (S_1), a higher energy vibronic of the first excited singlet (S_1^*), triplet (T_1), and ground states (S_0) are shown.

(S_1), a higher energy vibronic of the first excited singlet (S_1^*), triplet (T_1), and S_0 including the rate of absorption, k_{abs}, internal conversion, k_{IC}, and the non-radiative recombination rates of singlets ($k_{NR,S}$) and triplets ($k_{NR,T}$).

To form a more complete picture of the electronic transitions observed in organic systems, the coupling between electronic states and the vibrational modes of the molecule must be considered. This interaction creates energetically discrete eigenstates within each singlet/triplet manifold called vibronic modes, as shown in Fig. 1.4. Electrons in higher energy vibronics rapidly thermalize to the $\nu = 0$ vibronic through internal conversion with a rate, k_{IC}, as shown in Fig. 1.3). As a result, electronic transitions originate almost exclusively from the $\nu = 0$ vibronic in accordance with Kasha's rule. However, transitions into higher energy vibronics can be strong, even stronger than the $0 \rightarrow 0$ transitions in some cases, which gives rise to the multiple peaks in the absorption and emission spectra shown in Fig. 1.4. Finally, electronic transitions are much faster than nuclear reconfiguration, thus the electronic transitions are vertical in Fig. 1.4. Electronic transitions can therefore only occur if the initial molecular configuration is also capable of supporting the final state.

In addition to optical generation, excitons can be formed by electron/hole recom-

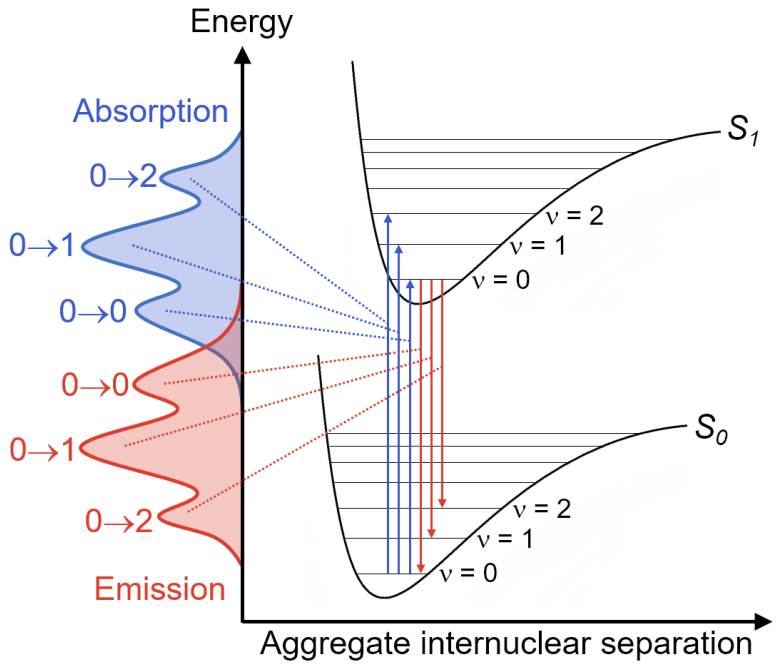

Figure 1.4: **Vibronic state diagram of a singlet and its ground state** | The first three electronic transitions in absorption (blue) and emission (red) are shown, along with an illustration of an absorption/emission spectrum they might form on the left. The first three vibronic levels, $\nu = 1, 2, 3$ are labeled in each manifold.

bination, as is the case in OLEDs where the two charge species are injected from opposite contacts. Since the spins of the two charges are random after electrical injection, three triplets are formed for every singlet in accordance wit spin statistics.[21] Excitons can also be generated thermally and by collision with high energy particles, such as electrons under high electric field, and by high intensity radiation, such as x-rays, γ-rays, α particles, and β particles. Organic semiconductors, such as anthracene and pentacene, have long been employed as scintillators due to their sensitivity to radiation, strong fluorescence, and robustness.[22]

1.1.3 Exciton transfer

Excitons have several mechanisms by which energy can be transferred from one molecule, called a donor, to another molecule, called an acceptor. In the near field ($\sim 3-10$ nm), an exciton can transfer its energy to an unexcited molecule via dipole-

dipole coupling, which is called Förster transfer.[23] Förster transfer has a characteristic Förster radius, R_0:

$$R_0 = \left[\frac{3\Phi_{PL}}{4\pi} \int \left(\frac{\hbar c}{nE} \right)^4 F_D(E)\sigma_a(E)dE \right]^{1/6}, \tag{1.5}$$

and characteristic transfer rate, $\Gamma_{D\to A}$:

$$\Gamma_{D\to A} = \frac{1}{\tau_D} \left(\frac{R_0}{r_{DA}} \right)^6, \tag{1.6}$$

where τ_D is the fluorescence lifetime of the donor, r_{DA} is the separation between the two molecules, Φ_{PL} is the photoluminescence quantum yield (PLQY) of the donor, c is the speed of light, n is the refractive index of the medium, E is energy, F_D is the normalized donor fluorescence spectrum, and σ_A is the normalized acceptor absorption cross section. Förster transfer is therefore maximized when the donor emission and acceptor absorption overlap strongly, indicating resonance.

Excitons can also be transferred to neighboring molecules through simultaneous exchange of electrons between the HOMO and LUMO of the donor and acceptor molecules, as described by D.L. Dexter (1953).[24] The electron exchange rate depends on the strength of coupling between the initial and final states, and can thus the Dexter transfer rate, $\Gamma_{exchange}$, can be written using Fermi's Golden Rule:

$$\Gamma_{exch} = \frac{2\pi}{\hbar} |V_{exch}|^2 \int F_D(E)\sigma_a(E)dE, \tag{1.7}$$

where V_{exch} is the so-called matrix element for the interaction:

$$V_{exch} = \frac{1}{4\pi\epsilon_0\epsilon_r} \int \psi_D(1)\psi_A^*(2)\frac{1}{r_{DA}}\psi_D^*(2)\psi_A(1)d\nu. \tag{1.8}$$

Here, ψ_D and ψ_A are the spatial wavefunctions of an electron on the donor or acceptor

with * indicating that they are excited, and the spin wave functions are omitted for simplicity. Since spin of the system must be conserved and the ground state of both molecules is a singlet, the transferred exciton retains the spin of the original exciton (*e.g.*, triplet→triplet or singlet→singlet). Dexter exchange is the most prevalent mechanism for triplet exciton transport and occurs almost entirely between nearest neighbor molecules as the electron wavefunction overlap falls off exponentially with distance.

Excitons can also be transferred through photon emission and re-absorption, so-called trivial transfer. Such transfer can occur over very long distances, and is most common in systems where a dilute emitter is dispersed in a host matrix with a larger energy gap. Finally, an exciton can couple to a neighboring molecule in the near-field, via coherent transfer in the case when the electron-phonon coupling energy, ΔE_{e-p}, is much less than the interaction potential, V_{int}, between the two molecules. Coherent transfer is known as the strong-coupling limit, and occurs on a timescale faster than molecular relaxation with a rate, $k_{D\rightarrow A}$:

$$k_{D\rightarrow A} \approx \frac{4V_{int}}{\hbar}. \tag{1.9}$$

In reality, coherent transfer rarely occurs in organic systems, because electron-phonon coupling is strong compared to the interaction between molecules, *i.e.*, $\Delta E_{e-p} \gg V_{int}$.

The aggregate result of these exciton transfer processes is that excitons are able to diffuse in bulk organic semiconductors until they recombine, either by emitting a photon or through non-radiative processes. The diffusion behavior of excitons can be modeled as a function of position, r, and time, t, such that:

$$\frac{\partial N(r,t)}{\partial t} = D\nabla^2 N(r,t) - \frac{N(r,t)}{\tau} + G(r,t), \tag{1.10}$$

where $N(r,t)$ is the exciton concentration, D is the exciton diffusivity, and τ is the

natural recombination lifetime. In steady-state, this equation simplifies to:

$$\frac{N(r)}{\tau} = D\nabla^2 N(r) + G(r). \tag{1.11}$$

It is useful to define the exciton diffusion length (L_D):

$$L_D = \sqrt{D\tau}, \tag{1.12}$$

which is the radius of the average spherical volume an exciton will traverse prior to recombination.

1.1.4 Polarons and mobility

In low electron mobility organic semiconductors, electron motion is slow compared to intramolecular and intermolecular vibrations. The host molecule and surrounding lattice therefore have time to adjust to the Coulombic potential of the charge, and relax to a lower energy configuration before the electron moves. This relaxation produces a polarization field surrounding the carrier that lowers its energy, thus the charge is self-trapped. The aggregate quasiparticle formed by the charge and the polarized region that surrounds it is called a polaron. In organic semiconductors, hole polarons in the HOMO and electron polarons in the LUMO are analagous holes and electrons in the valence and conduction bands of conventional semiconductors, and are the primary conductors of charge.

Since polarons are localized to a single molecule, they must escape the potential well of their host molecule to be transferred. The height of this energy barrier is dictated by the shape of the potential wells and distance between the molecules, as shown in Fig. 1.5. Additionally, the self-trapping potential from the polarization field lowers the energy by $\approx$ 100 meV, making electron transfer endothermic (*i.e.*, $\Delta G < 0$) when no field is applied, as shown in Case 1 in Fig. 1.5. Applying an

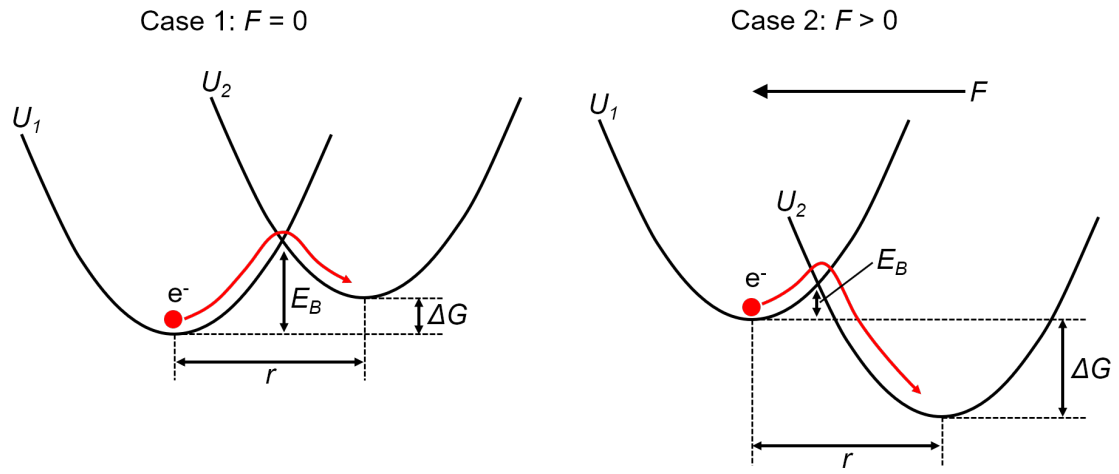

Figure 1.5: **Intermolecular charge transfer diagram** | Potential energy surfaces, U_1 and U_2, of two adjacent molecules with and without an externally applied electric field, F. The change in Gibbs free energy between the initial and final state, ΔG, intermolecular distance, r, and energy barrier for electron transfer, E_B, are shown for each.

external electric field significantly lowers E_B as shown in Case 2 in Fig. 1.5, and increases ΔG by qFr, where q is the charge of an electron, F is the magnitude of the field, and r is the spacing between the molecules. It follows that charge diffusivity, D, will be thermally activated with an activation energy equal to E_B:

$$D = D_0 \exp\left(\frac{-E_B}{k_B T}\right), \tag{1.13}$$

where D_0 is a constant related to the hopping attempt frequency and width of the barrier. Using the Einstein relation:

$$\frac{D}{\mu} = \frac{k_B T}{q}, \tag{1.14}$$

the electron mobility, μ, can be written in a similar form:

$$\mu = \mu_0 \exp\left(\frac{-E_B}{k_B T}\right), \tag{1.15}$$

where μ_0 is a constant.

In general though, this mobility expression is too simple as E_B and μ are dependent on the electric field. Barrier lowering, ΔE_B, due to the presence of an electric field is described by the Poole-Frenkel effect:

$$\Delta E_B = \left(\frac{q^3 F}{\pi \epsilon_r \epsilon_0} \right)^{1/2}. \tag{1.16}$$

Thus:

$$\mu(F,T) = \mu_0 \exp\left(\frac{-E_B + \Delta E_B}{k_B T_{eff}} \right) \quad for\ T > T_0, \tag{1.17}$$

where $\frac{1}{T_{eff}} = \frac{1}{T} - \frac{1}{T_0}$, since W.D. Gill (1972)[25] found experimentally that $\mu(F,T)$ vs.$\frac{1}{T}$ curves at different fields intersected each other at a finite temperature, T_0. Equation 1.17 breaks down as $T \to T_0$, since it incorrectly implies that F effectively increases the barrier height at low temperatures.

Furthermore, organic semiconductors are typically disordered due to the dynamic thermal motion and static configurational differences of each molecule in the film. This disorder can be approximated using the Gaussian disorder model (GDM), which assumes the density of LUMO/HOMO sites is Gaussian in energy:[26,27]

$$\sigma(E) \approx \frac{1}{\sqrt{2\pi\sigma_D^2}} \exp\left(\frac{-E^2}{2\sigma_D^2} \right), \tag{1.18}$$

where $\sigma(E)$ is the distribution of site energies and σ_D is the distribution half-width, as shown in Fig. 1.6. At low carrier densities, sites in the low energy tail of the distribution are occupied in accordance with Fermi-Dirac statistics. Since these low energy sites are sparsely distributed in space, they act as shallow charge traps. The mobility of disordered systems therefore appears low when only small amounts of charge are present and increases as the tail states are filled. Under this condition, the Einstein relation (eq. 1.14) no longer holds,[28] and it is typically found experimentally

that $D > \frac{k_B T}{q}\mu$.

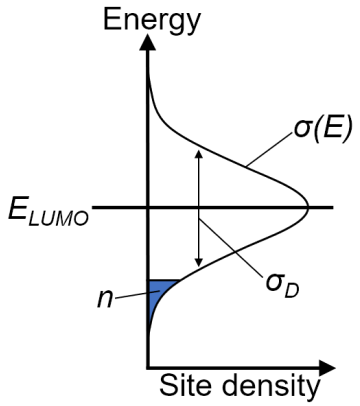

Figure 1.6: **Gaussian disorder model illustration** | Depiction of energetic disorder in the LUMO of an organic semiconductor, according to the GDM. The low energy tail of the distribution is filled with a charge density n.

1.1.5 Energy diagrams

Organic semiconductor devices are often comprised of many organic layers with different functions and energetics. Simplified energy diagrams that show the approximate relationships between these layers can provide valuable insight into device operation. Typically, device diagrams consist of vertical rectangles for each compound arranged side by side to show the layer structure. The bottom line of each rectangle represents the energy of the HOMO with respect to the vacuum energy, E_{Vac}, and the top line represents the energy of the LUMO. Layers comprised of two or more compounds blended together are typically shown as overlapping. Conductive contacts, such as metals, are typically shown as a single line that indicates their Fermi level ($E_{F,M}$), equal to their work function referenced to E_{Vac}. A sample energy diagram that demonstrates these elements is shown in Fig. 1.7. The HOMO energies in such diagrams are typically measured using ultraviolet photoelectron spectroscopy (UPS) unless otherwise noted. The LUMO energies are most often estimated from the "optical gap" of the organic, which is taken to be the low energy

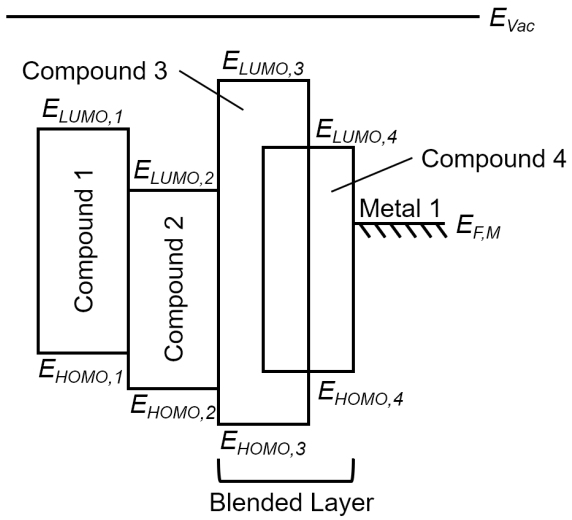

Figure 1.7: **Representative organic device energy diagram** | Energy levels of a device with two neat organic layers (Compound 1 and Compound 2), a blended layer comprising Compounds 1 and 2, and a metal contact.

cutoff of the absorption spectrum. Alternately, LUMO energies are sometimes found from density functional theory (DFT) simulations and from measurements such as inverse photoelectron spectroscopy (IPES) and cyclic voltammetry. However, none of the techniques for measuring LUMO have particularly high resolution ($\sim$500 meV). In addition, excitons and polarons have significant binding energies and, thus do not sit at the measured HOMO/LUMO energies.

While energy diagrams are typically drawn using measurements from neat materials, the situation in reality may be quite different. Once in contact with one another, charges will redistribute and interface dipoles can form between layers.[29] These processes can shift the energy levels significantly, particularly in blended systems.[30,31] Due to the low intrinsic charge densities in organics, they are easily depleted. Placing contacts with dissimilar work functions on either side of an organic semiconductor, as shown in Fig. 1.8, will therefore create a uniform internal field, F_{int}, with magnitude:

$$F_{int} = \frac{\phi_{M,1} - \phi_{M,2}}{d} \tag{1.19}$$

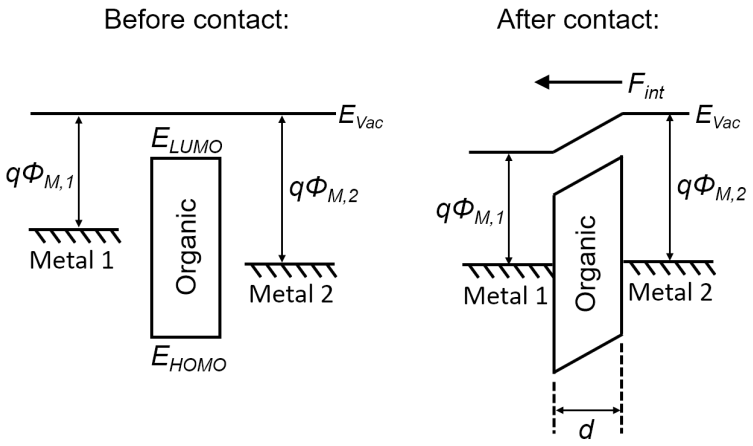

Figure 1.8: **Metal-organic energy level diagram** | Energy level alignment of two metals sandwiching an organic layer before and after contact. The difference in work function of the two metals ($\phi_{M,1} - \phi_{M,2}$) produces an internal field, F_{int}, in the organic layer.

where $\phi_{M,1}$ and $\phi_{M,2}$ are the work functions of the two metals, and d is the thickness of the organic layer. A similar uniform voltage drop across the organic layers is observed upon application of an external voltage.

1.1.6 Organic heterojunctions

Manipulating energy transfer and charge flow in organic semiconductor devices can be achieved by creating an interface between dissimilar materials, called a heterojunction (HJ). There are three basic types of HJ delineated by the relationship between the energy levels of the two semiconductors, as shown in Fig. 1.9. One of the materials in a so-called Type-I HJ is wider bandgap than the other, with a deeper HOMO and shallower LUMO. Type-I HJs therefore block electron, hole, and exciton transfer into the wide bandgap material, and can be used to confine those species to a particular layer of the device. Type-II HJs have staggered energy levels, and thus block electron transfer in one direction and hole transfer in the other. Excitons that reach a Type-II HJ see a barrier for one of the charges, and an energetically favorable transfer for the other. These HJs can therefore be used to dissociate excitons, such that the

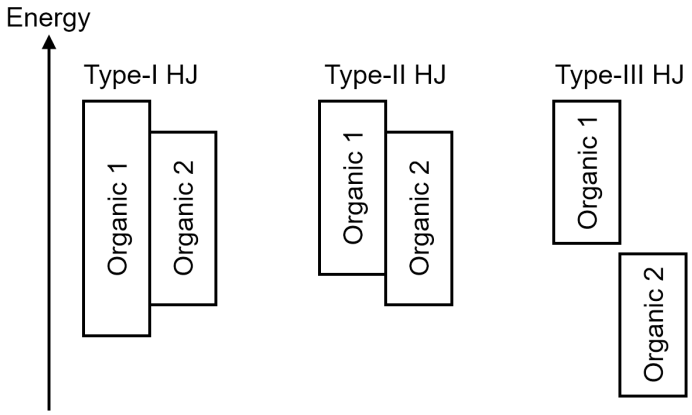

Figure 1.9: **Types of organic HJ** | Energy diagrams of Type-I (embedded gap), Type-II (staggered gap), and Type-III (broken gap) heterojunctions.

electron and hole occupy different molecules, which forms a CT state. By convention, the material with the shallower HOMO and LUMO in a Type-II organic HJ is called a donor since it preferentially donates electrons to the other molecule, called an acceptor. Type-II HJs are often called donor-acceptor HJs, abbreviated D/A HJ if the interface is planar or D:A HJ if the donor and acceptor are blended together. Type-III HJs have no energetic overlap between the two materials as shown in Fig. 1.9.

1.1.7 Theory of organic photovoltaic operation

Photocurrent generation in organic photovoltaics occurs in several steps, as shown in Fig. 1.10. First, photons are absorbed by the photoactive materials in the OPV, forming a population of excitons in the donor and acceptor. Absorption can be quantified with an efficiency, η_{abs}, equal to the number of excitons formed per incident photon. The excitons then diffuse until they reach the donor-acceptor HJ, with an efficiency η_{diff}. One of the charges in the exciton then transfers to the other molecule, with an efficiency η_{CT}. In the case of excitons formed in the donor, the electron will transfer to the acceptor, while excitons formed in the acceptor will transfer their hole to the donor. The photogenerated CT states then dissociate into free polarons that

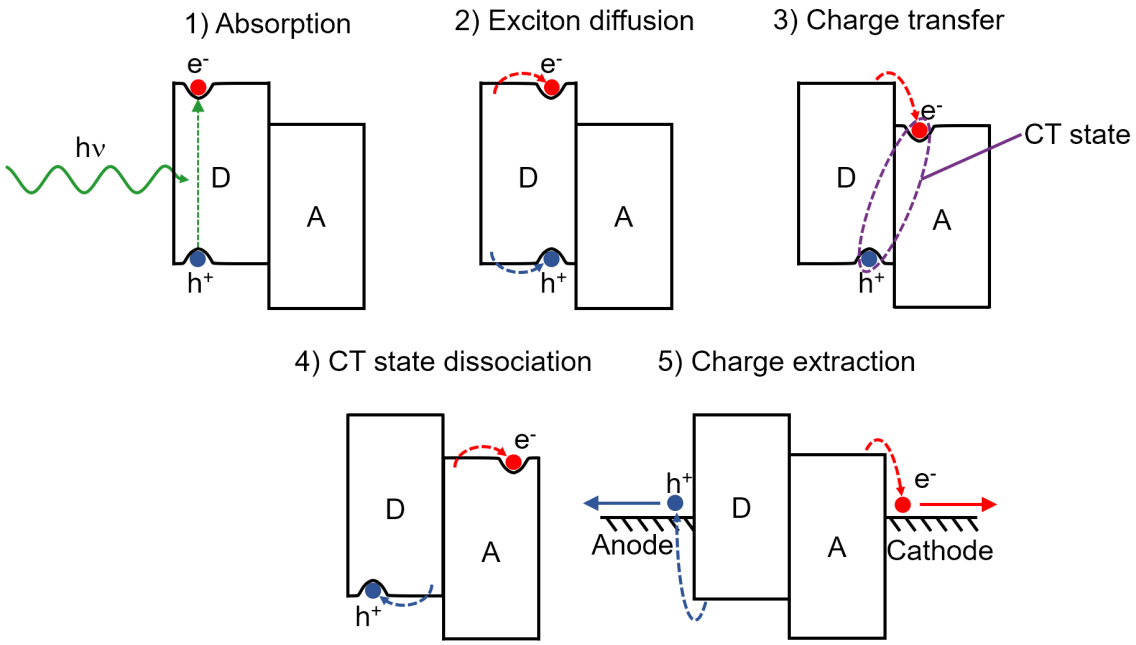

Figure 1.10: **Theory of OPV operation** | Illustration of the successive processes that lead to photocurrent generation in organic photovoltaics.

are no longer Coulombically bound to one another at the HJ. This dissociation has an efficiency, η_{diss}. Finally, the polarons are transported through the organic layers until the holes reach the anode and the electrons reach the cathode.

The product of all of these efficiencies is called the external quantum efficiency (EQE), which is defined as the number of electrons extracted per incident photon:

$$\eta_{EQE} = \eta_{abs}\eta_{diff}\eta_{CT}\eta_{diss}\eta_{ext}. \tag{1.20}$$

The constituent efficiencies, and thus η_{EQE}, may vary as a function of intensity, applied voltage, temperature, and wavelength of the incident light. Most commonly, however, EQE is reported as a function of wavelength.

In order for a photovoltage to be formed and for the photocurrent to be directional, the spatial distribution of photogenerated electrons and holes in OPVs must be different under steady-state. This can be accomplished by using asymmetric contacts or charge blocking layers. Typically, a low work function electrode is used as the

cathode (electron collecting contact), while a high work function electrode is used as the anode (hole collecting contact). The work function offset between the electrodes produces an internal field in the device, as shown in Fig. 1.8 that drives photogenerated holes and electrons in opposite directions. Energy barriers, in the form of charge blocking layers and selective contacts, can also ensure uni-directional currents by restricting the flow of one charge or the other.

1.1.8 Device architectures

The active materials required to construct an OPV cell can be broadly divided into four categories as shown in Fig. 1.11: substrates, electrodes, photoactive materials, and buffers. Substrates are typically glass or plastic and provide mechanical support for the thin OPV deposited on top. Ideally, substrates are highly transparent to ensure that the maximum amount of light reaches the photoactive layers, impermeable to atmospheric H_2O and O_2, and can be manufactured at low cost.

The electrodes are used to collect charge from the device and produce an inter-

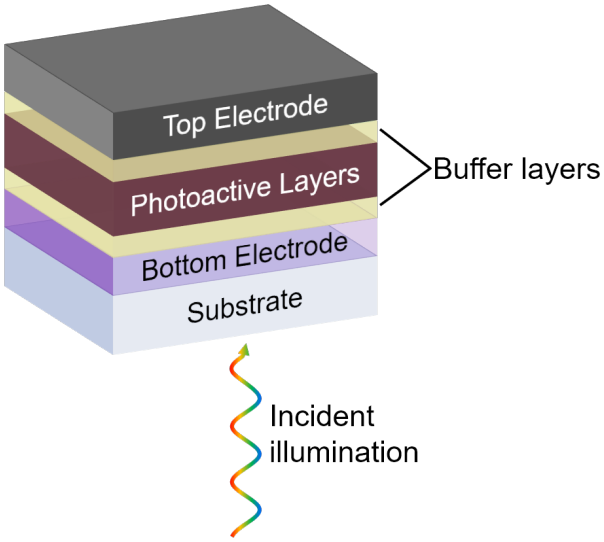

Figure 1.11: **Simplified OPV device structure** | The basic components of an organic photovoltaic: the substrate, bottom electrode, top electrode, and photoactive layers that may or may not be sandwiched by buffer layers for the purpose of charge manipulation or exciton blocking.

nal field as discussed in §1.1.7. One of these electrodes (the bottom electrode in Fig. 1.11), must be as transparent as possible. Most commonly, this electrode is a transparent conducting oxide (TCO) such as indium tin oxide (ITO), indium zinc oxide (IZO), or flourinated tin oxide (FTO). The thickness of the TCO controls both its resistance and transparency, and should thus be optimized to achieve the best trade off for a particular device. Many novel approaches to replace conventional TCOs are under development, including metal nanowire grids/meshes/composites,[32–34], thin metal alloys,[35] carbon nanotubes,[36,37] and graphene.[38,39] Since resistive power loss is proportional to I^2R, large area devices are particularly sensitive to the resistivity of the bottom electrode, and may require metallic busbars or sub-electrodes in conjunction with the transparent electrode to extract current.[40] Conventionally, the opposite electrode (the top electrode in Fig. 1.11) is highly reflective, thus light that reaches the electrode is reflected back into the photoactive layers for absorption. Metals such as Ag and Al make excellent reflective electrodes due to their low absorption and high conductivity. However, semi-transparent top electrodes are being increasingly utilized for semi-transparent OPVs.[12,41,42] In cases where the top contact is the cathode, a low work function is desirable to maximize the internal field and to efficiently extract electrons from the LUMO of the acceptor.[43]

The photoactive layers of the OPV are responsible for absorbing light and dissociating the resulting excitons into free polarons. The first successful bilayer OPVs by C.W. Tang (1986)[2] employed a planar Type-II D/A HJ with copper phthalocyanine (CuPc) as the donor and PTCBI as the acceptor. Planar D/A HJ OPVs dominated the field until 1995, when G. Yu *et al.*[44] and J. J. M. Halls *et al.*[45] introduced a bulk D:A HJ OPV where the donor and acceptor were mixed together. Planar HJ OPVs require that excitons diffuse through continuous domains of the acceptor and donor to reach the HJ for dissociation. The thickness of the donor and acceptor layers are therefore limited by the exciton L_D, such that η_{diff} in Eq. 1.20 re-

mains high. However, once excitons are dissociated at the planar HJ, each charge has a continuous extraction pathway that is spatially separated from its counter charges. This limits recombination, and improves the conductivity, thus η_{ext} is high. In contrast, the HJ in mixed HJ OPVs is distributed throughout the photoactive region. Excitons therefore reach the D:A HJ with little or no diffusion ($\eta_{diff} \approx 100\%$), and the photoactive region can be made thicker to increase absorption. Unlike the planar D/A HJ, however, the charges in the blend must traverse interpenetrating donor and acceptor domains that are not spatially separated. The probability of charges reforming CT states and recombining along the D:A interface is therefore higher than in planar devices. Since the chance of recombination increases with photoactive layer thickness, HJ OPVs must be optimized to find the ideal trade off between absorption and charge collection. A hybrid architecture called a planar-mixed HJ (PMHJ)[46] employs a mixed HJ in contact with neat layers of the donor and/or acceptor. Schematics of these three photoactive region architectures are shown in Fig. 1.12. Photoactive regions incorporating more than two components have also been demonstrated, but are outside the scope of this thesis.[47,48]

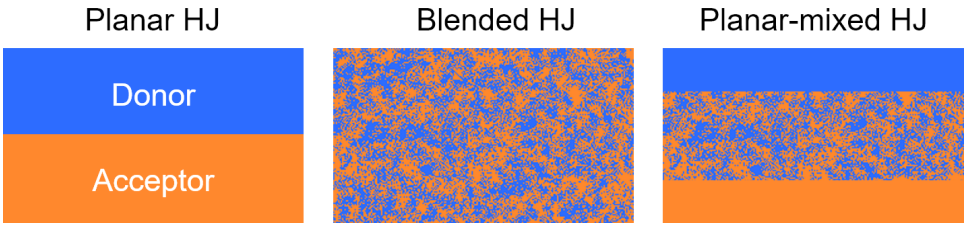

Figure 1.12: **Two-component OPV HJ architectures.**

Here, buffers or buffer layers refer to materials between the electrodes that are not photoactive. Buffer layers can be organic or inorganic (MoO_3, for example) and serve many different purposes within an OPV, such as electrode work function modification, charge extraction, charge blocking, charge injection, exciton blocking, and protection against subsequent depositions. Cathode buffer layers are a critical component in modern OPVs, as they confine excitons to the photoactive region, prevent the cathode

metal penetration into the device, and facilitate electron extraction. This can be accomplished simply with a thin neat layer of a wide energy gap exciton blocking material, as illustrated in Fig. 1.13. To improve the charge extraction efficiency and conductivity, some of the acceptor (for example C_{60} or C_{70}) can be blended into the wide bandgap material to form an electron-filtering compound buffer layer (EF-CBL).[49,50] Since electrons experience the internal field of the device, as shown in Fig. 1.13, they are forced through the buffer. Excitons, on the other hand, are charge neutral and the density of states they can occupy in the pure acceptor region is higher than it is in the EF-CBL. So while they may penetrate into the EF-CBL, they will typically diffuse back into the neat acceptor and, eventually, the HJ to generate photocurrent.[51]

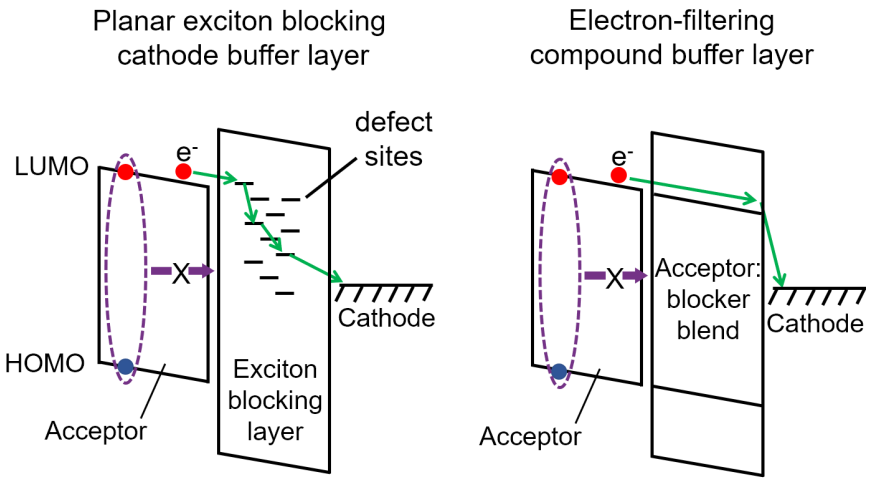

Figure 1.13: **OPV cathode buffer layer architectures** | Left: a planar cathode buffer layer comprised of a wide energy gap exciton blocking material. Right: an EF-CBL with the exciton blocking material and acceptor blended together. Electrons are conducted through the acceptor sites in the blend, while excitons are blocked.

1.1.9 Current-voltage characteristics

Electrically, OPVs behave similarly to inorganic *p*-*n* junction diodes that follow the ideal diode equation:

$$J = J_S \left[\exp\left(\frac{qV_A}{mk_BT} \right) - 1 \right] - J_{ph}. \tag{1.21}$$

Here, V_A is the applied voltage, m is the ideality factor, J_{ph} is the photocurrent, and J_S is the reverse bias saturation current:

$$J_S = q \left[\frac{D_p n_i^2}{L_p N_D} + \frac{D_n n_i^2}{L_n N_A} \right], \tag{1.22}$$

where D_p and D_n are the hole and electron diffusivities, L_p and L_n are the minority carrier diffusion lengths of holes and electrons, and N_A and N_D are the density of *p*-type and *n*-type dopants. Equation 1.21 can be derived by solving for the properties of the depletion region and solving for the carrier densities and currents in the quasi-neutral region of the diode to produce the total current.

While the current density–voltage (J–V) characteristics of OPVs are superficially similar to Eq. 1.21, the underlying physics are quite different. N.C. Giebink *et al.* (2010)[52,53] developed a theory to predict the J–V characteristics of organic HJs by considering that CT states across the HJ mediate the transfer between excitons, polarons, and the unexcited ground state. This treatment recovers the exponential J–V relationship observed in Eq. 1.21, and can be expressed as:

$$J = J_{S,0} \left[\exp\left(\frac{qV_A}{mk_BT} \right) - \frac{k_{CT,diss}}{k_{CT,diss,eq}} \right] - q \int \eta_{EQE}(\lambda)\Phi(\lambda)d\lambda, \tag{1.23}$$

in the absence of traps. Here, m is the ideality factor, $k_{CT,diss}$ and $k_{CT,diss,eq}$ are the present and equilibrium CT state dissociation rates, η_{EQE} is the quantum efficiency from Eq. 1.20, Φ is the photon flux incident on the device, and $J_{S,0}$ is the dark

saturation current:

$$J_{S,0} = qa_0(1 - \eta_{diss})k_{rec}N_{HOMO}N_{LUMO}\exp\left(\frac{-\Delta E_{HL}}{k_BT}\right) \tag{1.24}$$

where a_0 is the effective separation of the electron and hole in a CT state across the D/A HJ, η_{diss} is the CT dissociation efficiency from Eq. 1.20, k_{rec} is the free polaron recombination rate, N_{HOMO} and N_{LUMO} are the densities of states in the HOMO and LUMO at the HJ interface, and ΔE_{HL} is the energy difference between the HOMO of the donor and LUMO of the acceptor.

1.1.10 Equivalent circuits

Practical OPVs have two parasitic resistances, as shown in Fig. 1.14. A shunt resistance, R_{SH}, which is in parallel with the diode, and a series resistor, R_S. Shunt resistance is primarily caused by fabrication defects, such as pinholes, metal penetration into the organic layers, and particles on the substrate.[54] These defects allow current to bypass the HJ causing so-called leakage current. Series resistance comes from several sources including the sheet resistance (R_{sheet}) of the electrodes, resistivity of the organics (ρ_{org}), and interfacial resistances between the constituent layers

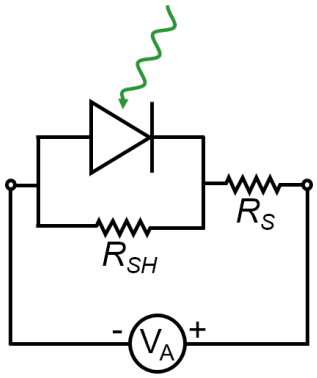

Figure 1.14: **OPV equivalent circuit diagram** | A photodiode in parallel with a shunt resistor, R_{SH}, and in series with a series resistor, R_S.

($R_{interfacial}$):[40,55]

$$R_S = R_{sheet}\left(\frac{L}{W}\right) + \frac{\sum\left(\rho_{org}t_{org} + R_{interfacial}\right)}{A} \tag{1.25}$$

where L and W are the length and width of the more resistive electrode, t_{org} is the thickness of the organic layers, A is the area of the device, and the sum encompasses all organic layers and interfaces. Typical shunt resistances are on the order of kΩ to GΩ, while series resistances are usually less than 100 Ω. The impact of these resistances on device performance can be intuited by comparing their magnitude to the dynamic resistance of the diode as a function of voltage:

$$R_{diode}(V_A) = \left.\frac{\partial V}{\partial I}\right|_{V_A}, \tag{1.26}$$

which is equal to the inverse slope of the J–V characteristic in Eq. 1.23. When V_A is small or negative, R_{diode} is at its largest and may therefore be similar to or greater than R_{SH}. In that case, a significant portion of the total current will flow through the shunt resistor. However, in this regime, the effective resistance of R_{diode} and R_{SH} in parallel is significantly larger than R_S, thus almost none of the voltage will be dropped across R_S and it can be neglected. As the diode begins to exponentially turn on in forward bias, R_{diode} decreases rapidly, thus the portion of current drawn through R_{SH} will drop until it is also negligible. At sufficient forward bias, R_{diode} will become comparable to and, eventually, less than R_S. In this regime, a significant portion of the applied voltage will be dropped across R_S, reducing the potential across the diode itself by JR_SA. For realistic devices, Eq. 1.23 must therefore be modified to contain the effect of these resistances:

$$J = J_{S,0}\left[\exp\left(\frac{q(V_A - JR_SA)}{mk_BT}\right) - \frac{k_{CT,diss}}{k_{CT,diss,eq}}\right] + \frac{(V_A/A) - JR_S}{R_{SH}} - q\int \eta_{EQE}(\lambda)\Phi(\lambda)d\lambda. \tag{1.27}$$

Simulated J–V characteristics for an OPV in the dark ($\Phi = 0$) with an ideality factor of $m = 1.6$ are shown in Fig. 1.15 as a function of R_S and R_{SH}.

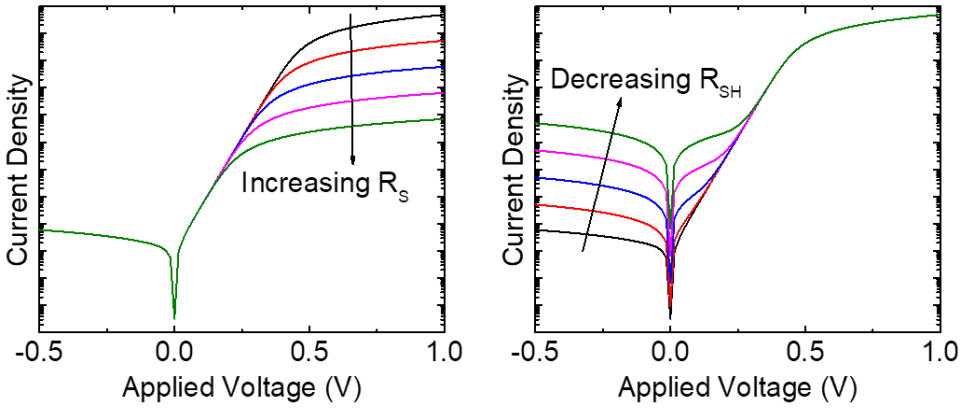

Figure 1.15: **Impact of parasitic resistances on OPV J–V characteristics** | Simulated OPV J–V characteristics with increasing R_S (left) and decreasing R_{SH} (right).

Under illumination, an OPV will generate a photocurrent equal to $q \int \eta_{EQE}(\lambda)\Phi(\lambda)d\lambda$ as outlined in §1.1.7. The left panel of Fig. 1.16 shows the measured J–V characteristics of a tandem OPV in the dark, and under several different light intensities, Φ. Subtracting the dark current from each of the total currents ($J_{total} - J_{dark}$) is approximately equal to the photocurrent, which is plotted in the right panel. In reverse bias, the magnitude of the photocurrent increases slightly since the resultant field is additive with the internal field, thus increasing η_{ext} and η_{EQE}. In forward bias, the applied field is opposite the internal field, thus the magnitude of the photocurrent decreases. Above a certain voltage (≈1.7 V for the OPV in Fig. 1.16), the field resulting from the applied voltage surpasses the internal field, causing the photogenerated charges to flow in the opposite polarity.

1.1.11 Photovoltaic efficiency

In general terms, a circuit element that supplies power must generate a current that opposes its terminal voltage. An OPV operating in quadrant IV of its J–V characteristic on a linear-linear plot is, therefore, generating power equal to the product of

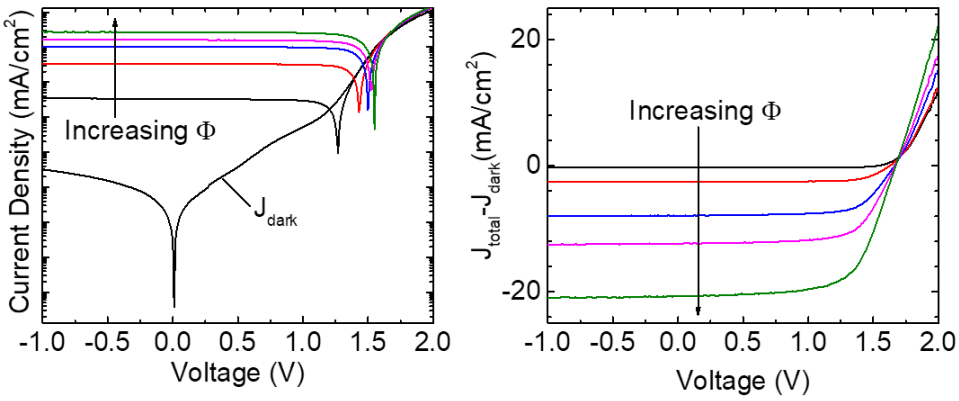

Figure 1.16: **Light intensity and voltage-dependent photocurrent** | Left: absolute value of current vs. voltage for a tandem (*i.e.*, 2-junction) OPV in the dark, and under several different light intensities, Φ. Right: photocurrent vs. voltage for the same OPV, approximated by subtracting the dark current J_{dark} from the total current J_{total} at each intensity. Note: This method of calculating photocurrent ($J_{total} - J_{dark}$) is highly approximate, since the presence of the photogenerated charges perturbs the behavior of the thermally generated and electrically injected charges that constitute J_{dark}.

its current and voltage, as shown in the right panel of Fig. 1.17. The maximum power density the OPV can output, P_{max}, is found at its maximum power point (MPP), where $V = V_p$ and $J = J_p$. The quotient obtained by dividing P_{max} by the optical power incident on the device, P_{in}, is its PCE.

More commonly, PCE is expressed in terms of J_{SC} (the current density at $V = 0$), V_{OC} (the voltage at $J = 0$), and fill factor (FF),defined as:

$$FF = \frac{J_p V_p}{J_{SC} V_{OC}}, \tag{1.28}$$

which is equal to the ratio of the red-shaded area to the gray-shaded area in Fig. 1.17. Using these quantities, $P_{max} = J_{SC} V_{OC} FF$, and PCE is therefore:

$$PCE = \frac{J_{SC} V_{OC} FF}{P_{in}}. \tag{1.29}$$

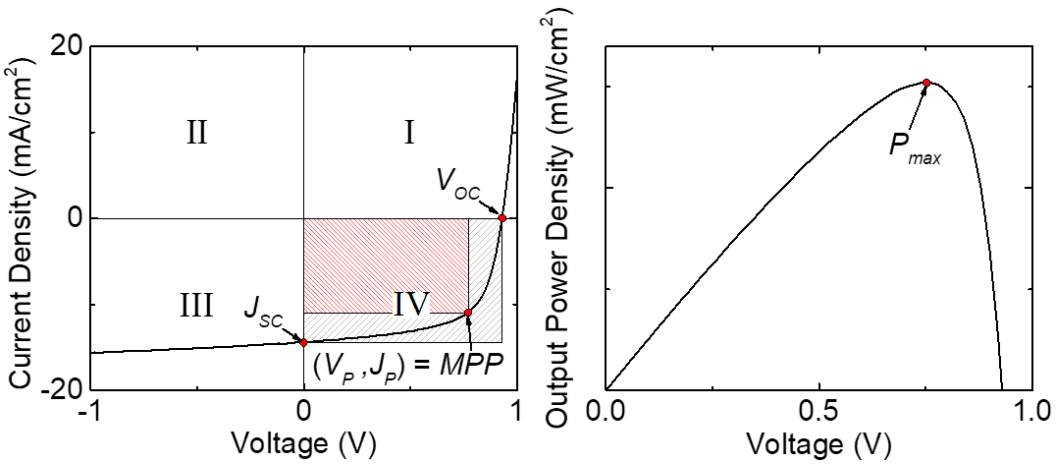

Figure 1.17: **Output power of an illuminated OPV** | Left: J–V characteristics of an OPV under illumination with key operating points shown: J_{SC}, V_{OC}, and MPP. Right: output power density vs. voltage for the same OPV with the maximum output power, P_{max}.

1.1.12 Standard solar spectra

In theory, the *PCE* of a solar cell can be measured in response to an arbitrary illuminant by measuring P_{in} from the source, measuring the J–V characteristics of the OPV while illuminated, extracting J_{SC}, V_{OC}, and FF, and performing the calculation in Eq. 1.29. This method can be used to determine the efficacy of a cell for a specific application—indeed, what matters practically is how much power a particular cell generates and whether or not that power is sufficient for its intended use. However, enabling reliable comparison between various photovoltaic technologies and results from different laboratories requires a more rigorous standardized treatment. An important component of photovoltaic testing is standardization of the solar spectrum. Outside of the earth's atmosphere, spectral irradiance from the sun is quite constant, varying only slightly ($< 1.7\%$)[56] from day-to-day due to the presence of faculae, sunspots, and solar flares. Over the years, satellites mounted with spectral radiometers, space shuttles, high altitude spacecraft, and solar telescopes have accurately measured bands of this broad spectrum, allowing standards organizations to generate standardized composite spectra. These extraterrestrial spectra, are typically referred

to as air mass 0 or "AM0" spectra, and have an irradiance of 1366.1 W/m^2. The most widely used AM0 spectra are the "Standard Extraterrestrial Spectrum Reference E-490-00", which was compiled by the American Society for Testing and Materials (ASTM) in 2000, and the "Gueymard synthetic extraterrestrial spectrum" [56].

Standardizing the terrestrial solar spectrum creates a new set of challenges, as the spectral irradiance of the sun varies significantly as a function of latitude, time of year, time of day, altitude, local weather conditions, particulate densities, and the levels of absorptive gasses (H_2O, CO_2, CH_4, O_3, NO_2, chlorofluorocarbons, etc.) in the atmosphere. The universally adopted standard, ASTM G-173,[57] is calculated from AM0, by applying geometric and atmospheric corrections that reasonably approximate conditions in the contiguous United States, as follows:

- The receiving panel has a 37° south-facing tilt from the earth's surface normal vector, and sits at sea-level.
- The sun's rays arrive at the panel perpendicular to its surface. Since the atmosphere refracts the sun's rays, this corresponds to a solar angle of 48.19° from the earth's surface normal vector.
- The solar illumination passes through an absolute air mass of 1.5, where air mass is defined as $AM = L/L_{normal}$. Here, L is the path length through the atmosphere, and L_{normal} is the thickness of the atmosphere normal to earth's surface.
- The content of the atmosphere is defined using the 1976 U.S. standard atmosphere.[58]
- The spectrum is "global", *i.e.*, diffuse light from the sky and reflected light from the ground are included. The ground reflection is non-lambertian, with a spectrally-varying albedo as measured by the NASA Jet Propulsion Laboratory for "light sandy soil." [57]

This spectrum is often abbreviated as "AM1.5G", since it corresponds to an air mass of 1.5 and includes diffuse and ground-reflected light. The total irradiance of AM1.5G is 1000 W/m^2 or 100 mW/cm^2. The referenced AM0 and AM1.5G spectra are plotted vs. wavelength and photon energy in Fig. 1.18. A properly calibrated OPV efficiency measurement is one that replicates what the cell's performance *would be* under AM1.5G illumination.

The actual solar flux incident on different regions of the United States has been constantly measured for decades on panels at various angles, and concentrating solar collectors.[59] For the sunniest parts of the country, such as Phoenix, AZ, the average daily solar flux is 6.5 kWhr/m^2/day (equivalent to 6.5 hr of AM1.5G per day). For Detroit, MI, the solar flux is significant lower on average—4.23 kWhr/m^2/day, equivalent to 4.23 hr of AM1.5G per day.

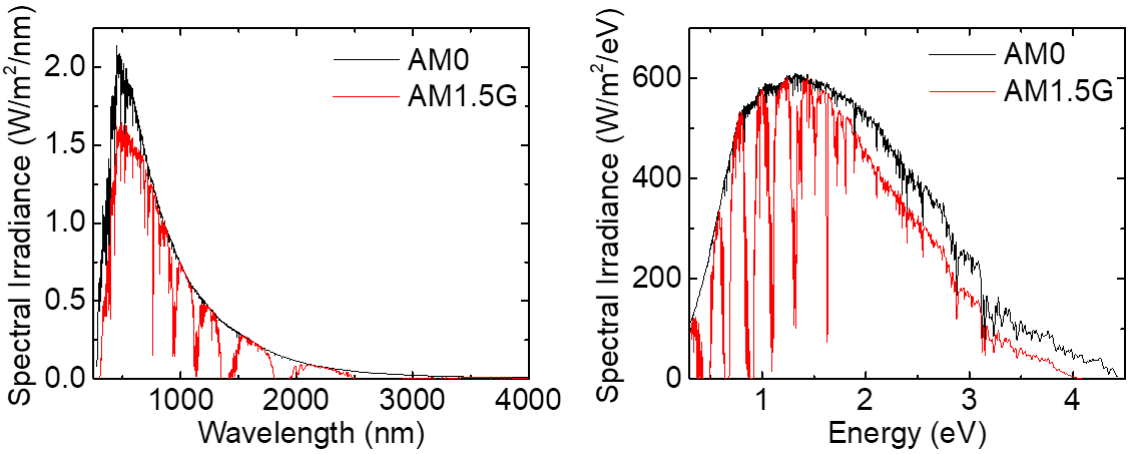

Figure 1.18: **AM0 and AM1.5G solar spectra** | Spectral irradiance of the standard AM0 and AM1.5G solar spectra as a function of wavelength (left) and photon energy (right).

1.1.13 Calibrated photovoltaic efficiency measurements

The lack of a true AM1.5G light source presents a number of challenges for the calibrated measurement of photovoltaic cells, as even reasonably-well matched laboratory solar simulators and outdoor measurements will inevitably produce variations

that decrease the accuracy of cell-to-cell and interlaboratory comparisons. Photocurrent is particularly susceptible to miscalibration, since it is linearly proportional to solar intensity and device area. It is therefore critical to measure the wavelength dependent EQE of the cell, which can then be integrated over the reference AM1.5G spectrum to produce an exact value of what J_{PH} would be under perfect AM1.5G illumination ($J_{PH,AM1.5G}$). A schematic of an EQE experimental measurement setup is shown in Fig. 1.19.

First, a light source is monochromated and chopped with a certain frequency. This light can be either focused directly onto the device, or focused into an optical fiber as shown in Fig. 1.19. A lock-in current amplifier is then used to synchronously detect the current generated by the solar cell in response to the light at each wavelength. Current can be converted to units of charges/second by dividing by the charge of an electron, q. The light intensity at each wavelength is then calibrated using a certified photodiode with a known responsivity (units of A/W). Measuring the wavelength

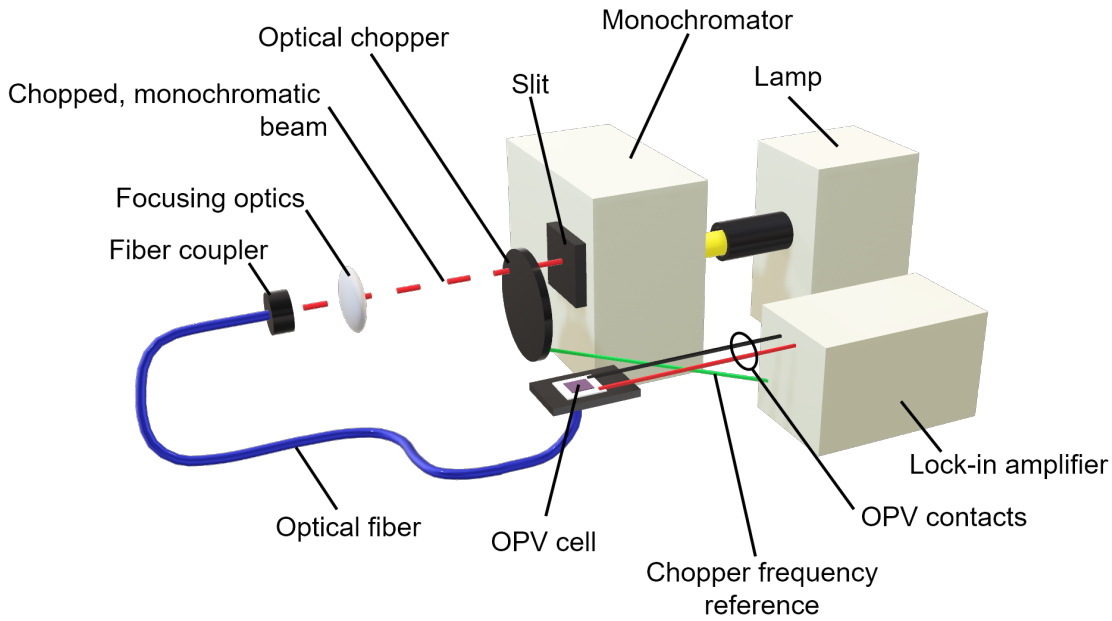

Figure 1.19: ***EQE* measurement setup schematic** | Basic optical setup and electrical detection circuitry required to measure EQE of an OPV cell.

dependent photocurrent on the reference diode in the same method as above, and then dividing by its responsivity, produces the optical power at each wavelength. Power can be converted to photons/second, by dividing by the photon energy at each wavelength ($E = hc/\lambda$, where h is Planck's constant). In total, EQE is defined as:

$$EQE(\lambda) = R_{ref}(\lambda)\frac{I_{OPV}(\lambda)}{I_{ref}(\lambda)}\frac{hc}{q\lambda}, \tag{1.30}$$

where $R_{ref}(\lambda)$ is the responsivity of the reference cell and $I_{OPV}(\lambda)$ and $I_{ref}(\lambda)$ are the measured photocurrents of the OPV and reference cell as a function of λ. The theoretical J_{PH} under AM1.5G illumination can be calculated using the equation:

$$J_{PH,AM1.5G} = \frac{q}{hc}\int EQE(\lambda)SI_{AM1.5G}(\lambda)\lambda d\lambda, \tag{1.31}$$

where $SI_{AM1.5G}(\lambda)$ is the spectral irradiance of AM1.5G. In some cases, EQE will depend on light intensity, thus the OPV may need to be biased with a constant white light during the EQE measurement. When measured correctly, $J_{PH,AM1.5G}$ is equivalent to J_{SC}.

To measure the remainder of the J–V characteristics, an illumination source should be chosen that closely matches the AM1.5G spectrum over the absorption region of the OPV. Most labs employ a Xe arc lamp with an AM1.5G filter that provides a reasonably good match for visible wavelengths. Solar simulators are rated based on their spatial nonuniformity, temporal instability, and spectral match from class A to class C for each metric. The highest rating, class AAA has spatial nonuniformity and temporal instability $< \pm 2\%$, and its entire spectrum is within 25% of AM1.5G.[60] During these measurements, it is also critical to know the precise area of the device, and ensure that no photocurrent contribution is coming from outside this area. A typical OPV substrate and masking scheme is shown in Fig. 1.20, where the device area is defined as the intersection of the ITO anode and metal cathode.

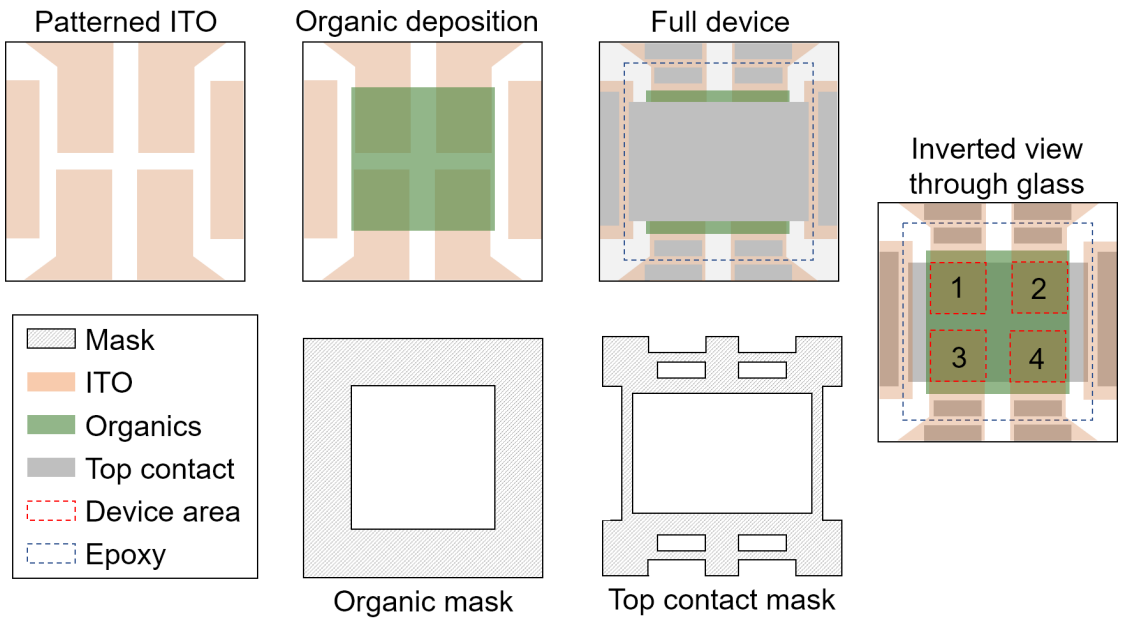

Figure 1.20: **Typical OPV device layout and masking scheme.**

A precisely-aligned mask can be used between the device and light source during measurement to ensure that only the device active area is being illuminated.

Calibrating the intensity of the solar simulator is typically performed with a calibrated Si photodiode with a known "1-sun" current. Ideally the reference cell is filtered, such that it absorbs in the same range as the cell to be tested. The J–V characteristics of the OPV under this "1-sun" intensity will be similar to what they would be under AM1.5G. However, since the spectrum of the simulator is inevitably mismatched from AM1.5G, this measurement may produce errors—most clearly detected by a mismatch between $J_{PH,AM1.5G}$ (from the integrated EQE) and the J_{SC} extracted from the J–V characteristics. This is because certain spectral bands from the simulator will be more intense (and others less) than AM1.5G. These regions compensate each other to produce the 1-sun current on the Si photodiode. When testing the OPV, it is unlikely that such perfect compensation will occur.

The magnitude of this mismatch is quantified using the spectral mismatch factor,

M:[61–63]

$$M = \frac{\int_{\lambda1}^{\lambda2} SI_{AM1.5G}(\lambda)R_{ref}(\lambda)d\lambda}{\int_{\lambda1}^{\lambda2} SI_{AM1.5G}(\lambda)R_{OPV}(\lambda)d\lambda} \frac{\int_{\lambda1}^{\lambda2} SI_{sim}(\lambda)R_{OPV}(\lambda)d\lambda}{\int_{\lambda1}^{\lambda2} SI_{sim}(\lambda)R_{ref}(\lambda)d\lambda}. \tag{1.32}$$

Here, $SI_{AM1.5G}$ and SI_{sim} are the spectral irradiance of AM1.5G and the solar simulator, and R_{OPV} and R_{ref} are the responsivity of the OPV and the reference cell. The integration range, $\lambda1$ to $\lambda2$ should extend beyond the absorption of the reference cell and OPV, to ensure that all of the photocurrent is included. If the solar simulator intensity is set to produce a current in the reference cell equal to its calibrated 1-sun current, J_{SC} of the OPV can then be "corrected" for mismatch by dividing by M.[61]

While calibrating simulator intensities with a reference cell and correcting *via* mismatch factor is common practice in the OPV community, this can lead to errors. First, consider that Eq. 1.32 is simply a ratio of four currents:

- the top left term is the calibrated 1-sun current of the reference cell;
- the bottom left term is $J_{PH,AM1.5G}$ of the OPV calculated from its EQE;
- the top right term is the J_{SC} of the OPV under the simulator; and,
- the bottom right term is the J_{SC} of the reference cell under the simulator.

When the simulator's intensity is calibrated with the reference cell (*i.e.*, its current on the simulator is equal to its 1-sun calibrated value), the top left and bottom right terms in Eq. 1.32 cancel each other by definition. In this case, correcting for mismatch by dividing J_{SC} of the OPV by M, simply returns $J_{PH,AM1.5G}$ from the EQE. In addition to J_{SC}, which is known to be inaccurate when $M \neq 1$ (hence the mismatch factor correction), FF, and V_{OC} may also be inaccurate, since they depend weakly on intensity. Solving Eq. 1.23 for V_{OC} at $J = 0$:

$$V_{OC} = \frac{mk_BT}{q} ln\left(\frac{q\int \eta_{EQE}(\lambda)\Phi(\lambda)d\lambda}{J_{S,0}} + \frac{k_{CT,diss}}{k_{CT,diss,eq}}\right). \tag{1.33}$$

Instead, OPVs can be measured using a simulator intensity that produces $J_{SC} = J_{PH,AM1.5G}$. Under this condition, no spectral correction is required, and the photocurrent, $q\int \eta_{EQE}(\lambda)\Phi(\lambda)d\lambda$, is identical to that under AM1.5G. As a result, FF and V_{OC} will also be accurate with the following caveats.

- Using this scheme, the calibration of the EQE measurement setup is critical, and should be checked frequently by measuring the EQE of a calibrated Si photodiode and integrating over the AM1.5G spectrum to ensure that its $J_{PH,AM1.5G}$ closely matches its calibrated 1-sun current.

- The spatial distribution of charges generated in an OPV is different for each wavelength. While J_{SC} will be forced to match $J_{PH,AM1.5G}$ using this method, the equilibrium charge density under the simulator may differ from that under AM1.5G. Theoretically, this could perturb FF and V_{OC}. However, using the common method of Si photodiode intensity calibration does not address this problem either, since the distribution *and* density of charge will still be different than under AM1.5G.

- The proposed scheme is only intended for brief efficiency measurements. Degradation and cell heating may be highly wavelength dependent in OPVs. Thus, for example, a simulator capable of producing $J_{SC} = J_{PH,AM1.5G}$ on the OPV, but that does not contain the near-UV photons present in AM1.5G, may therefore be inadequate for simulated long-term aging experiments.

1.1.14 Device fabrication methods

All materials in this work, including organics, metal oxides, and metals were purchased commercially. The organic compounds were purified using vacuum thermal gradient sublimation,[64] while the other materials were used as-purchased. A variety of unpatterned substrates were used in this work: glass, quartz, Si, sapphire,

CaF_2, and KBr. The salt substrates were used for Fourier transform infrared (FTIR) spectroscopy, and were not cleaned prior to thin film growth. All other substrates were sonicated sequentially for five minutes each in a tergitol/deionized (DI) H_2O solution, DI H_2O, acetone (2×), and isopropyl alcohol (2×). Glass substrates with pre-patterned ITO anodes were used for all photoactive organic devices and cleaned using the same procedure. After sonication, the substrates were removed from the isopropyl alcohol and rapidly dried with a stream of N_2. Pre-patterned ITO substrates intended for OPV fabrication were then "snow cleaned" on a 100°C hot plate with a stream of CO_2 for 30 s to remove any remaining particles,[65] and treated with ultraviolet (UV)-ozone for 10 min to lower the work function of the ITO.[66]

All layers in this work were deposited using vacuum thermal evaporation (VTE) under high vacuum ($< 2 \times 10^{-7}$ Torr). Deposition rates and film thicknesses were monitored using a quartz crystal microbalance (QCM), and calibrated by measuring film thickness *via* variable angle spectroscopic ellipsometry or profilometry (in the case of metals). The layers were deposited through shadow masks to confine constituents to desired regions of the substrate, and device active areas were defined as the overlap area of the ITO anode and metal cathode as shown in Fig. 1.20. Device areas between 0.09 cm^2 and 1 cm^2 depended on the requirements of the experiment. Devices were stored and transported exclusively in vacuum or N_2 to avoid exposure to atmospheric contamination unless otherwise noted.

Many thin films and devices in this work were encapsulated to perform experiments in air or for OPV aging. These were encapsulated in a high purity N_2 glovebox (< 1 ppm H_2O and O_2) by affixing a glass slide to the substrate by applying a UV-curable bead of epoxy around its periphery as shown in Fig. 1.20. In many cases, a BaO_x/SrO_x desiccant sticker was placed on the inside of the cover glass to scavenge any residual H_2O or O_2 and to absorb any H_2O or O_2 that leak into the package during aging. A desiccant was not included in the package of devices aged at high intensity,

since the stability of the desiccant to elevated temperatures and light intensities was not known.

1.2 Organization of the thesis

Since the introduction of C_{60} to OPVs in 2001,[18] fullerenes have been the most widely used and studied acceptor materials. This thesis will explore several aspects of photovoltaic devices based on the fullerenes C_{60} and C_{70}. Chapter II shows how organic heterostructures can be used to confine electrons to a thin C_{60} or C_{70} channel where they can diffuse laterally over several cm. The implications of this effect will be demonstrated in OPVs with sparse cathode grids. Future work, and additional applications that may benefit from this effect will also be proposed. The remainder of this thesis will focus on the operational stability of OPVs, beginning in Chapter III that will introduce the metrics, experimental methods, and accelerated aging techniques used to characterize OPV reliability. Chapter IV examines the photochemical stability of a number of organic thin films used in OPVs, and shows quantitatively how photo-oligomerization of C_{60} leads to burn-in of planar HJ OPVs. Chapter V focuses on the morphological stability of fullerene-based EF-CBLs, and demonstrates the importance of morphological stability to OPV reliability *via* thermally-accelerated aging experiments. In Chapter VI, the temperature and intensity-dependent performance of small-molecule OPVs are evaluated with respect to their diurnal operation. In Chapter VII, extremely stable OPVs based on DBP:C_{70} with TPBi:C_{70} EF-CBLs are aged at high illumination intensities in order to accelerate their degradation and elucidate their very slow degradation modes. Lastly, Chapter VIII describes how highly stable OPVs might be practically realized, and outlines future work for OPV reliability.

CHAPTER II

Long-range electron diffusion in organic heterostructures with fullerene channels

As discussed in Chapter I, the area of an OPV that produces photocurrent can typically be accurately defined by the intersection area of the anode and cathode contacts. An exception to this rule is the small amount of light ($\sim 1\%$) that may scatter in from the periphery of this area, thus an aligned shadow mask is typically placed in front of an OPV during calibrated measurements to ensure that light is only incident on the intended photoactive area. However, certain devices deviate from this trend, producing a significantly greater photocurrent when illuminated without a mask than they do with a mask.[67] The OPVs in question employ a PMHJ structure with donor–acceptor–acceptor' (d–a–a') type donor molecule[68,69] such as DTDCPB or DTDCTB in the blended HJ with C_{70}, and have a neat layer of fullerene on top. The photocurrent contribution from outside the overlap area of the electrodes was particularly pronounced in small area devices. For example, a 4 mm diameter single junction device with the structure: 150 nm ITO / 10 nm MoO_3 / 80 nm DTDCTB:C_{70} / 10 nm C_{60} / 8 nm BPhen / 100 nm Ag, produced a J_{SC} of 11.3 mA/cm^2 when illuminated without a mask. A 1 mm diameter circle with the same structure produced an apparent photocurrent of 12.3 mA/cm^2, a 9% increase. Devices in this section are named following the convention: (donor in the HJ)-(thickness and

type of neat fullerene)-(type of buffer layer: neat = 8 nm BPhen, EF-CBL = 10 nm BPhen:C_{60} 1:1 EF-CBL).

2.1 Steady-state line scans

To understand the origin of this anomalous photocurrent contribution and, indeed, to ensure that its origins were from beyond the overlap area of the electrodes, OPVs were illuminated continuously from an optical fiber as shown in Fig. 2.1a. The fiber was then rastered across the surface of the glass and the photocurrent at each position was recorded, as shown in Fig. 2.1b. For a typical OPV without a neat fullerene layer or d–a–a' donor, the photocurrent contribution quickly vanished beyond the edge of the cathode, with a 0.2-0.3 mm tail corresponding to the width of the fiber and scattered light. However, devices that included a neat fullerene layer and d–a–a' donor blended with C_{70} in the HJ continued to produce an appreciable photocurrent for several mm outside the edge of the metal cathode, hence called "edge currents."

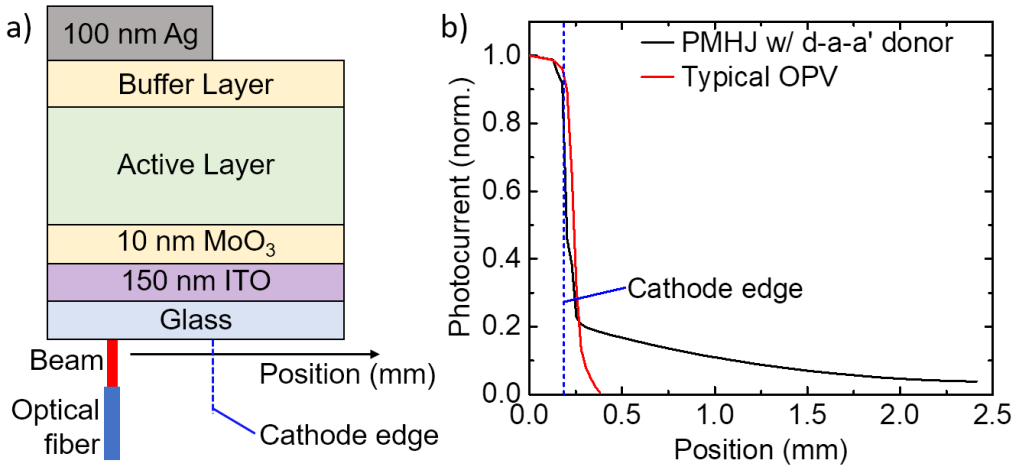

Figure 2.1: **Position dependence of photocurrent generation** | **a)** Simplified schematic of the setup employed to measure the positional dependence of photocurrent in a series of OPVs. **b)** Normalized position-dependent photocurrent scans of a DTDCPB-(10 nm C_{60})-neat OPV compared to a typical DBP:C_{70} PMHJ OPV.

2.2 Transient line scans

In a photoactive organic heterostructure, three forms of energy transfer are present: light (*e.g.*, trivial scattering or absorption and re-emission), exciton diffusion, and charge transport. These three mechanisms have different properties, which make it possible to determine which of them is primarily responsible for producing edge currents. Perhaps the clearest difference between these transfer mechanisms is their transient response. Photons are very fast on the expected timescale for polaron transfer over millimeters (> 1 ms), and the intrinsic lifetime of excitons limits their transit time to < 1 μs. The response of these energy transfer mechanisms to electric fields will also be different, given that excitons and photons have no net electric charge.

To study the transient behavior of edge currents, we constructed a transient photocurrent setup as shown in Fig. 2.2. The measurements were performed under vacuum in an open-loop liquid N_2 cryostat with four feedthroughs for the electrical probes, optical fiber, and fiber positioning arm pictured in Fig. 2.3. The electrical probes and fiber positioning arm were controlled with x-y-z positioning stages with a resolution of 50 μm. The optical fiber was bare, with a 25 μm core diameter and a numerical aperture of 0.1. A optical micrograph of the cleaved fiber tip is shown

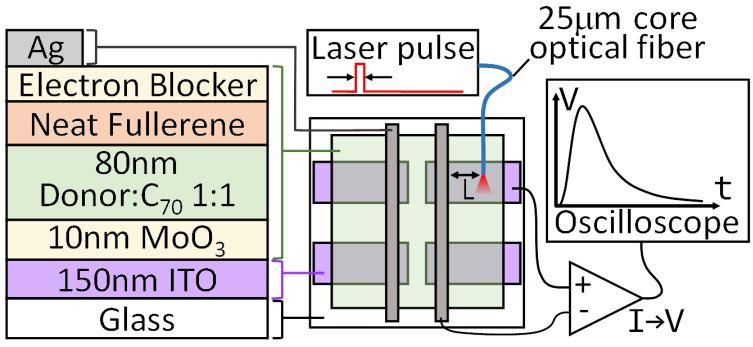

Figure 2.2: **Transient photocurrent measurement schematic** | Device structure, substrate design, and measurement schematic used for transient photocurrent measurements. The distance, L, is the distance between the position of the optical fiber and the edge of the cathode. Adapted from Q. Burlingame *et al.* (2018).[31]

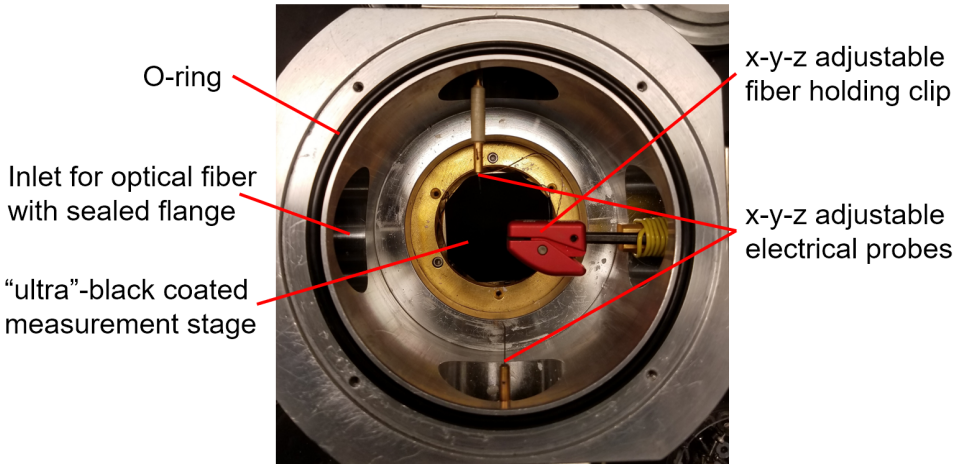

Figure 2.3: **Photograph of the transient photocurrent measurement setup** | **a)** Top view of the liquid N_2 cryostat used to measure transient photocurrent spectra with key components labeled. During operation, a lid with a quartz window was placed on top of the o-ring, and the cryostat was evacuated.

in Fig. 2.4a, along with its measured output from a Si CCD beam profiler in Fig. 2.4b. The FWHM of the beam was 47 μm. The stage of the cryostat was coated with a 99+% optically absorptive black foil to prevent light scattering, as shown in Fig. 2.3. Diode lasers with wavelengths of either 405 nm or 637 nm were coupled into the fiber, depending on the measurement. The diodes were driven by a pulse

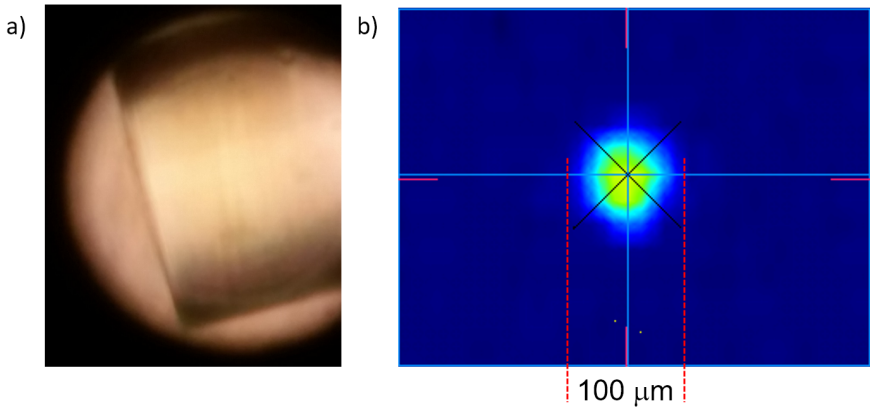

Figure 2.4: **Optical fiber characterization** | **a)** Optical micrograph of the 25 μm core optical fiber used to illuminate OPV samples during transient photocurrent measurements. **b)** Profile of the output beam from the fiber in **a** measured using a Si CCD beam profiler. The FWHM of the beam is 46 μm.

generator with pulse durations of 0.5-2 ms and a period of 1-100 s, depending on how long the photocurrent transient took to return to its baseline. The current response from the OPVs was amplified with a low-noise current amplifier at 10^8 V/A, and recorded with a digital oscilloscope. Scans were averaged over 10+ pulses to reduce the noise of the measurement, and filtered with rise time filters between 10 μs and 10 ms. The steady-state dark current was subtracted from all photocurrent transients, leaving only the light response.

2.2.1 Position and thickness dependence

Figure 2.5a shows the photocurrent transients from a DTDCPB-(10nm C_{60})-neat OPV as a function of the illumination position, L. When light from the fiber is incident directly beneath the Ag, it follows the shape of the pulse with a $\sim$ 1 ms decay. Interestingly, as the fiber moves away from the cathode, the current transient becomes significantly slower, and its magnitude at any given time is reduced substantially. This slow response to light incident outside the device area is strongly suggestive

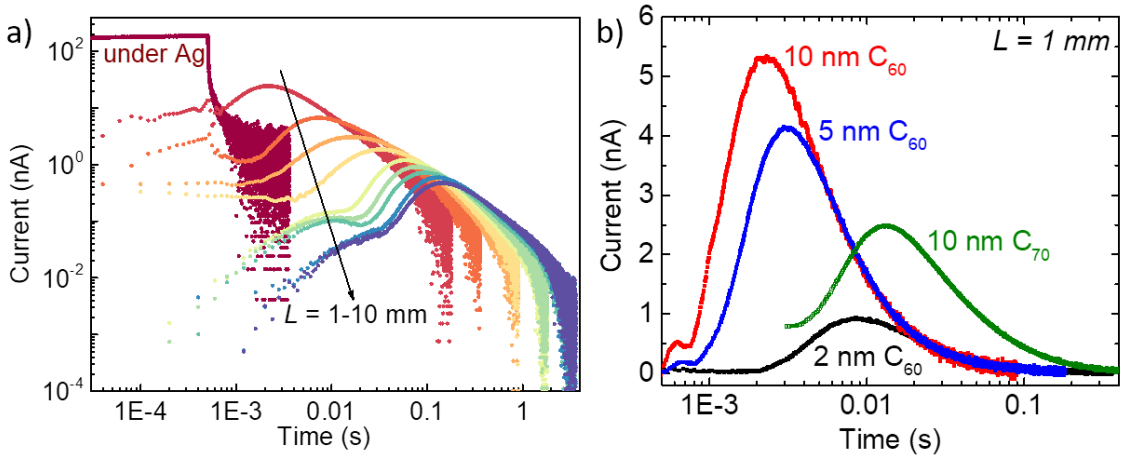

Figure 2.5: **Position-dependent transient photocurrent** | **a)** Room temperature photocurrent transients from a DTDCPB-(10nm C_{60})-neat OPV illuminated with 0.5 ms pulses of 405 nm illumination. **b)** Photocurrent transients at $L = 1$ mm for OPVs with varying thicknesses of neat C_{60} or C_{70} layer as noted in the figure.

that the anomalous photocurrent contribution is resultant of charge transport, rather than light or excitons. The magnitude and speed of the photocurrent response also depends on the thickness and type of fullerene in the neat layer, as shown in Fig. 2.5b. Thicker layers showed no significant change compared with the 10 nm C_{60} OPV, and devices with no neat fullerene layer had no response at all. This suggests that the neat fullerene layer (henceforth called the channel) is responsible for transporting the current. The proposed theory of device operation is, therefore, as follows.

- Photons incident through the ITO anode but outside the cathode are absorbed in the HJ and dissociate into free charges.
- While many of these charges recombine with one another, a portion of the holes reach the ITO, and a portion of the electrons reach the neat fullerene layer.
- These charges diffuse laterally in the neat fullerene channel until they recombine, or reach the Ag cathode and are collected.

2.2.2 Energy levels and charge confinement

A key challenge for the proposed model is understanding how the fullerene channel is able to confine charges such that they can diffuse laterally over > 1 cm, rather than penetrating back into the HJ. In theory, there is little or no energy barrier between the channel and the fullerene in the HJ since they are comprised of the same materials. To test this hypothesis, UPS was performed on DTDCPB:C_{70} HJ thin films with and without a 5 nm C_{60} channel grown on top, as shown in Fig. 2.6a. Remarkably, the *I.P.* (*i.e.*, HOMO energy) of the C_{70} in the blend undergoes a massive shift (420 ± 100 meV) compared to the neat C_{60} layer grown on top. Bilayer films of C_{60} and C_{70} had less than a 100 meV difference, as did the fullerene *I.P.* in a DBP:C_{70} blend compared to a C_{60} layer grown on top. The result of this energy level shift when blending with a d–a–a' donor molecule is an energy barrier between the HJ and channel that acts

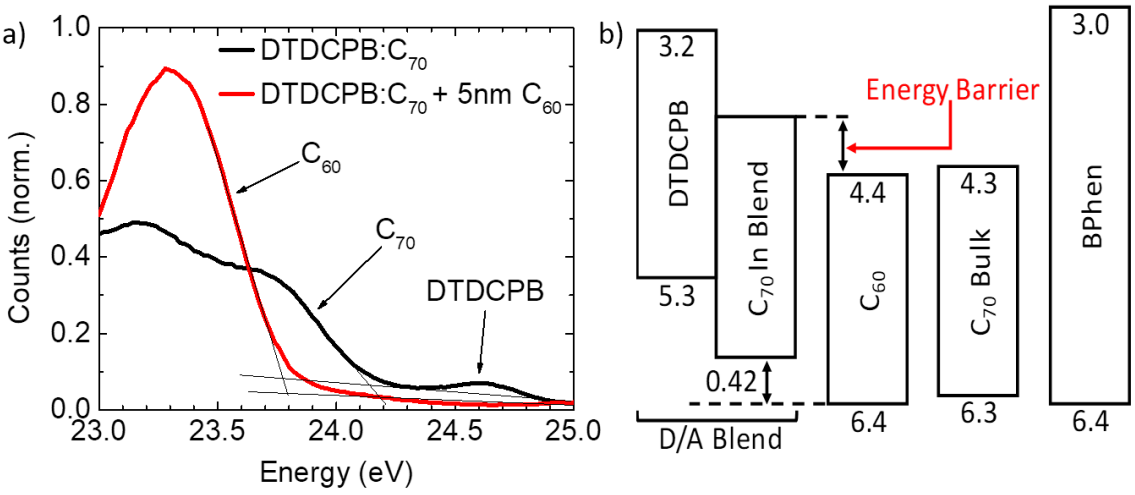

Figure 2.6: **UPS spectra and d-a-a':C_{70} energy diagram** | **a)** UPS spectra of a DTDCPB:C_{70} HJ with and without a 5 nm C_{60} channel grown on top. The *I.P.* energies are extracted from the data by taking the intercept of linear extrapolations of the peaks and baseline. **b)** Energy level diagram extracted from the UPS measurements.

to confine electrons, as illustrated by the energy level diagram in Fig. 2.6b. While the exact origin of this shift is not currently known, it is likely a polarization effect. The d–a–a' donors have large dipole moments (DTDCPB = 12.0 debye, DTDCTB = 14.5 debye),[68,69] and thus significantly shift the ground-state spatial distribution of charges in C_{70}.

2.2.3 Monte Carlo confinement simulations

The presence of the energy barrier (E_B) at the interface of the channel effectively prevents electrons from re-entering the HJ and recombining with holes or quenching at the MoO_3 interface. To quantify how large the barrier would need to be to produce lateral electron diffusion on the order we observe in DTDCPB-(10nm C_{60})-neat OPVs, we performed Monte Carlo charge hopping simulations. A simplified schematic of the simulated geometry is shown in Fig. 2.7a, though the actual dimensions of the simulation were $200 \times 7 \times 100$ in the x, y, an z dimensions and each site had a lattice constant, $a = 1$ nm (approximately the lattice constant of C_{70}). Sites with $z > 90a$

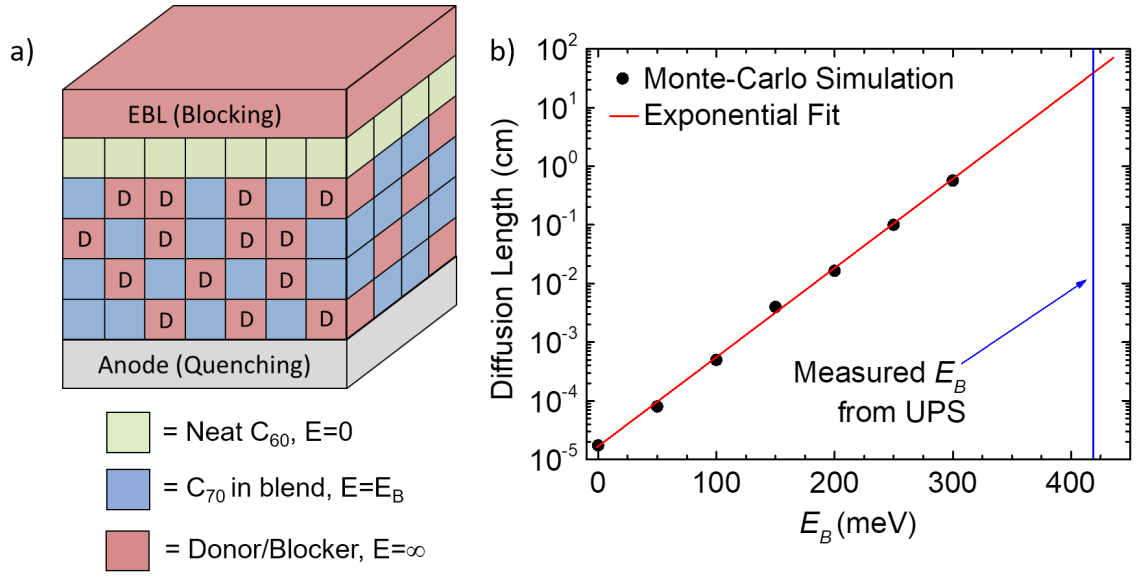

Figure 2.7: **Monte Carlo charge diffusion simulations** | **a)** Simplified schematic of the geometry used for Monte Carlo charge hopping simulations. **b)** Lateral charge hopping L_D as a function the energy barrier (E_B) between the C_{60} channel and the HJ, with the measured value of E_B from UPS shown.

(the top 10 sites in each column) were designated as channel sites representing neat C_{60} molecules. The sites in the blend were randomly generated with 50% donors and 50% fullerene molecules. The energy to hop onto a donor site was set to ∞, while the energy to hop into the blend from the channel was E_B. Periodic boundary conditions were used in y, and blocking interfaces were placed at the top of the channel ($z = 100a$) and film edge ($x = 0$). Electrons that reached $x = 200a$ were said to have been collected, and charges that reached $z = 0$ were quenched at the interface with MoO_3. Charges originated in the channel, and their motion was simulated by choosing a random direction for each hop, and apply the Miller-Abrahams hopping rate with a probability of successful hopping given by:

$$p = \exp(-E/k_B T), \tag{2.1}$$

where E is the energy difference between the current and future sites. Using this approach, the charge diffusion efficiency (η_{sim}) over $200a$ is equal to the ratio of charges collected at the cathode ($x = 200a$) to those quenched at the MoO_3 interface ($z = 0$). The charge diffusion efficiency ($\eta_D(x)$) across a distance x, is given by:

$$\eta_D(x) = (\eta_{sim})^{x/200a}, \tag{2.2}$$

and the charge diffusion length can be expressed as:

$$L_D = -200a/\ln(\eta_{sim}). \tag{2.3}$$

Calculated values of electron L_D as a function of E_B are shown in Fig. 2.7b, along with a line indicating the measured value of E_B from the UPS spectra. Even if E_B is at the lower bound of its error bar ($E_B = 320$ meV), the expected L_D would still be greater than 1 cm.

2.2.4 Charge diffusion simulations

The charge confinement simulations suggest that the measured channel barrier height is sufficient to support charge diffusion on the scale observed in the distance-dependent transient photocurrent measurements in Fig. 2.5a. To quantitatively confirm that charge diffusion caused the transient photocurrent behavior, charge dynamics were simulated from a solution to the 2-dimensional charge diffusion equation:

$$\dot{N}(x, y, t) = D\nabla^2 N(x, y, t) - kN(x, y, t) + G(x, y, t), \tag{2.4}$$

subject to blocking boundary conditions at the edges of the organic film, and a quenching boundary condition at the edge of the Ag cathode. In this case, $N(x, y, t)$, is the electron density as a function of position from the cathode, x, lateral position, y, and

time, t. The charge diffusivity is D, and k is the total rate of charge recombination and trapping. The generation term is assumed to be Gaussian in space, with the form:

$$G(x,y,t) = \frac{Q}{qt_{pulse}} \frac{q}{2\pi\sigma^2} \left[\frac{(x-x_0)^2 + (y-y_0)^2}{2\sigma^2} \right], \tag{2.5}$$

where Q is the total charge injected into the channel, t_{pulse} is the length of the pulse, σ is the width of the beam (46 μm), and (x_0,y_0) is the incident position. Here, x_0 is equivalent to L from Figs. 2.2 and 2.5. The initial electron density was set to 0, since the intrinsic carrier density in C_{60} (typically $< 10^8$ cm^{-3}, depending on purity)[70] is many orders of magnitude smaller than the photogenerated charge density. The diffusion electron current arriving at the edge of the Ag cathode, was then given by:

$$I(t) = q \int_{y_{min}}^{y_{max}} D \frac{dN(x,y,t)}{dx} \bigg|_{x \to 0} dy. \tag{2.6}$$

To fit $I(t)$ vs. t to the photocurrent transients, Eqs. 2.4-2.6 were solved numerically, and values of D, Q, and k were varied to minimize the difference between the fit and measured data with an optimization algorithm. The value of D is primarily responsible for determining the arrival time of the current transient, while k controlled the slope at long times and Q linearly controlled the amplitude. This method was applied to the position-dependent data in Fig. 2.5a, and produced fits to the data shown in Fig. 2.8. The values of D, k, and Q used to fit the position-dependent photocurrent transients of several different device structures are shown in Table 2.1. The diffusivity was similar for devices with DTDCTB and DTDCPB, and decreased for thinner fullerene channels. Employing an EF-CBL instead of the neat BPhen buffer also significantly slowed charge diffusion, presumably as charges can penetrate temporarily into the C_{60} of the EF-CBL before returning to the channel. The diffusivity of the OPV with C_{70} was lower, consistent with its lower reported electron mobility.[71,72] Nearly all of the data could be fit with $k = 0$, suggesting that trapping

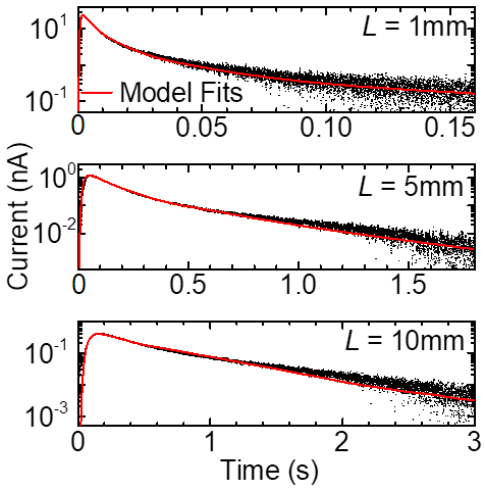

Figure 2.8: **Position-dependent charge diffusion model fits** | Fits to the photocurrent transients at $L = 1$, 5, and 10 mm, using the charge diffusion model introduced in §2.2.4. Data and fits from Q. Burlingame *et al.* (2018).[31]

and recombination were not a significant factor on the timescale of the measurements. The OPV with a C_{70} channel was an exception, as its charge loss rate was larger than even the upper bound of the OPVs with C_{60} channels.

From the fitted values of D in this work, we apply the Einstein relation (Eq. 1.14) to calculate the room temperature electron mobilities for C_{60} and C_{70} channels, al-

Table 2.1: **Charge diffusion model fit parameters** | Room temperature fit parameters (D, k, and Q) extracted from the position-dependent photocurrent transient of the devices listed.

Device	D (cm^2s^{-1})	k (s^{-1})	Q (nC)
DTDCPB-(10 nm C_{60})-neat	0.83 ± 0.07	0.9 ± 0.6	2.2 ± 0.8
DTDCTB-(10 nm C_{60})-neat	0.67 ± 0.06	1 ± 1	0.38 ± 0.02
DTDCTB-(5 nm C_{60})-neat	0.53 ± 0.03	0.4 ± 0.4	0.35 ± 0.02
DTDCTB-(2 nm C_{60})-neat	0.16 ± 0.02	0.7 ± 0.7	0.29 ± 0.03
DTDCTB-(10 nm C_{60})-EF-CBL	0.37 ± 0.08	0.3 ± 0.2	3.2 ± 0.8
DTDCTB-(10 nm C_{70})-neat	0.16 ± 0.01	2.4 ± 0.8	0.21 ± 0.02

though we note that D/μ is often higher than the Einstein relation predicts in organic semiconductors due to energetic conduction-site disorder.[28] Using this method, we find $\mu = 26 \pm 3$ for C_{60} and $\mu = 6 \pm 1$ for C_{70}, which are 2-5 times larger than the previously reported mobilities in fullerene transistors.[73,74] This is not unexpected, since the channel currents flow through the bulk with high electron densities $> 10^{17}$ cm^{-3}. Bulk mobilities in organic semiconductors are generally higher due to the presence of interfacial traps[75,76] and, as discussed in §1.1.4, the presence of energetic disorder in the film produces a charge-density dependence that increases μ at high current densities.[77]

2.2.5 Charge diffusion around physical defects

To examine the robustness of electron diffusion currents to impedance at physical defects, and to determine whether the "blocking" boundary condition at film edges is accurate, the transient photocurrent of a DTDCTB-(10 nm C_{60}-EF-CBL device was measured at $L = 3$ mm before and after a series of razor blade cuts were made to the organic layers as shown in Fig. 2.9. Compared to the pristine sample (Fig. 2.9a), cutting a 1 cm line between the illumination position and the Ag cathode edge (shown in Fig. 2.9b) significantly slowed the photocurrent transient as the current took time to diffuse around the cut. This geometry was simulated using the charge diffusion model in 2.2.4 assuming that the interface of the cut was lossless, which fits the experimental data closely as shown in Fig. 2.9d. This confirms that the edges of the film were indeed fully charge blocking, and did not introduce any additional recombination. When the scratch was completed (as shown in Fig. 2.9c) such that no continuous organic pathway persisted between the illumination position and the Ag cathode, the diffusion signal vanished except for a small signal from excess scattered light.

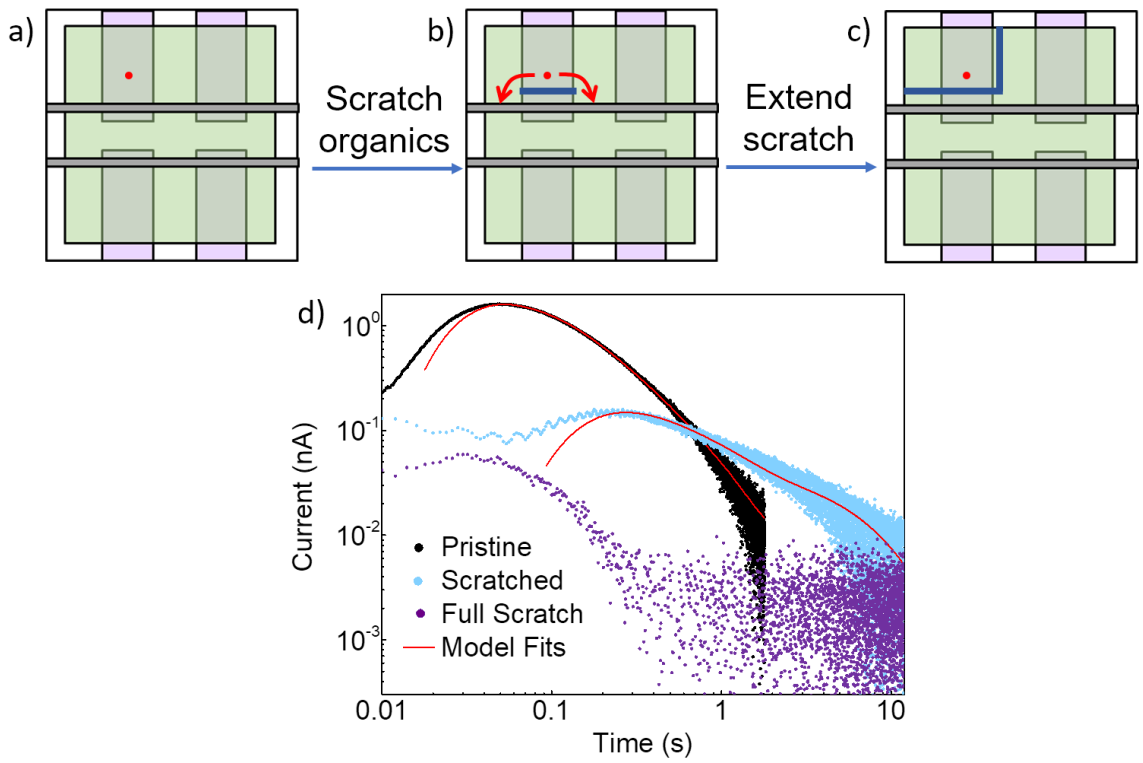

Figure 2.9: **Charge diffusion around film discontinuities** | Sample geometry diagrams for: **a)** a pristine OPV with the illumination position indicated by the red dot; **b)** an OPV after a 1 cm razor blade cut across the organic layers; and **c)** an OPV after the cut was extended such that no continuous organic path remained between the Ag cathode and the illumination position. **d)** Room-temperature transient photocurrents on a DTDCTB-(10 nm C_{60})-EF-CBL device before and after the cuts shown in **a-c** with fits to the charge diffusion model described in §2.2.4. Data and fits from Q. Burlingame *et al.* (2018).[31]

2.2.6 Temperature dependence

Temperature-dependent transient photocurrent spectra were obtained in 20°C intervals from 120K to 300K on OPVs with 10 nm C_{60} and C_{70} channels, as shown in Fig. 2.10a-b. All spectra were fit using the charge diffusion model, as shown in Fig. 2.10c-d, and the values of D and k extracted from the fits are plotted vs. the inverse thermal energy in Fig. 2.10e-f. We find that the diffusivities of both devices and k in the C_{70} device are strongly thermally activated, indicated by the red fit lines in 2.10e-f. The activation energy of D in C_{60} was 70 ± 8 meV, with activation energies of

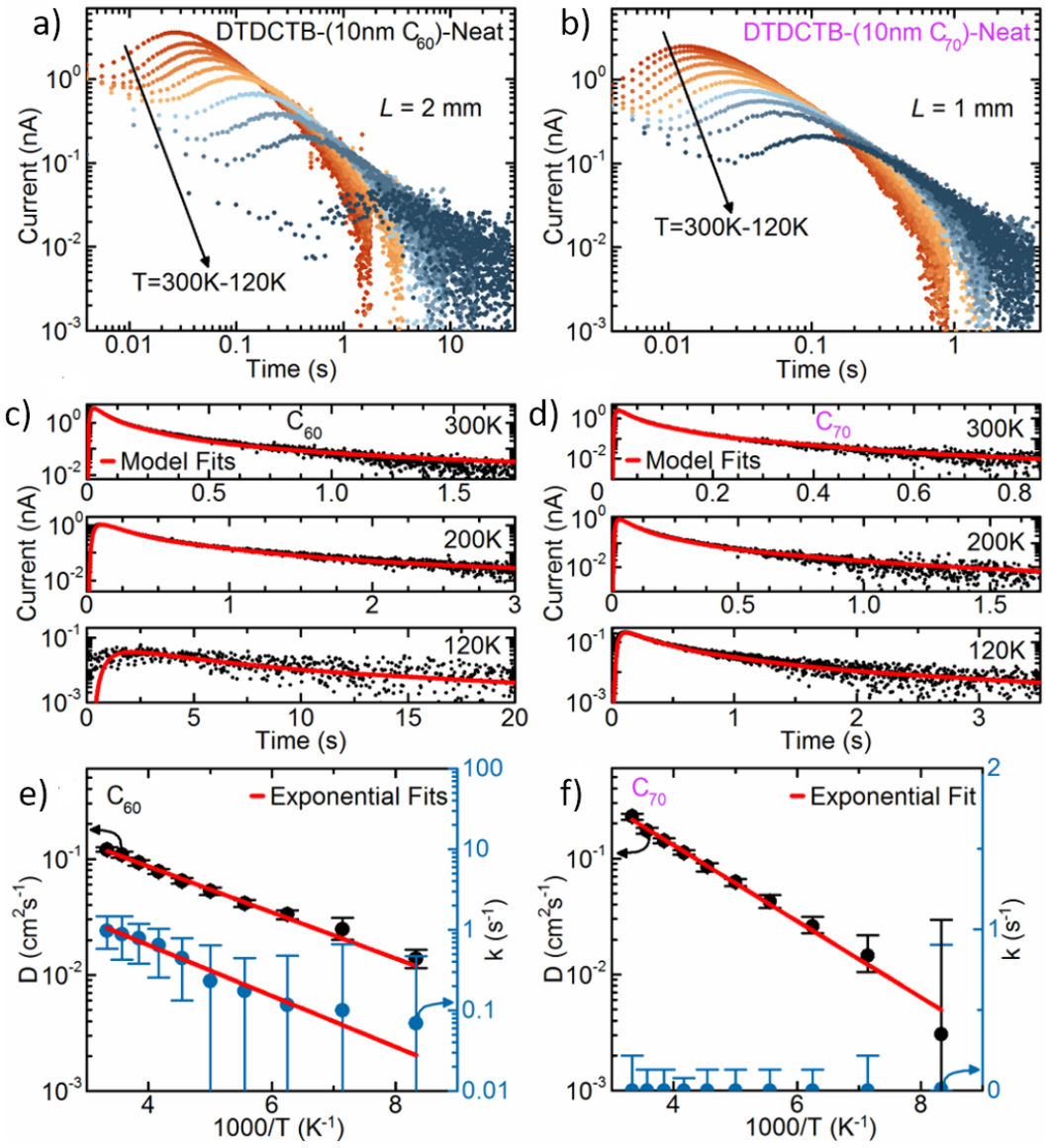

Figure 2.10: **Temperature dependence of C_{60} and C_{70} channel photocurrents** | Temperature-dependent transient photocurrent data at 20 K increments from 120 K to 300 K in response to 2 ms pulses of $\lambda = 637$ nm illumination on a **a)** DTDCTB-(10 nm C_{60})-neat OPV at $L = 2$ mm and **b)** DTDCTB-(10 nm C_{70})-neat OPV at $L = 1$ mm. **c,d)** Fits to the transient data using the model in §2.2.4 at select temperatures for the same devices shown in **a** and **b**. **e,f)** D (black points) and k (blue points) extracted from the temperature dependent fits vs. $1000/T$ for the same devices. Exponential fits are shown as red lines to D and k where applicable to extract their activation energies. Adapted from Q. Burlingame *et al.* (2018).[31]

36 ± 3 meV and 50 ± 11 meV for D and k in C_{70}. The exponential increase in D with temperature is expected as conduction in the fullerenes is limited by intermolecular charge hopping.[78] The activation energies of recombination/trapping and diffusivity are nearly the same in the device with a C_{70} channel, implying that its electron L_D is approximately the mean free path between sparsely distributed defects in the channel. To our knowledge, these are the first reported measurements of activation energy for diffusive transport in a molecular semiconductor.

2.2.7 Voltage dependence

Figure 2.11a shows the transient photocurrent spectra of a DTDCTB-(10 nm C_{60})-neat device as a function of applied voltage. Compared with 0 V, forward bias (ITO voltage > 0) reduces the current amplitude and delays the peak arrival time, while reverse bias increases the peak height and hastens the arrival of the current peak.

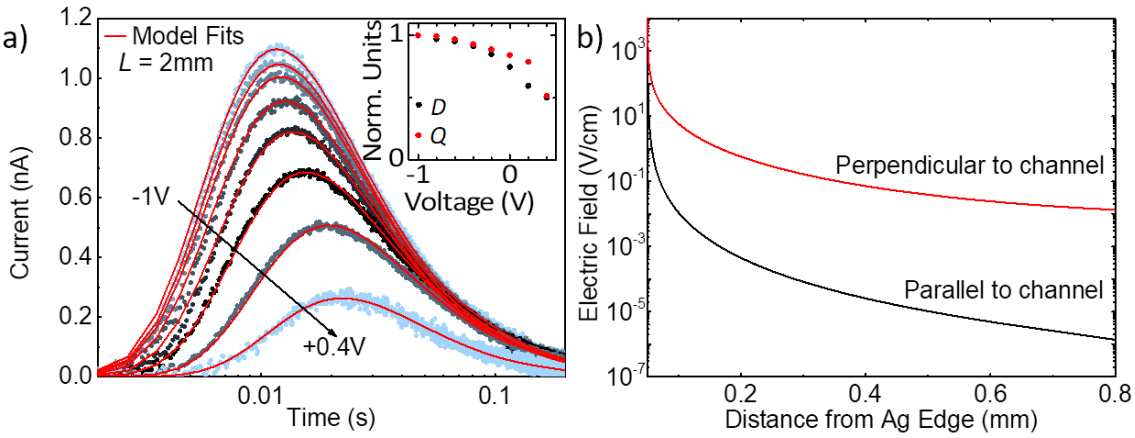

Figure 2.11: **Voltage-dependent C_{60} channel currents and field simulations** | **a)** Voltage-dependent transient photocurrent spectra at 0.2 V intervals from -1 V to 0.4 V in response to 2 ms pulses of 637 nm light on a DTDCTB-(10 nm C_{60})-neat device at $L = 2$ mm with charge diffusion simulation models fits shown as red lines. Normalized model fitting parameters, D and Q, extracted from the best fits are plotted in the inset of **a**. **b)** Finite element method electric field simulations as a function of distance from the edge of the Ag device cathode in response to 1 V applied bias.

The data were fit using charge diffusion simulations, as indicated by the red lines, and D and Q are extracted as a function of voltage and plotted in the inset. Both parameters decreased in forward bias and saturated with sufficient reverse bias. To understand these dependencies, the electric field parallel and perpendicular to the channel was simulated for 1 V of applied voltage on the OPV contacts using a finite element model, as shown in Fig. 2.11b. The geometry was approximated as two conducting planar electrodes with a 100 nm-thick insulator between them, with a relative dielectric constant $\epsilon_r = 3$. The bottom electrode and insulator extended 1 mm, representing the ITO and organic layers, while the top electrode extended just 50 μm to represent the edge of the Ag cathode. We see that the vertical field is more than four orders of magnitude larger than the horizontal field, which is too small (< 0.1 V/cm) to generate an appreciable drift current. The voltage dependence is therefore likely a result of only the field component perpendicular to the channel and the asymmetry between the channel top and bottom interfaces. In reverse bias, the applied field acts to help electrons dissociate and reach the channel (increasing Q), then preferentially pulls them toward the buffer and away from the HJ once in the channel (increasing D).

2.3 Further implications of edge currents

Thus far, this chapter has demonstrated photoactive organic heterostructures with fullerene channels that can confine electrons for several seconds, and allow them to diffuse laterally over more than 1 cm. These timescales and distances are somewhat unprecedented for charge transport in organic semiconductors, suggesting that traps and recombination centers are nearly absent in the channels and along their interfaces. The device geometry allows for unprecedented characterization of organic semiconductor charge diffusion processes, but may also enable several promising future applications for organic semiconductor devices. The remainder of this section

speculates and details preliminary findings on the feasibility of three possible applications: phototransistors, CCDs, and OPVs with sparse grid contacts.

2.3.1 Phototransistors

As this chapter has shown, the application of light to organic heterostructures with a d–a–a' donor and a fullerene channel can significantly alter the charge density in the channel. It is therefore possible to fabricate a transistor where the current between two electrodes (a drain and a source) is modulated by light incident on the organic layers. A large area phototransistor based on this concept was fabricated with the structure shown in Fig. 2.12, where the channel length was 1 cm, defined as the separation between the ITO / MoO_3 (source) and Ag (drain) electrodes. The organic structure was 80 nm DTDCPB:C_{70} / 10 nm C_{60} / 8 nm BPhen. A continuous-wave (CW) HeNe laser was incident on the organic heterostructure above the ITO and the J–V characteristics were measured as a function of calibrated output intensity from the laser. The device shows a transistor-like saturation at high applied voltages

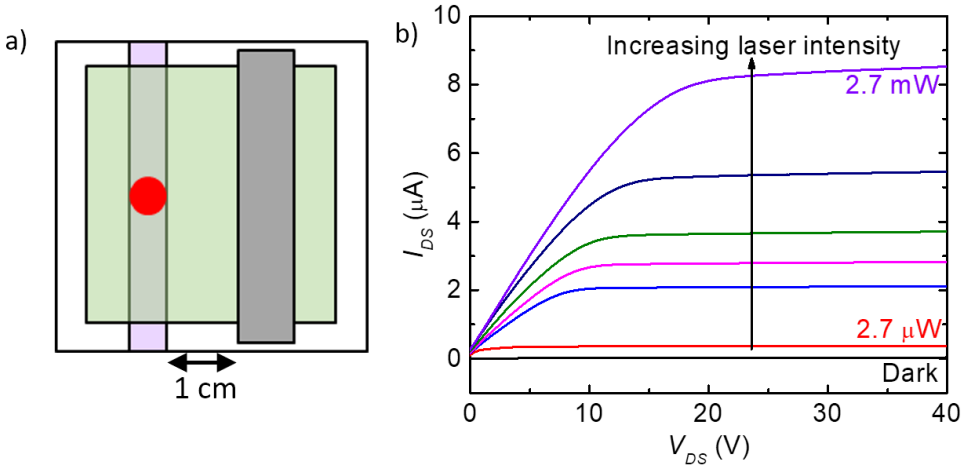

Figure 2.12: **Phototransistor schematic and performance characterization** | **a)** Schematic of an organic phototransistor employing a PMHJ with a d–a–a' donor and C_{60} channel. **b)** Performance characteristics of a phototransistor as a function of applied voltage and calibrated intensity from a CW HeNe laser.

as all the photogenerated charges are swept out. While the speed and responsivity of the devices are not high, they could serve as simple large-area detectors of room brightness or beam incidence.

2.3.2 Organic charge-coupled devices

In a CCD, many voltage-controlled pixels are connected to each other in long lines. When light is applied to a CCD, the pixels generate charges that remain stored within each pixel—isolated from neighboring pixels with potential energy barriers. To form an image, the pixels are "read" one-at-a-time, by applying a train of voltage pulses that pass each pixel's charges to its nearest neighbor. When a charge packet reaches the end of the pixel chain, a readout circuit converts it to a digital value, which is stored into memory. This bucket-brigade process continues until all of the pixels have been read and stored. Given their tendency to be trap-filled and slow, organic semiconductors have never been employed in a CCD, to our knowledge. However, given the charge lifetimes (> 1 s) we observed in the OPVs in this chapter, a fully organic CCD may indeed be possible. To realize such a device, several proofs-of-concept must be realized. First, it must be shown that an electric field incident perpendicular to the channel can be used to confine electrons to a pixel. Once this has been demonstrated than a simple $1 \times n$ CCD can be fabricated to test for packet transfer fidelity. The total time needed for readout must also be substantially faster than the decay time of the charge packets. While such organic devices would be inherently slower than conventional semiconductor CCDs, they could be made flexible and large area. This would allow them to conformally coat large optical elements, and potentially simplify complex optical systems such as telescopes.

2.3.3 Semi-transparent solar cells with grid electrodes

As described in the beginning of this chapter, the presence of edge currents can lead to OPVs efficiency measurement errors, as areas outside the intended active areas contribute current.[67] However, edge currents could also provide a useful benefit—allowing an OPV to collect photocurrent from areas where no metal cathode exists. Given proper optimization, this could lead to OPVs with a sparse metal grid contact that remain largely transparent while efficiently generating photocurrent from the non-metallized regions of the device. To test the viability of this concept, a series of 3mm × 3 mm OPVs were fabricated with varying top contact densities as shown

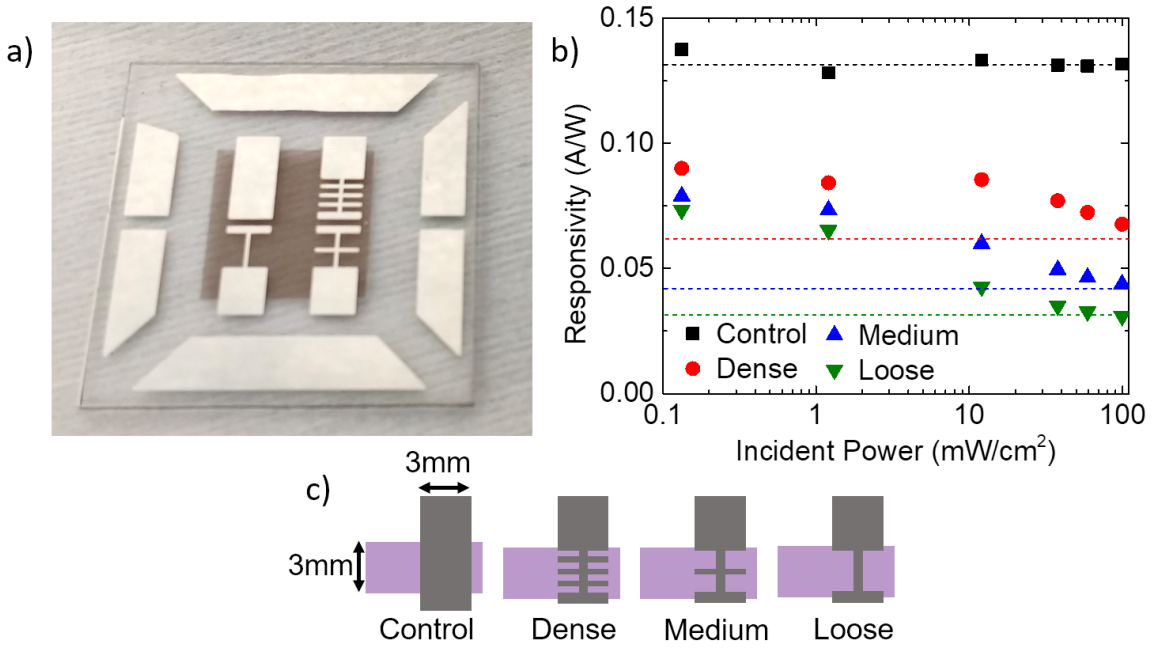

Figure 2.13: **OPVs with grid electrodes of varying densities** | **a)** Device photograph of an OPV containing four subcells: control (top left), dense grid (top right), medium grid (bottom right), and loose grid (bottom left). **b)** Responsivity vs. incident light intensity for the four OPVs shown in **a**. The dotted lines indicate the geometric expectation if only the organic area beneath the electrodes are contributing photocurrent. **c)** Schematic diagrams of the four electrode geometries showing the intersection of the 3 mm ITO strip (purple) and Al cathodes with varying shapes (gray).

in the photograph in Fig. 2.13a and schematic in Fig. 2.13b. The structure of the devices was 150 nm ITO / 10 nm MoO_3 / 120 nm DTDCPB:C_{70} 1:1 / 20 nm C_{60} / 8 nm BPhen / 100 nm Al. Figure 2.13c shows the responsivity (J_{SC}/P_{in}) as a function of P_{in} under simulated AM1.5G illumination, with dotted lines indicating the expected responsivity if only the area coated with Al was contributing. Compared to the device with full metal coverage (control), the responsivity of the grid devices rolls off strongly with intensity, such that the benefit of edge currents nearly vanishes at 100 mW/cm^2. The operational photovoltaic parameters are shown for each structure in Table 2.2, along with the operational parameters for the loose-grid device at 0.01 sun intensity. Despite losing a significant portion of its V_{OC} (0.904 $\rightarrow$ 0.72 V) and *FF* (58 $\rightarrow$ 48%), the *PCE* of the loose grid OPV is higher under 1 mW/cm^2 illumination than it is under 100 mW/cm^2, as its responsivity more than doubles.

A similar intensity roll-off was observed in the standard edge current devices.[31] Illuminating a DTDCTB-(10 nm C_{60})-neat OPV 2 mm away from the edge of its

Table 2.2: **Performance of OPVs with grid electrodes** | Photovoltaic performance characteristics of OPVs with top-grid electrodes of varying densities under 100 mW/cm^2 simulated AM1.5G illumination. Characteristics of the loose grid device is also listed under 1 mW/cm^2 to show its intensity-dependent performance roll-off.

	100 mW/cm^2 performance			
Device	J_{SC} (mA/cm^2)	V_{OC} (V)	*FF* (%)	*PCE* (%)
Control	13.2	0.911	64	7.7
Dense	6.8	0.908	58	3.6
Medium	4.4	0.907	58	2.3
Loose	3.1	0.904	58	1.6
	1 mW/cm^2 performance			
Loose	0.074	0.72	48	2.6

cathode, the *EQE* decreased from 30% to 15% as the energy of the 500 ms pulse was increased from 0.11 nJ to 1.7 nJ at a wavelength of 637 nm. Increasing the duration of the pulse from 0.1 ms to 100 ms also produced a dramatic 72% drop in *EQE* (*i.e.*, edge current charges collected per incident photon). This roll-off may simply be a function of the photogenerated charge densities that become large after long or intense pulses are absorbed. This results since the field produced by the photogenerated charges opposes further diffusion of electrons and holes to the channel and anode, respectively. For semi-transparent OPVs with reasonably efficiencies based on this technology to be realized, this problem must be addressed. However, the impact of intensity-dependent roll-off would be diminished on vertically-installed solar windows, since the solar power incident on vertical surfaces is lower than that on conventional solar cells.

The wavelength-dependent *EQE* was measured for the full-coverage control device and on the medium-grid device while illuminating under and outside the electrode, as shown in Fig. 2.14. The shape of the spectrum for the control device and medium-

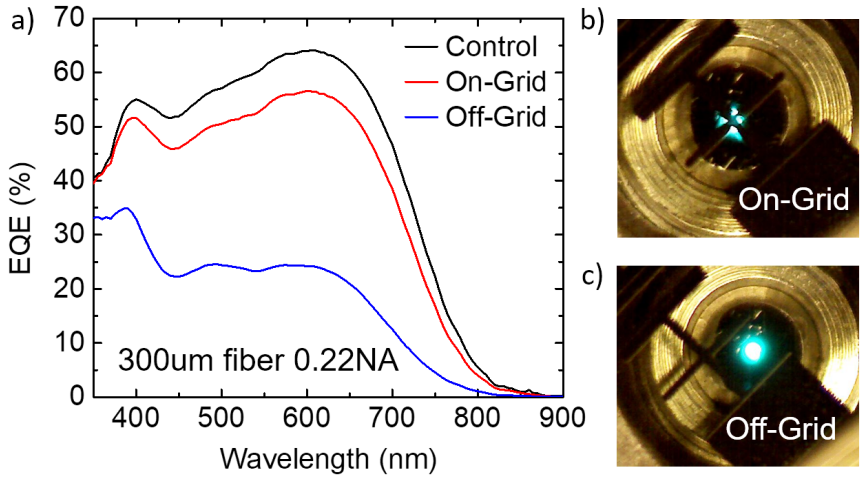

Figure 2.14: **Position-dependent *EQE* of grid electrode OPVs** | **a)** Wavelength-dependent *EQE* spectra for a control OPV with full cathode coverage, and a medium-grid OPV as defined in Fig. 2.13 illuminated beneath and outside of its grid electrode, as shown in the photographs in **b** and **c**.

grid device illuminated beneath its electrode were similar, with a small loss due to transmitted light that can be seen in the photograph (Fig. 2.14). However, when illuminating away from the metal grid, the shape of the EQE spectrum changes significantly due to the lack of secondary reflections. In addition to the intensity-dependent roll-off, the reduced EQE is responsible for the remaining efficiency difference between the control and grid-electrode devices.

CHAPTER III

Operational stability of organic photovoltaics

Over the past 15 years, innovations in materials, deposition technology, device architecture and encapsulation have increased device operational lifetimes of OPVs from minutes to years, enabled by a continually deepening understanding of the intrinsic and extrinsic degradation modes OPVs experience.[79–82] However, OPVs remain far less stable than established inorganic photovoltaic technologies such as Si and CdTe, which can operate reliably for > 25 years.[83] The development of highly stable OPV cells remains a critical challenge on the path to their widespread commercial deployment.

Among OPVs, thermally evaporated small molecular weight devices are perhaps the most promising from a reliability perspective[81,84] as they are comprised of pure materials[85,86] with controllable morphology[84,87] and high materials densities,[84] and can be readily integrated into multi-junction devices.[88,89] When encapsulated, the intrinsic lifetimes of state-of-the-art small-molecule OPVs can be greater than 50 years as this thesis will show. The gradual improvement that led to such lifetimes has resulted primarily from moving away from planar HJ devices,[81,90–93] while continued progress is required as fullerenes[94–102] are replaced with higher efficiency non-fullerene acceptors (NFAs)[48,103–107] and as multi-junction architectures are increasingly utilized.[88,89]

Degradation can be divided into two broad categories—extrinsic and intrinsic. Intrinsic degradation cannot be avoided under standard operation and, therefore, sets a theoretical maximum on device lifetime. Extrinsic degradation on the other hand can result from poor encapsulation, oxidation of electrical contacts, and stressors that may be present during a particular test but are not present in standard operation (*e.g.*, high temperatures induced by accelerated aging experiments). As of yet, OPVs with a sufficient intrinsic lifetime for commercial applications have not been demonstrated, thus understanding intrinsic degradation is currently of greater scientific interest.

3.1 Metrics of stability

Figures of merit (FoMs) that describe device reliability enable comparison between devices and laboratories. The most commonly used FoM is T_{80}, defined as the time required for the *PCE* of the OPV to degrade to 80% of its starting value, as shown in Fig. 3.1. In general though, OPVs require a combination of high *PCE* and long lifetime to be commercially viable, thus it is useful to define FoMs that place impor-

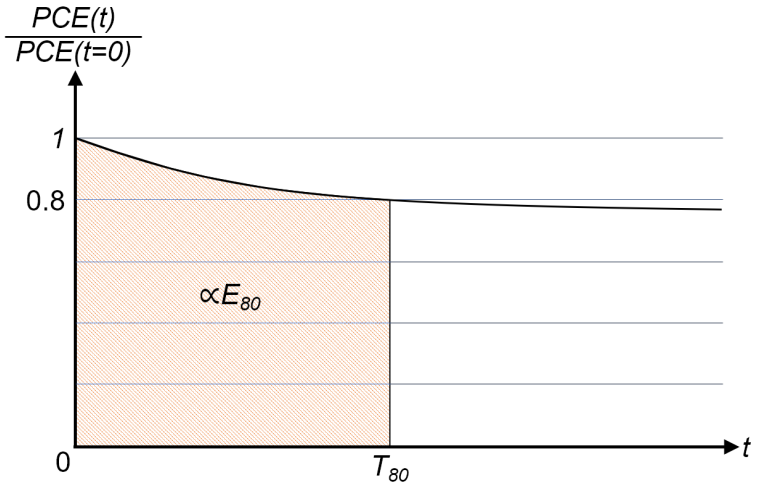

Figure 3.1: **Representative lifetime plot of an OPV** | *PCE* as a function of time normalized to its value at $t = 0$. The shaded area is approximately proportional to E_{80}.

tance on both. One such metric, called E_{80} [81] or Lifetime Energy Yield (LEY) [82], is defined as the energy a device can generate while operating at its MPP until it reaches T_{80}:

$$E_{80} = \int_{t=0}^{t=T_{80}} PCE(t)P_{in}(t)dt \tag{3.1}$$

These simple metrics can also be modified to apply to devices that experience a rapid loss of efficiency during early aging (so-called "burn-in"), before stabilizing. In this case, a stabilization time (T_S) and stabilized efficiency ($PCE(t = T_S)$) can be defined at the end of burn-in, and a stabilized lifetime ($T_{S,80}$) can be defined as the time elapsed between T_S and when the device degrades to 80% of $PCE(t = T_S)$, as shown in Fig. 3.2. [80,82,108] An E_{80} can similarly be defined for OPVs with a stabilization time:

$$E_{S,80} = \int_{t=T_S}^{t=T_S+T_{S,80}} PCE(t)P_{in}(t)dt. \tag{3.2}$$

While these energy generation metrics gives weight to both PCE and lifetime, comparisons between devices using this FoM are susceptible to being dominated by lifetime,

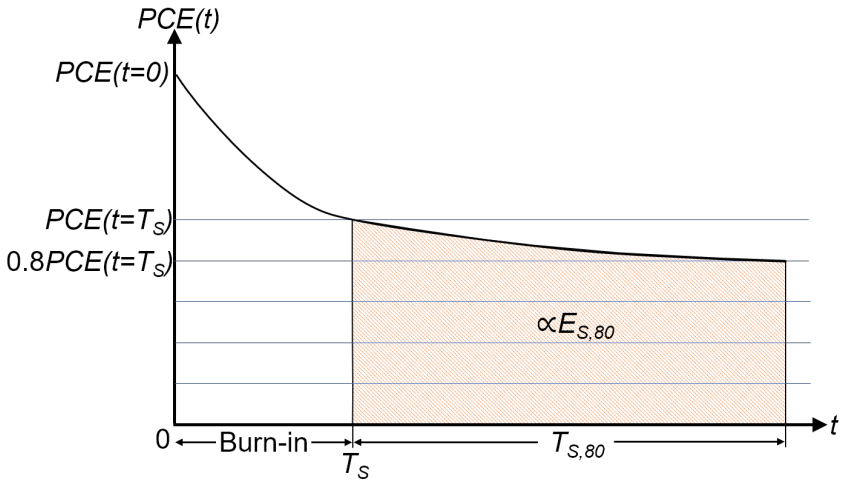

Figure 3.2: **Representative lifetime plot of an OPV with a burn-in period** | PCE as a function of time. The stabilized lifetime is the time between T_S and when PCE reaches 80% of its stabilized value. The shaded area is approximately proportional to $E_{S,80}$.

Table 3.1: **Lifetime, efficiency, and figures of merit for select OPVs** | FoMs and testing conditions of small-molecule OPVs with reported efficiencies and lifetimes are shown. Select polymer cells are included for reference. *SM = thermally evaporated small molecule. †Measured to 9,000 hr with 8% *PCE* loss. ‡Extrapolated from high intensity aging data in Chapter VII.

Year Published	Cell Type*	*PCE* (%)	T_{80}, $T_{S,80}$, or T_{final} (hr)	E_{80} (kWhr/m^2)	*ELP*	Illuminant
2006 [109]	Polymer	1.4	1	0.014	0	Xe arc
2008 [89]	SM Tandem	4.1	1,600	66.7	13.1	Halogen
2010 [96]	SM	0.5	25	0.12	0.7	Blue LED
2011 [110]	Polymer	4.2	4,400	186	15.3	S plasma
2011 [111]	SM	2	1,000	6.7	6	Metal Halide
2012 [112]	SM	2.1	1,800	38.9	6.8	Metal Halide
2012 [97]	SM	2.2	1,500	33.3	7	White LED
2013 [100]	SM	3.2	1,700	55.6	10.3	Xe arc
2013 [113]	Polymer	5.1	250	12.8	12.2	Metal Halide
2014 [114]	Polymer	2.7	12,000	333	11	S plasma
2014 [115]	SM	2.3	700	16.1	6.5	N/A
2017 [105]	Polymer	6.1	1,900	105.6	20	White LED
This work	SM	6.6	9,000†	528	26.1	Xe arc
This work	SM	6.6	99,000‡	4,167	33.0	Xe arc/LED

as *PCE* has historically spanned just over one order of magnitude (1% → 17%) while T_{80} has spanned at least seven (seconds→years). Hence, a FoM called efficiency log-lifetime product (*ELP*) can be used, which gives comparable weight to advances in *PCE* and reliability:

$$ELP = PCE \cdot log_{10}(T_{80}[hr]). \tag{3.3}$$

Literature data from small molecular weight OPVs that report both a lifetime and

PCE can be seen in Table 3.1, along with their E_{80} (or $E_{S,80}$) and *ELP* calculated using Eqs. 3.1, 3.2, and 3.3. Several state-of-the-art polymer devices are also shown for reference, including the current best result for an OPV with a solution-processed NFA. For reference, a 15% *PCE* photovoltaic cell with a 25-year T_{80} (the approximate requirements for commercial applications) would have an $E_{80} > 2 \times 10^{10}$ J/m^2 and an *ELP* of 80.

3.2 Reliability testing methods

Due to their potential sensitivity to light, electrical bias, elevated temperature, and atmospheric O_2 and H_2O, disentangling the contributions of various stressors requires carefully targeted testing. Proper testing and consistent reliability data reporting have therefore been a source of significant discussion over the past several years in the OPV community with several publications outlining consensus OPV stability testing protocols and reporting metrics.[80,82,108] In addition, many techniques have been employed to characterize individual materials for their thermal/morphological stability (differential scanning calorimetry (DSC), thermogravimetric analysis (TGA), atomic force microscopy (AFM), scanning electron microscopy (SEM), x-ray diffractometry (XRD)) and photochemical stability (ultraviolet-visible (UV-vis) absorption spectroscopy, laser desorption ionization time-of-flight (LDI-TOF) mass spectrometry, FTIR spectroscopy, nuclear magnetic resonance (NMR), x-ray photoelectron spectrosopy (XPS), time-of-flight secondary ion mass spectroscopy (TOF-SIMS)), which can be predictive of their stability when integrated into OPVs.

The most common way to measure the intrinsic stability of an OPV is by subjecting it to continuous illumination at its MPP in a pure N_2 atmosphere while periodically measuring its *J*–*V* characteristics. This method has the advantage of being controllable, since the temperature and illumination conditions can be precisely known, and continuous illumination accelerates test duration by $\sim 5\times$ compared

with outdoor testing that is limited to several hours of sun per day. To perform such experiments during this work, we constructed an automated testing environment capable of simultaneously testing 72 OPVs, with integrated temperature control and automated data collection and analysis software. Firstly, all devices are hermetically sealed with two glass slides and a UV-curable epoxy, to ensure that the ingress of O_2 and H_2O is minimized. Here, the epoxy seal is positioned around the periphery of the substrate as shown in Fig. 1.20 where a small gap is left in the metal contacts, since they do not adhere strongly enough to the substrate to create a mechanically sound seal. A 1.5 kW, AM1.5G-filtered Xe arc lamp was used for solar aging, which supplies approximately 1 kW/m^2 illumination over a 10"$\times$ 10" area.

In addition to the light source, automated testing of many cells simultaneously requires a current/voltage source measurement unit (SMU), a multiplexing circuit that connects one device to the SMU at a time, substrate holders with reliable contacts to the OPV, load resistors for each device, a calibrated photodiode to track the intensity of the simulator, and a software package to control the system. The basic circuit employed is shown in Fig. 3.3. Nominally, all relays are in the horizontal position, thus the OPVs are in a series-parallel configuration with a load resistor, R_{load}, chosen to hold the OPV at its MPP. To measure the J–V characteristics of an OPV, its associated relay was closed into the vertical position in Fig. 3.3, thereby

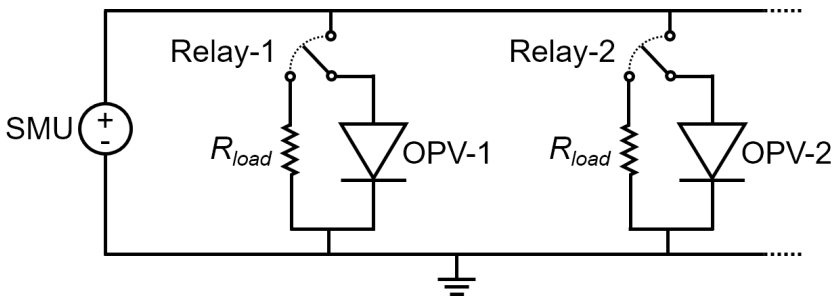

Figure 3.3: **OPV lifetime testing circuit diagram** | Schematic of the circuit employed to age OPVs while connected to an electrical load, and periodically connect them to the SMU for measurement.

connecting it to the SMU. The timing of the relays and SMU measurement sweeps was controlled by the software.

Making mechanically robust and electrically stable contacts to the OPVs is critical for lifetime testing, and is non-trivial since soldering to the ultra-thin Al/Ag OPV electrodes is difficult, and Ag paste does not adhere to thermally evaporated Ag or Al. In this work, custom printed circuit boards (PCBs) (as shown in Fig. 3.4) were used to mount and contact the OPVs. A recessed pocket was designed to fit the OPV substrates with contacts bridging between the OPV electrodes and the Cu PCB contacts using Cu tape as shown in Fig. 3.4 (right). On the OPV side, a conductive Ni paint was used to adhere to the electrode, which was then connected to the Cu tape using Ag paste. The Cu tape was directly soldered to the Cu contacts on the PCB to carry the current out to connection pins. During operation, the PCB was inverted such that the OPVs were illuminated through the hole in the PCB and the contacts were facing away from the light.

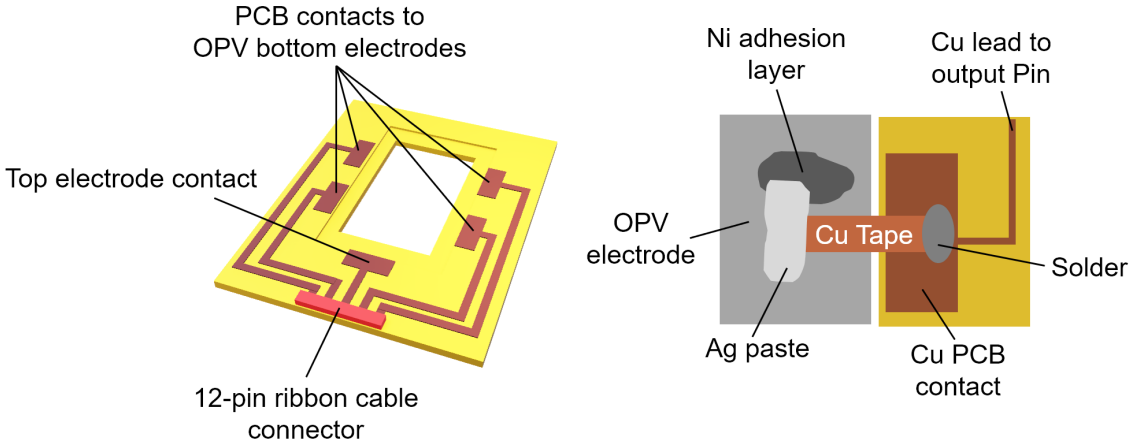

Figure 3.4: **OPV lifetime mounting and contact schematic** | Diagram of the PCB (left) and compound electrical contact (right) used to mount and contact OPVs during lifetime testing.

For testing, the PCBs were mounted to an optics table under illumination from the Xe arc lamp using screws and four teflon standoffs at the corner of the OPVs, as shown in Fig. 3.5. Optionally, a resistive heater and Cu heat spreading plate

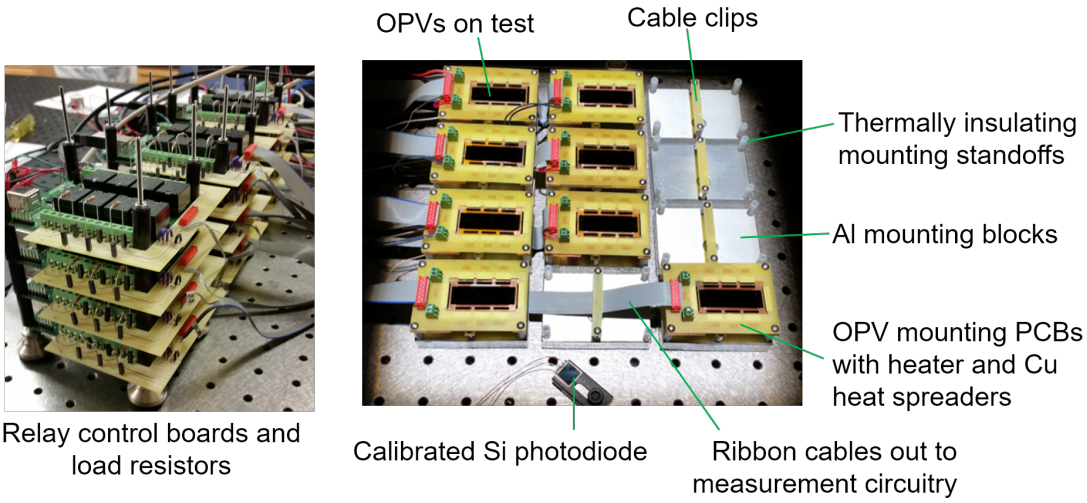

Figure 3.5: **OPV lifetime measurement setup photographs** | Left: Photograph of the 8-channel relay boards, and PCBs that were used to connect the OPVs to the SMU and load resistors. Right: Photograph of OPVs under lifetime testing with key elements of the setup labeled.

could be mounted between the PCB and the standoffs to heat the OPV substrate. Teflon standoffs were chosen for this reason, since they thermally insulate the Cu heat spreader from the bench, allowing the system to reach higher temperatures ($> 130°C$). To prevent the heaters from melting the ribbon connector cables, clips are placed under each substrate holder for cable routing, as shown in Fig. 3.5. Each substrate was assigned an 8-channel relay board (Fig. 3.5 (left)) that implemented the circuit diagrammed in Fig. 3.3. Power for the relays and resistive heaters was supplied by an external DC power supply.

Finally, the relay boards and SMU were interfaced to a computer using USB and GPIB connectors, respectively. A control software package was written to automate OPV testing, and log and analyze the performance data (PCE, J_{SC}, V_{OC}, FF, R_S, and R_{SH}) of each OPV vs. time. Screen captures of the graphical user interfaces (GUIs) used to control the tests and compile data are shown in Fig. 3.6. The output power of the Xe lamp was measured continuously with a calibrated Si photodiode as shown in Fig. 3.5.

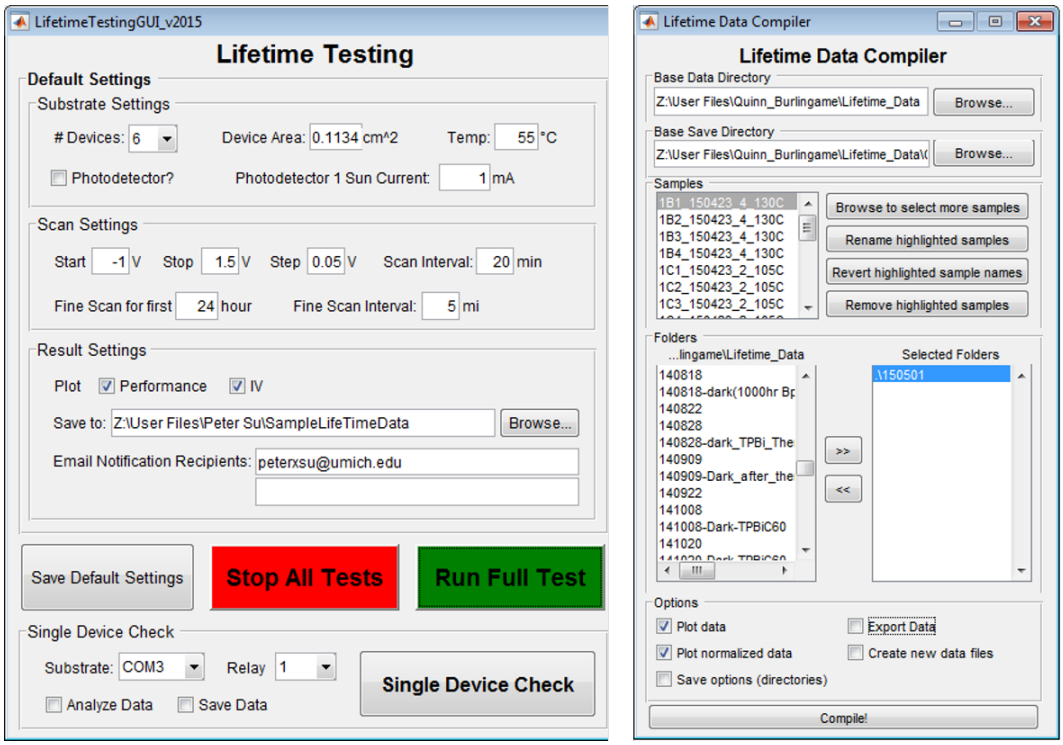

Figure 3.6: **OPV lifetime testing software GUIs** | Screen captures of the GUIs used to control lifetime testing of OPVs (left) and compile their performance data (right).

The measurement circuitry and contacts using this method were able to maintain reliable performance for several thousand hours under test, including at elevated temperatures up to 130°C. The most significant instability was in the spectrum of the Xe lamp, which continuously red-shifts over its lifetime, as shown in Fig. 3.7. Due to its strong near-IR absorption, the Si photodiode used to calibrate the lamp intensity produced a constant photocurrent despite this red shift, while the OPVs, which absorb strongly from 400-700 nm, collected less photons. This creates the false appearance of J_{SC} loss in the OPVs, as shown in Fig. 3.7.[81] As a result, constant monitoring of the Xe spectrum and cross-calibration of the OPV performance during measurement is required to accurately determine J_{SC}. Alternative light sources such as sulfur plasma lamps, Hg arc lamps, metal halide lamps, and white light emitting diodes (LEDs) can also be used for continuous OPV aging experiments.[108] However,

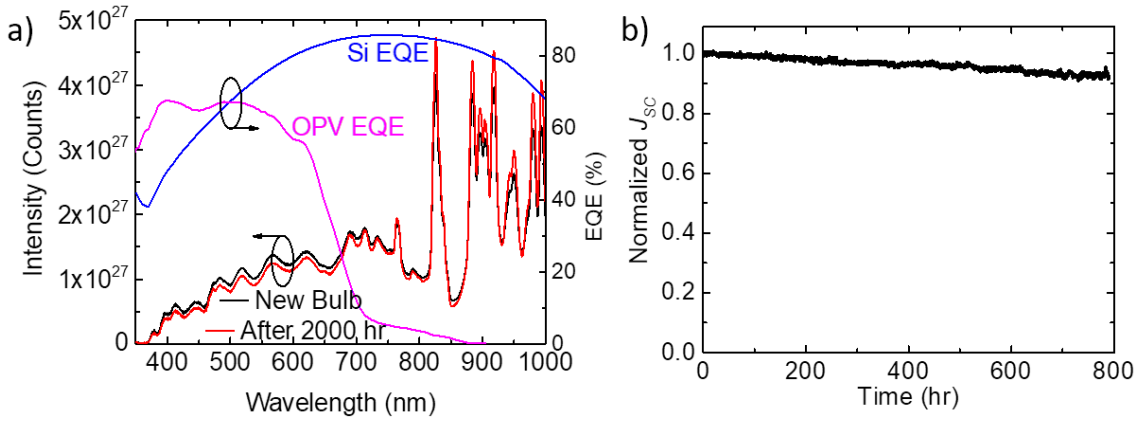

Figure 3.7: **Effects of Xe arc lamp instability | a)** (left-axis) Intensity of the Xe arc lamp used for OPV aging before and after running for 2000 hr. (right axis) *EQE* of a typical OPV and the Si photodiode used to calibrate the intensity of the Xe arc lamp. **b)** Trend in apparent J_{SC} of the OPV as the Xe lamp red-shifts, from Q. Burlingame *et al.* (2016).[81]

the spectral match of sulfur plasma and Hg arc lamps with AM1.5G is poor, and large area white LED sources are not yet commercially available at low cost. Once they become cost competitive, LED simulators are likely the best available source for solar aging studies due to their excellent stability, high efficiency, and spectral tunability.

While continuous aging experiments provide a controlled environment for evaluating intrinsic stability, outdoor lifetime measurements expose cells to a broader range of conditions are experienced during practical operation, including light and thermal cycling, variations in humidity, and weather. Several outdoor aging studies have been performed on solution-processed polymer solar cells,[116–119] while few reports exist describing small-molecule OPV outdoor lifetimes.[81] The outdoor lifetime measurements in this work were performed in Sede Boqer, Israel, using a 30° fixed-angle testing station with a reference Si detector, as shown in Fig. 3.8. The OPVs were mounted and contacted using the same PCBs and methods described for continuous illumination aging. Compared with indoor tests, outdoor tests show a higher incidence of catastrophic failure, due to the additional stress placed on the encapsulation materials during outdoor measurements. Outdoor measurements also

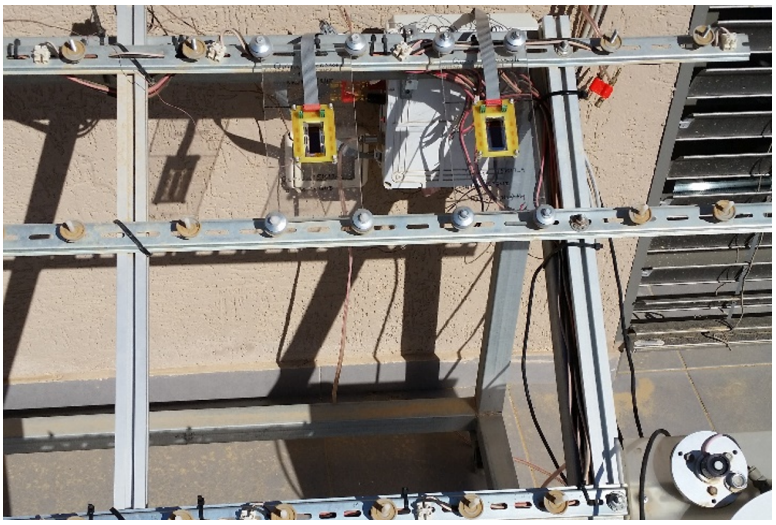

Figure 3.8: **Outdoor OPV reliability measurement setup** | Photograph of two OPV substrates aging outdoors in Sede Boqer, Israel on a fixed angle (30°) platform with a reference Si photodiode.

introduce potential uncertainty, due to the high variance in conditions at different locations, and provide no acceleration (unlike continuous aging and accelerated aging experiments).

3.3 Accelerated aging

Over the past several years, reports of OPVs with lifetimes greater than several months have become frequent.[81,105,110,114] As this trend continues, and perhaps accelerates, assessing device operational lifetimes *via* continuous illumination and outdoor testing will no longer be feasible on a practical timescale. Accelerated aging methods are therefore required, with an ideal accelerated test simply speeding up the intrinsic failure modes that exist under normal outdoor operation, rather than inducing new extrinsic degradation.

3.3.1 Theory and acceleration factor

Two possible stressors for accelerating OPV aging are temperature and light intensity. Thermally accelerated aging seeks to accelerate the rate of change of a device parameter, p, which degrades over time, t, as a function of temperature, T, as follows:[120]

$$p(t) = \alpha \exp\left(-k_{deg}(T)t\right) + \beta, \tag{3.4}$$

where α and β are constants. Here, $k_{deg}(T)$ is a thermally activated degradation rate with an Arrhenius temperature dependence:

$$k_{deg}(T) = A \exp\left(\frac{-E_A}{k_B T}\right), \tag{3.5}$$

where A is a constant and E_A is the activation energy of the degradation process.

High intensity aging can potentially provide valuable information about what mechanisms drive performance loss since it can increase the rate of photochemical reactions and produce large densities of electrons, polarons, and phonons. The rate of photochemical degradation, for example, will increase linearly with intensity,[102,121,122] while the rate of degradation due to multiple particle interactions (*e.g.*, exciton–exciton, polaron–polaron, and exciton–polaron) will increase quadratically.[123–125] When aging under high intensities and temperatures, it is useful to define an acceleration factor, γ, linking the accelerated degradation rate, k_{acc}, to the degradation rate, k_{ref}, under standard operating conditions:[120]

$$\gamma = \frac{k_{acc}}{k_{ref}} = \left(\frac{I_{acc}}{I_{ref}}\right)^{\xi} \exp\left(\frac{E_A}{k_B}\left[\frac{1}{T_{acc}} - \frac{1}{T_{ref}}\right]\right), \tag{3.6}$$

where I_{acc} is the intensity during the accelerated test, I_{ref} is the intensity under standard operation, E_A is the Arrhenius activation energy, and T_{acc} and T_{ref} are the operating temperatures during accelerated and standard aging. The exponen-

tial factor, ξ, can be fit empirically, and will depend on the relative contribution of photochemical ($\xi = 1$) and multiple particle ($\xi = 2$) degradation modes.

3.3.2 Experimental methods

In this work, both thermal and high intensity acceleration are used, depending on the device architecture and its active failure modes. For thermal testing, devices were aged using the continuous illumination setup described in §3.2. The temperature of each device was monitored with a thermocouple attached to the front surface of the OPV and was modulated by controlling the current to a resistive heater attached to the Cu heat spreader on each device. The temperature was maintained within 1°C of the desired temperature by a computer integrated proportional–integral–derivative (PID) controller.

High intensity illumination was applied to OPVs using two sources: concentrated sunlight, and high intensity white LEDs. Concentrated sunlight was collected using a 2-axis solar tracker in Sede Boqer, Israel, and was focused into a 1 mm diameter quartz optical fiber with a parabolic reflector.[126] A multimode quartz block was placed between the fiber and the OPV to distribute the illumination over the entire device area. Intensity was calibrated using a calibrated pyranometer, and controlled with a shutter/iris.[127,128] Experiments were limited to several hours around mid-day, and could only be performed during clear skies where the spectrum was nearly time invariant and similar to AM1.5G.[129] The OPVs were actively cooled with a thermoelectric cooler during aging.

To conduct high intensity aging experiments at the University of Michigan, we constructed a system with white LEDs and integrated water cooling as shown in Fig. 3.9. The four LEDs in the system were controlled by independent power ballasts, with adjustable output power. Light from the LEDs was collimated onto the OPVs with Ag-coated high-temperature polycarbonate (PC) tubes, as shown in the right

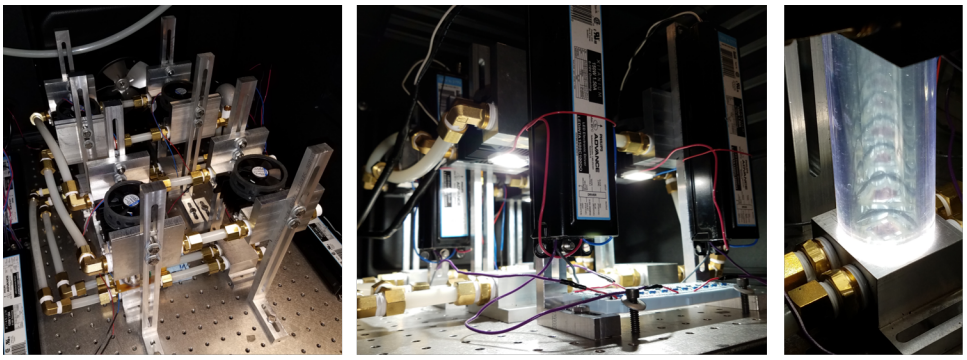

Figure 3.9: **High intensity LED aging setup photographs.**

photograph in Fig. 3.9. Chilled H_2O flowed through Al blocks beneath each OPV's substrate to cool them. The LEDs were mounted to Al heat sinks attached to cooling fans. These heat sinks were connected to hollow Al blocks with chilled H_2O flowing through them for additional LED cooling.

The LED spectrum extended from 420 nm to 700 nm with a correlated color temperature (CCT) of 5000K as shown in Fig. 3.10. The equivalent solar intensity of the LEDs was calibrated by measuring the J_{SC} of a fresh OPV in response to

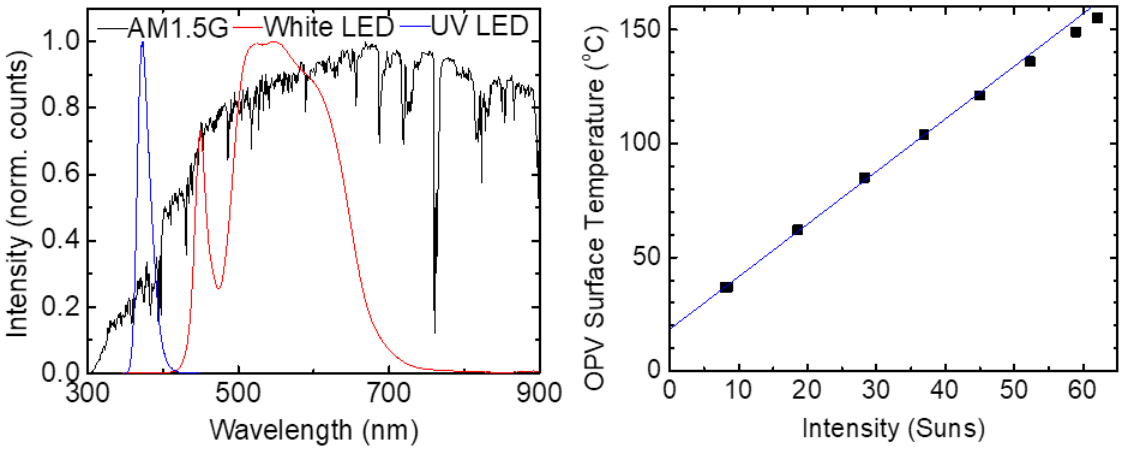

Figure 3.10: **Performance characterization of the LED aging setup** | Left: Normalized spectra of the high intensity white and UV LEDs used to accelerate OPV aging compared to the normalized AM1.5G spectrum. Right: Equivalent solar intensity vs. OPV surface temperature under high intensity LED illumination.

the LED illumination incident through a neutral density (ND) filter. The ND filter had an optical density (OD) of 1, thus an LED intensity that produced an OPV photocurrent equal to 10% of the OPV's 1-sun J_{SC} under AM1.5G was said to be 1 sun of equivalent intensity. The ND filter was used during calibration to keep the OPV current and temperature low during calibration as J_{SC} becomes non-linear at higher intensities and changes as a function of temperature.[130] The Al heat sinks had a base temperature of 12°C, though the temperature of the OPVs increased almost linearly with intensity as shown in Fig. 3.10. The maximum equivalent solar intensity the system could produce was > 60 suns. A removable UV LED source capable of delivering > 100 suns of UV illumination was also included in the system, with the spectrum shown in Fig. 3.10. The intensity of the UV LED was calibrated by measuring its irradiance and dividing it by the total irradiance of AM1.5G at $\lambda < 400$ nm, which is approximately 4.6 mW/cm^2.

CHAPTER IV

Photostability of organic thin films and photovoltaic cells

4.1 Optical and Fourier transform infrared spectroscopy

The photostability of the individual materials and thin films that comprise an OPV can be predictive of the stability of the OPV itself—particularly if the stability of the constituents is poor.[81,101,102] A simple method to screen for stability is to age thin films under various conditions, and measure the change in their UV-vis absorption or FTIR spectra. These optical techniques are useful for detecting large changes, where a significant portion of the molecules ($\gtrsim 1\%$) in the film have degraded. Infrared spectroscopy is particularly useful, since certain regions of the spectrum correspond to specific bonds, functional groups, and vibrational modes, and can thus be used to identify how molecules change with time. In this work, 13 common OPV materials were screened for stability by measuring the FTIR absorption spectra of 100 nm thick films on KBr before and after aging for 1 week under different atmospheric and illumination conditions: in the dark in N_2; in the dark in air; under simulated 1-sun illumination in N_2; and under simulated 1-sun illumination in air. The study included donor materials (DBP, DTDCPB, DTDCTB, and SubPc), acceptor materials (C_{60} and C_{70}), buffer materials (3TPYMB, Alq_3, BAlq, BP4mPy, BPhen, and TPBi), and

PTCBI that has been used previously as both an acceptor and an exciton blocker. Structural formulae of each of these compounds are shown in Fig. 4.1, and their full chemical names are included in the List of Chemicals.

The full FTIR spectra are shown in Appendix A and the results are qualitatively summarized in Table 4.1. Interestingly, none of the spectra showed any change after aging in the dark either in N_2 or air, except for BPhen which had visibly crystallized after aging. Under illumination in air, the polar molecules (3TPYMB, Alq_3, BAlq, DTDCPB, DTDCTB, SubPc, and TPBi) were hygroscopic, while thin films of BP4mPy, BPhen, C_{60}, C_{70}, DBP, and PTCBI showed no evidence of H_2O ingress. Almost all materials showed some level of oxidation after aging under illumination in air, as evidenced by the formation of an FTIR absorption peak around 1750 cm^{-1} (associated with the stretching mode of the C–O double bond), with the exception of BP4mPy that remained totally stable under all aging conditions.

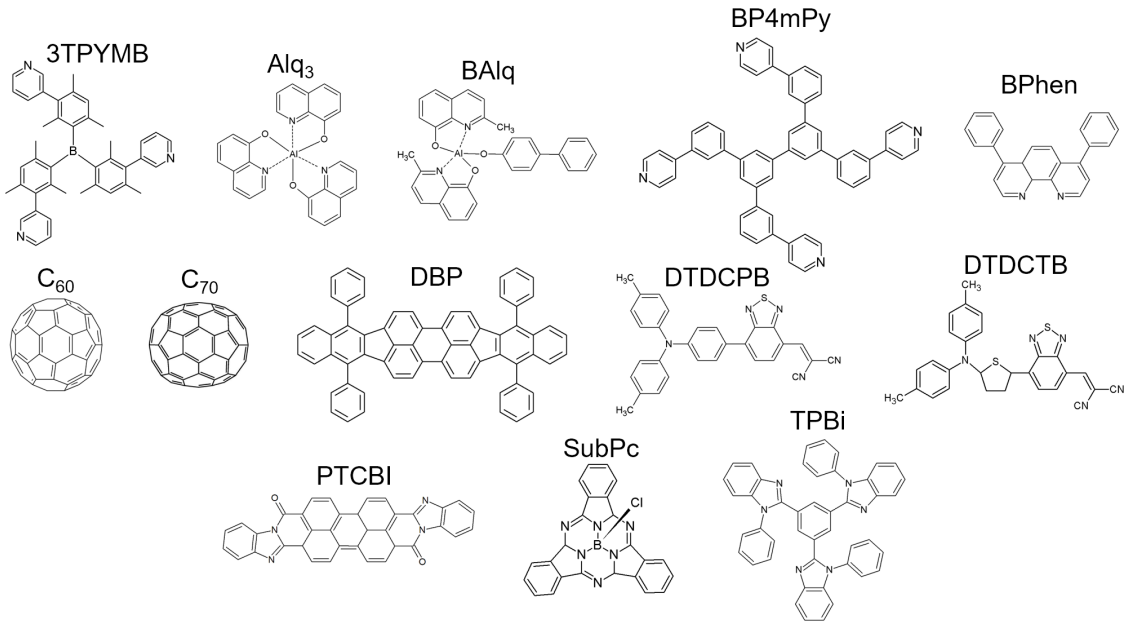

Figure 4.1: **Structural formulae of OPV materials.**

Table 4.1: **Summary of thin film stability from FTIR absorption spectra** | Full spectra are shown in Appendix A. Thin films of each material were aged for 1 week at the stated conditions: Dark/N_2, Dark/air, 1-sun/N_2, 1-sun/air. Ingress of H_2O and oxidation were inferred from the presence of an increased H_2O background and the formation of modes around 1750 cm^{-1}, respectively.

Material	Dark/N_2 stability	Dark/air stability	1-sun/N_2 stability	1-sun/air stability	C–O formation	H_2O ingress
3TPYMB	good	good	good	poor	weak	strong
Alq_3	good	good	good	poor	strong	strong
BAlq	good	good	good	poor	strong	strong
BP4mPy	good	good	good	good	none	none
BPhen	ok	ok	ok	poor	strong	none
C_{60}	good	good	poor	poor	strong	none
C_{70}	good	good	good	ok	weak	none
DBP	good	good	good	poor	strong	none
DTDCPB	good	good	good	poor	weak	strong
DTDCTB	good	good	good	poor	weak	strong
PTCBI	good	good	good	ok	weak	none
SubPc	good	good	good	poor	strong	strong
TPBi	good	good	good	poor	poor	strong

4.1.1 Oligomerization in C_{60} films and heterojunctions

Without the presence of H_2O and O_2, the organic thin films aged in N_2 under illumination were stable with the exception of C_{60}, which underwent significant chemical changes. The vibrational spectrum of C_{60} has been explored both computationally and experimentally,[102,121,131,132] with four of its 174 vibrational modes satisfying the condition: $d\mu/dr \neq 0$, where μ is the dipole moment and r is the nuclear displacement during the vibration. These four modes can therefore couple to

IR radiation, and appear at 526, 575, 1182, and 1429 cm^{-1} in Fig. A.6. These peaks are significantly reduced after aging under illumination in N_2, and a number of new peaks emerge between 550 and 800 cm^{-1}. These changes are consistent with fullerene photo-oligomerization—where light-induced chemical bonds are formed between adjacent C_{60} molecules, thus creating C_{120}, C_{180}, and longer oligomers as evidenced by LDI-TOF mass spectrometry studies.[121,131] The new infrared (IR) absorption peaks that emerge betwen 550 and 800 cm^{-1} are associated with new vibrational modes of the oligomers. Since the formation of oligomers breaks the symmetry responsible for C_{60}'s long exciton lifetime ($\tau > 1$ μs),[133] solution-based exciton lifetime measurements have found that the recombination rate is significantly faster than that of the monomer.[134–136]

Using the four characteristic C_{60} FTIR modes as a fingerprint, *in situ* time-dependent FTIR absorption spectra were measured on planar and blended SubPc:C_{60} HJs over a 24 hour period, as shown in Fig. 4.2.[102] Over the course of the measurement, light from a Xe arc lamp was focused into a broadband liquid light guide to soak the C_{60} film inside the FTIR tool, which was continuously purged with N_2. The FTIR absorption spectra of 100 nm thick films of SubPc and C_{60} are plotted for reference, and scaled to represent the amount of each material in the HJ. As we can see, the FTIR spectra of the as-grown HJs are linear superpositions of the as-grown neat C_{60} and SubPc spectra. Over time, the four characteristic C_{60} peaks (529, 575, 1182, and 1429 cm^{-1}) become smaller in both HJs, while the oligomer peaks between 550 and 800 cm^{-1} become more pronounced.

To more quantitatively assess the formation of C_{60} oligomers from these spectra, the peak heights from the four C_{60} FTIR peaks were extracted as a function of time and normalized to their initial values as shown in Fig. 4.3.[102] In the planar HJ, the decrease was relatively rapid and continued to decrease throughout the 24 hr measurement. After 24 hr, the peak heights degraded to 29% to 53% of their starting

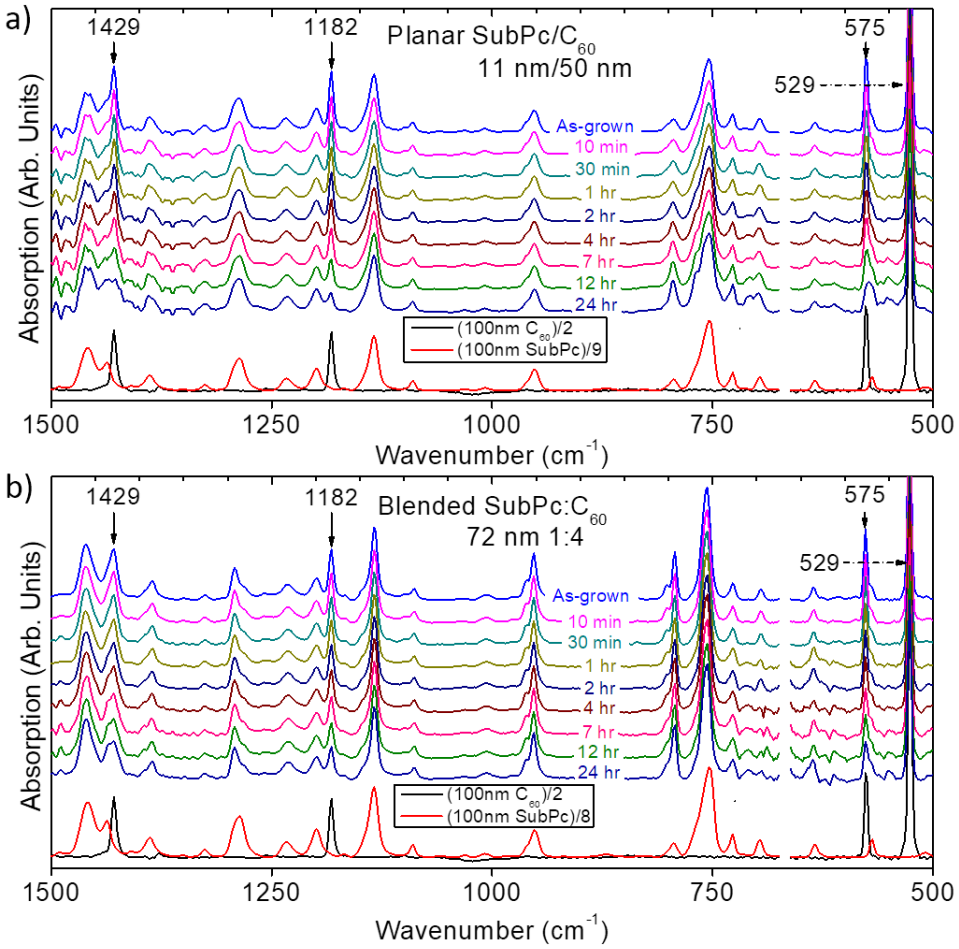

Figure 4.2: ***In situ* FTIR spectra on SubPc:C_{60} HJs** | Time-resolved FTIR spectra of a **a)** planar 50 nm C_{60}/11 nm SubPc HJ and **b)** blended 72 nm SubPc:C_{60} 1:4 HJ grown on KBr while being exposed to Xe arc lamp illumination. Neat SubPc and C_{60} spectra are shown for reference, and scaled to match the amount of each compound in the HJs.

values. In the blended HJ, the peak heights decreased more slowly, and appeared to saturate after about 10 hr—maintaining between 63% and 79% of their initial intensity after 24 hr.

Finally, the photochemical instability of C_{60} is apparent from its UV-vis absorption spectra, as shown in Fig. 4.4. After aging for 1 week in N_2 under 100 mW/cm^2 Xe arc lamp illumination, the absorbance of the film broadens significantly.[101,102,122] Under the same treatment, a 100 nm thin film of SubPc shows no change.[101,102]

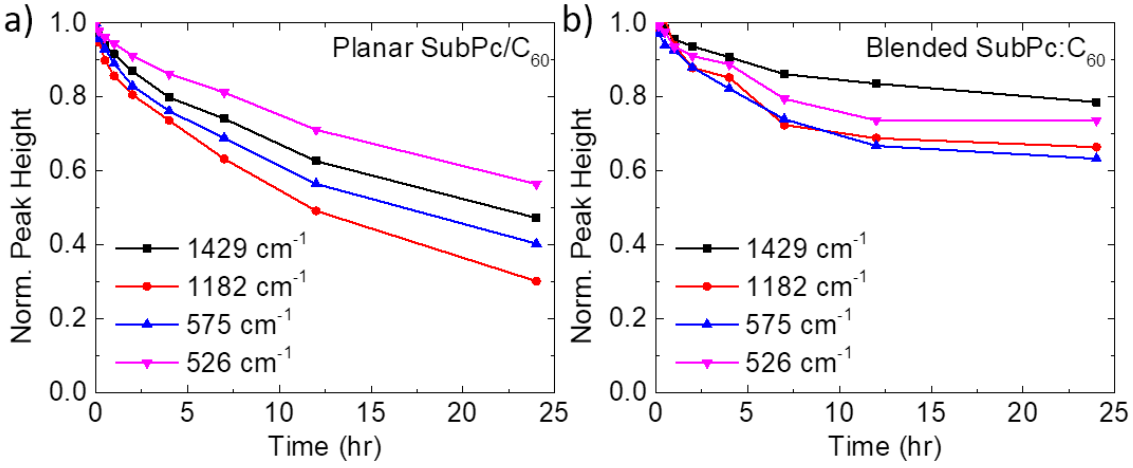

Figure 4.3: **Time-resolved C_{60} FTIR peak heights in HJs** | Normalized magnitude of the four C_{60} FTIR absorption peaks extracted from Fig. 4.2 as a function of time for the **a)** planar SubPc/C_{60} HJ and the **b)** blended SubPc:C_{60}. Adapted from Q. Burlingame *et al.* (2015).[102]

4.2 Burn-in of planar C_{60} organic photovoltaic cells

As we have shown, C_{60} thin films rapidly oligomerize when exposed to light which changes their photophysical, electrical, and optical properties in several ways that are relevant to photovoltaic performance. Unsurprisingly, thermally evaporated pla-

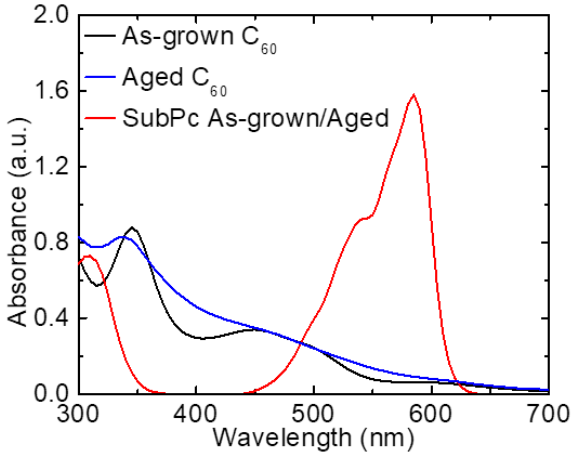

Figure 4.4: **Absorbance of C_{60} and SubPc after solar aging** | Wavelength-dependent absorbance of 100 nm thin films of SubPc and C_{60} before and after aging for 1 week under simulated solar illumination in N_2. No change was observed in the absorbance of the SubPc film. Adapted from Q. Burlingame *et al.* (2015).[102]

nar HJ OPVs[96,98,100,102,115,122] and their solution-processed counterparts containing $PC_{61}BM$[99] are largely unstable. Planar SubPc/C_{60} HJ OPVs, with the structure shown in Fig. 4.5a, experience a rapid burn-in period during the first several hours under illumination, where $> 30\%$ of the initial J_{SC} is lost.[100] The loss in photocurrent during aging in these devices occurs disproportionately where C_{60} absorbs more light than the SubPc donor (as shown in Fig. 4.5b, confirming that the photocurrent contribution from the C_{60} layer diminishes over time and is therefore responsible for the degradation. Furthermore, burn-in was shown by X. Tong *et al.* (2013)[100] to proceed linearly with the number of absorbed photons, independent of wavelength, suggesting that excitons drive burn-in that is consistent with previous studies on C_{60} oligomerization.[121] Interestingly, blending C_{60} and SubPc was found to totally eliminate burn-in by X. Tong *et al.* (2013),[100] despite the fact that here we observed evidence of significant C_{60} oligomerization in the FTIR spectra of blended SubPc:C_{60} HJs, as shown in Figs. 4.2 and 4.3.

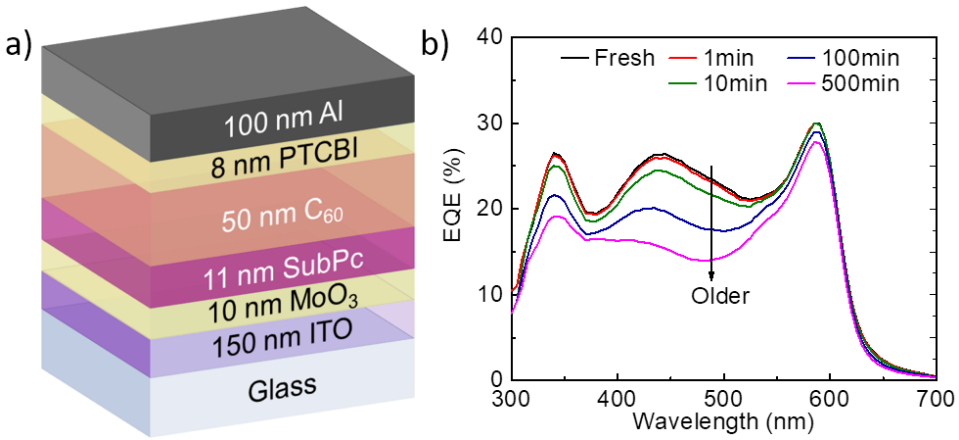

Figure 4.5: **Time-resolved *EQE* of a planar HJ SubPc/C_{60} OPV** | **a)** Structure of a planar HJ SubPc/C_{60} OPV with a PTCBI cathode buffer layer. **b)** Time-resolved *EQE* spectra of the device shown in **a)** while aging under 100 mW/cm^2 simulated solar illumination. Adapted from Q. Burlingame *et al.* (2015).[102]

4.2.1 Theory and exciton diffusion modeling

From §1.1.8, recall that a key advantage of blended donor-acceptor HJs is their lack of dependence on the exciton L_D of the constituents since the HJ is distributed everywhere. If the L_D of C_{60} decreased during oligomerization, it would therefore degrade the performance of a planar HJ OPV, without affecting the performance of blended HJ devices. To quantify this effect, consider the steady-state exciton diffusion equation (Eq. 1.11) in one spatial dimension, x, which is the distance from the HJ:

$$D\frac{\partial^2 N(x)}{\partial x^2} - k_{loss}N(x) + G(x) = 0, \tag{4.1}$$

where $k_{loss} = 1/\tau$ is the exciton recombination rate. The transfer matrix method can be used to calculate the light-induced exciton profile,[137] and Eq. 4.1 can be solved to find the exciton flux to the HJ, which is proportional to EQE and therefore J_{SC}. In the planar C_{60} HJ case, the formation rate of oligomers should be proportional to the exciton density, and the presence of oligomers effectively increases k_{rec}. The C_{60} monomer fraction remaining as a function of time and position, $\Gamma(x,t)$, can be expressed as:

$$\Gamma(x,t) = \frac{M(x,t)}{M_0} = (1-\Gamma_\infty)\exp[-k_F N(x,t)] + \Gamma_\infty, \tag{4.2}$$

where $M(x,t)$ is the monomer density, M_0 is the initial monomer density, k_F is the oligomer formation rate, and Γ_∞ is the percentage of monomers remaining at $t = \infty$. If we include the impact of monomer formation and recombination, Eq. 4.1 on the C_{60} side of the HJ becomes dependent on the aging time, t:

$$D\frac{\partial^2 N(x,t)}{\partial x^2} - \left[(k_1 + k_F)\Gamma(x,t) + k_{2+}(1-\Gamma(x,t))\right] N(x,t) + G(x,t) = 0, \tag{4.3}$$

where k_1 and k_{2+} are the recombination rates on C_{60} monomers and oligomers respectively. Since literature reports show that the lifetime of oligomers does not continue to decrease for longer chains (*i.e.*, $C_{120} \approx C_{180}$, etc.), only one rate, k_{2+}, is required to represent all non-monomers.

In order to use Eq. 4.3 to simulate *EQE* as a function of degradation, the diffusivities of SubPc and C_{60} excitons and their recombination rates were taken from the literature (SubPc: $D = 3.2 \times 10^{-4}$ cm^2s^{-1},[138] $k_{rec} = 5 \times 10^8$ s^{-1} [139] and C_{60}: $D = 1.6 \times 10^{-5}$ cm^2s^{-1},[18] $k_1 = 1 \times 10^6$ s^{-1})[133]. While exciton recombination rates have been measured for C_{120} and C_{180} in solution *via* transient absorption spectroscopy,[134–136] no measurements of k_{2+} or k_F have been reported for thin films. To fit these parameters, it is useful to find a portion of the *EQE* spectrum that has no contribution from SubPc, and where C_{60}'s absorption is constant. From the absorption spectra in Fig. 4.4, we can see that $\lambda = 450$ nm meets these requirements. This can also be inferred from the aged *EQE* spectra (Fig. 4.5b) as *EQE* loss is maximized near $\lambda = 450$ nm.

As $t \to \infty$, the J_{SC} loss saturates as the oligomer density reaches its maximum, Γ_∞. Even so, a significant portion of the photocurrent contribution from the C_{60} layer remains, as evidenced by the remaining *EQE* contribution at $\lambda = 450$ nm. This, therefore, implies a certain exciton L_D in the oligomerized C_{60} layer, which is a function of k_{2+} and Γ_∞, and is lower than the L_D in the as-grown acceptor layer. However, these paramaters cannot be determined independently since many (k_{2+},Γ_∞) pairs can produce the same L_D. As a starting point, we therefore assume that $\Gamma_\infty = 0$, and solve Eq. 4.3 at $t \to \infty$ with respect to the boundary conditions: 1) complete quenching at the SubPc/C_{60} interface, *i.e.*, $N(x) = 0$; and 2) ideal exciton blocking at the C_{60}/PTCBI interface, *i.e.*, $\partial N(x)/\partial x = 0$. The value of k_{2+} was then varied until the value of the simulated *EQE* and measured *EQE* at $\lambda = 450$ nm was minimized as shown in Fig. 4.6, which occurred at $k_{2+} = 5.8 \pm 0.4 \times 10^6$ s^{-1}. Using this value

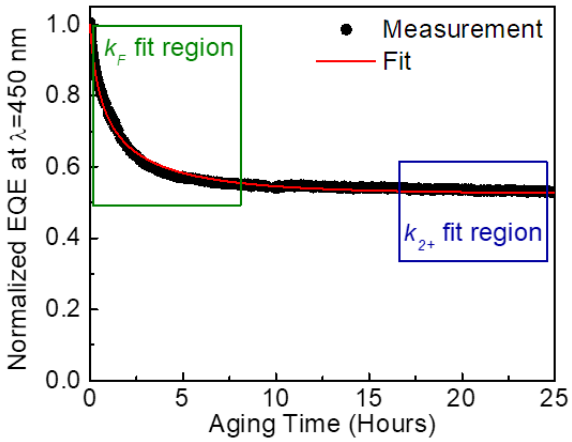

Figure 4.6: **Time-resolved SubPc/C_{60} *EQE*** | Normalized *EQE* at $\lambda = 450$ nm as a function of time for a planar HJ SubPc/C_{60} OPV aging under 100 mW/cm^2 simulated solar illumination, fitted using Eq. 4.3 and the method described in §4.2. Adapted from Q. Burlingame *et al.* (2015).[102]

of k_{2+}, the value of k_F can then be fit by simulating the *EQE* at $\lambda = 450$ nm with Eq. 4.3 as a function of time, and varying K_F to match the measured *EQE* trend as shown in Fig. 4.6. This method produces a value of $K_F = 80$ s^{-1}.

Returning to the inseparability of k_{2+} and Γ_∞, the fully transformed C_{60} film (containing both monomers and oligomers) will have an effective exciton lifetime, τ_{eff}:

$$\tau_{eff} = \left[k_1\Gamma_\infty + k_{2+}(1-\Gamma_\infty)\right]^{-1}, \tag{4.4}$$

with a corresponding exciton L_D:

$$L_D = \sqrt{D\tau_{eff}}. \tag{4.5}$$

Plugging in $k_{2+} = 5.8 \pm 0.4 \times 10^6$ at $\Gamma_{infty} = 0$ produces an $L_D = 16.6 \pm 0.1$ nm, compared with $L_D = 40$ nm in the fresh layer. Therefore, any (k_{2+},Γ_∞) pair that produces an $L_D = 16.6 \pm 0.1$ nm would have an identical effect on photocurrent generation from the C_{60} layer. To illustrate this effect, several $1/k_{2+}$ vs. Γ curves are plotted in Fig. 4.7 with each line representing a distinct L_D as noted. A vertical

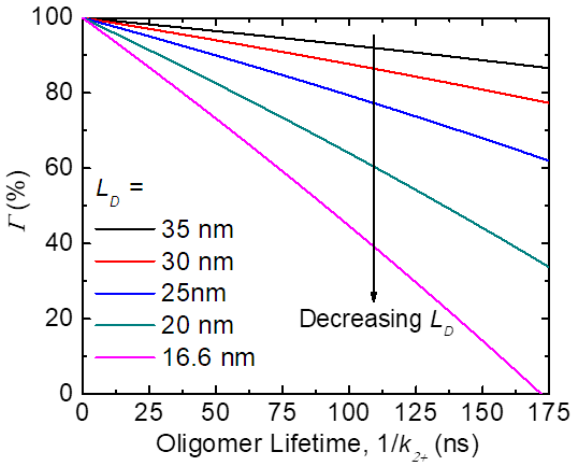

Figure 4.7: **C_{60} film exciton lifetime vs. monomer density** | Exciton lifetime of C_{60} oligomers (k_{2+}) vs. remaining monomer concentration (Γ), showing several curves that respresent constant exciton L_D's in films containing both monomers and oligomers. Adapted from Q. Burlingame *et al.* (2015).[102]

path downward on the plot in Fig. 4.7 corresponds to device aging, where L_D and Γ decrease until reaching the final $L_D = 16.6 \pm 0.1$ nm.

4.2.2 Mass spectrometry on aged C_{60} heterojunctions

To attempt to experimentally determine the values of k_{2+} and Γ_∞, LDI-TOF mass spectra were collected from a 50 nm C_{60}/11 nm SubPc HJ before and after aging for 1 week under 100 mW/cm^2 simulated solar illumination to ensure that burn-in had saturated. To prepare the samples for measurement, they were dissolved in toluene and pipetted onto the mass spectrometry measurement puck. The fresh HJ dissolved completely within seconds. While soaking the aged HJ, its SubPc layer rapidly dissolved, while the C_{60} layer partially remained even after soaking for $>$ 1 hr—indicative of the presence of oligomers.[121] The remaining film was scraped into the toluene to ensure that any monomers present in the film were dissolved. Given their densities and thicknesses (SubPc = 11 nm, 1.53 g/cm^3 and C_{60} = 50 nm, 1.65 g/cm^3), the expected ratio of C_{60} molecules to SubPc molecules, assuming

their desorption and ionization rates are comparable, is 2.93. Dividing the measured counts of C_{60} at 720 m/z by the measured counts of SubPc at 431 m/z produced a ratio of 3.27 in the fresh sample. In the aged sample, this ratio was reduced to just 0.34 despite the magnitude of the SubPc peak remaining constant, suggesting that a majority of the C_{60} monomers were oligomerized. Taking the ratio of the final and initial C_{60}/SubPc ratios, Γ_∞ is found to be $10.4 \pm 0.2\%$. Plugging this value into Eq. 4.5 at $L_D = 16.6 \pm 0.2$ nm produces a corresponding oligomer lifetime of $1/k_{2+} = 156 \pm 2$ ns—nearly 6.5 times shorter than the measured exciton lifetime of pristine C_{60}.[133]

4.2.3 Comparison to previous reports

Beyond this work, several hypotheses have been advanced to explain burn-in phenomena in planar HJ C_{60}-based OPVs. H. Zhang *et al.* (2014)[122] proposed that burn-in may result from reduced charge extraction efficiency if the mobility of aged C_{60} films was less than that of pristine C_{60}. However, such an effect would be apparent in the R_S of the OPV and would primarily degrade *FF* instead of J_{SC}. Indeed, X. Tong *et al.* (2013)[100] shows almost no loss in *FF* during burn-in. Similarly, V_{OC} is also stable compared to J_{SC} during early aging, which implies that the loss is not due to recombination of generated charges, but rather the loss precedes the charge generation process.

The analysis contained here also differs from that of X. Tong *et al.*, which modeled burn-in as the result of a sparse population of exciton quenching sites forming during early aging. While such a model can also fit the data—and indeed is one extreme of the diffusion length model proposed here (where $k_{2+} \to \infty$ and $\Gamma_\infty \to 0$)—it does not account for the significant changes observed in the FTIR absorption, UV-vis absorption, and mass spectra of aged C_{60} thin films. Additionally, the models differ in their interpretation of the self-limiting saturation observed in burn-in and the lack

of burn-in in mixed HJ SubPc:C_{60} OPVs, as X. Tong *et al.* implies that saturation may result from the large capture radius of the quenching sites, which thus eliminates the excitons needed to create additional defects. However, such an effect would also quench all excitons and drive the photocurrent contribution of the C_{60} layer to 0—an effect clearly not observed from the *EQE* spectra. Finally, X. Tong *et al.* hypothesizes that burn-in is not observed in blended HJs because the long-lived excitons required to form defect sites are quenched by the donor/acceptor HJ. In this work, we find direct chemical evidence for the presence of C_{60} photochemical transformations *via* FTIR even in blended HJs. Thus, only the exciton L_D model described here is consistent with the entire set of observations associated with burn-in.

CHAPTER V

Morphological stability in exciton-blocking, electron-filtering compound buffer layers

Under the stress of continually varying temperatures and light intensities during the operation, OPVs may undergo morphological changes with time.[81,87,98,140–142] Most commonly, morphological changes are due to crystallization when the device is operating at or near the glass-transition temperature (T_G) of one of the constituent molecules. Such processes are associated with large changes in dark current, degradation of *FF* and Voc, and even catastrophic failure *via* short-circuiting of the OPV.[87,140] Developing OPVs that maintain a stable morphology throughout their operational lifetime is therefore essential to realizing long-lifetime devices.

5.1 Structural phases and crystal growth theory

In general, thermally evaporated small molecule films grow in either an amorphous or semi-crystalline phase, which sits at a higher enthalpy than the crystalline phase (if such a phase exists), as shown in Fig. 5.1a. Since the crystal is energetically preferred to the amorphous phase (with a Gibb's free energy difference, ΔG_v), crystal nucleation and growth will naturally proceed if the molecules are sufficiently free to re-orient and move—which occurs as the temperature approaches the T_G, as shown

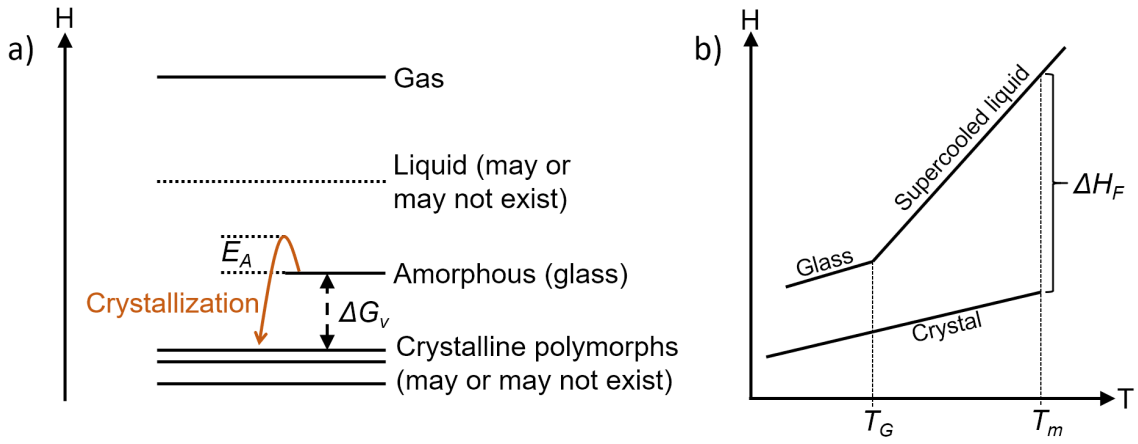

Figure 5.1: **Structural phases of small molecules** | **a)** Simplified phase diagram of a small molecular weight compound as a function of enthalpy, H. The activation energy for crystallization, E_A, and free energy difference, ΔG_v, between the amorphous and crystalline phases are shown. **b)** Idealized temperature-enthalpy diagram showing T_G, T_m, and ΔH_f. Adapted from J. Hoffman (1958).[145]

in Fig. 5.1a.[143–145] The rate of crystal growth, U, can be approximated by:[143]

$$U \propto \frac{Tw}{\eta}\left[1 - \exp\left(-\frac{\Delta G_v}{k_B T}\right)\right] \tag{5.1}$$

where T is temperature, w is a constant depending on the growth mode, and η is the molecular mobility. The Gibb's free energy difference, ΔG_v, is proportional to the enthalpy of fusion of the crystal phase, ΔH_f, as shown in Fig. 5.1b, and the degree of super cooling: $T_m - T$, where T_m is the crystal melting temperature:[145]

$$\Delta G_v \propto \frac{\Delta H_f (T_m - T) T}{T_m^2}. \tag{5.2}$$

Compounds with stable amorphous/semi-crystalline morphologies therefore have three characteristic traits: a high T_G indicating that molecules require a large amount of thermal energy to become mobile, a high T_m, and a low ΔH_f indicating that the energetic driving force between the amorphous and crystalline phases is small.

5.2 Morphological stability of exciton blocking layers

Perhaps the most widely reported morphological instabilities are found within wide energy gap OPV cathode buffer layers.[81,87,141,142] In 2007, H. Wu *et al.*[141] found that replacing BCP buffers with TPBi significantly improved the lifetime of CuPc/C_{60} OPVs. In 2010, N. Wang *et al.*[142] saw a similar improvement when comparing TPBi to BPhen and BCP buffers.

5.2.1 Differential scanning calorimetry and x-ray spectra

Here, we study the structural phases of BPhen, BP4mPy, and TPBi using a combination of DSC and temperature resolved XRD. First, DSC is used to identify the phase transition temperatures of each exciton blocking material. Each powder sample (0.1-2 mg) was hermetically sealed in an Al pan, and heat flow was measured in comparison to a calibrated reference pan as a function of temperature. Samples were measured during heating at 10°Cmin^{-1} from 25°C to slightly below each material's evaporation temperature to prevent decomposition, then measured during cooling, and a 2nd heating ramp. Since the powders typically begin as crystalline and become amorphous after cooling from the melt, this heat-cool-heat cycle allows us to see the transitions beginning with a crystal (1st heating) and glass (2nd heating). All DSC data are plotted with exothermic reactions in the positive direction. To obtain the temperature-dependent XRD spectra, organic powder samples were heated on a N_2-purged XRD stage, and then cooled back to room temperature. Diffraction spectra were taken from $2\theta = 5 - 30°$ at each temperature identified as a phase transition from DSC measurements. The background of the stage itself was measured before loading the organic powder to identify any features not associated with the sample.

During the 1st heating ramp, the BPhen powder showed only one transition: a melt at 218°C, as shown in Fig. 5.2a. After cooling from the melt, a large glass transition is observed beginning at 61°C, which is also clearly observed in the 2nd

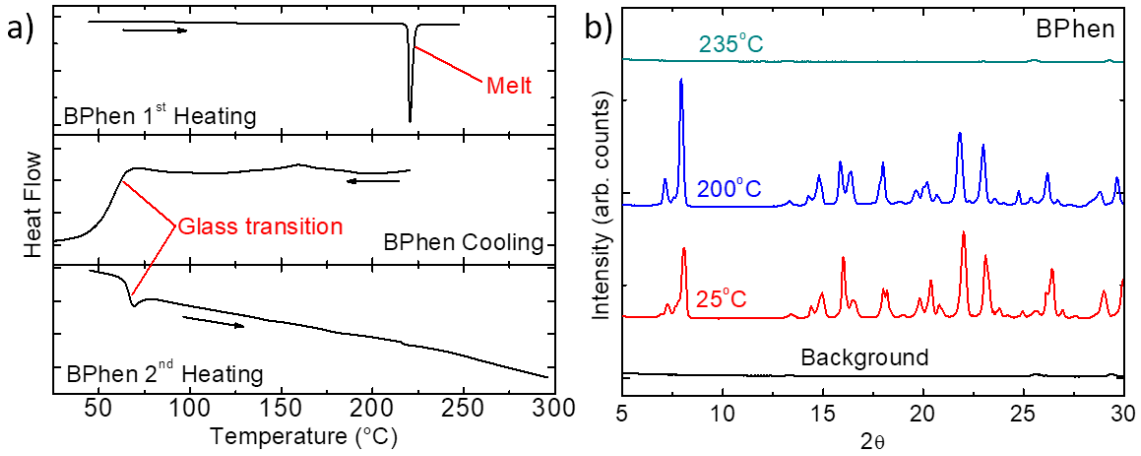

Figure 5.2: **BPhen DSC and powder XRD spectra** | **a)** Differential scanning calorimetry on a BPhen powder sample, with the melt and glass transitions indicated. **b)** Powder x-ray diffraction spectra of a BPhen powder at several temperatures: room temperature, 200°C = just before the melt, and 235°C = just after melting.

heating ramp as well. Melting and cooling produced a fully amorphous BPhen phase, since during the 2nd heating, only T_G is observed with no melt. From the XRD spectra in Fig. 5.2b, BPhen shows several crystal peaks at room temperature prior to heating. After heating to 200°C (just below the melting temperature), additional crystallization was observed, particularly at the 2θ = 7.8-8.2°, suggesting the BPhen morphology shifted during heating. At 235°C, the powder melts and no peaks are visible.

Comparatively, BP4mPy has a very different structure (shown in Fig. 5.3), as even the powder shows no evidence of crystallinity. During the 1st DSC heating cycle, the glass transition is visible at 105°C, and can also be seen during cooling and the 2nd heating ramp. Another feature visible at high temperatures in all three scans at 245°C corresponds to a weak crystallization event, such as a meta stable high enthalpy crystal. However, no x-ray features were observed at higher temperatures (not-shown), thus the origin of this feature is unknown. From the x-ray spectra, a very broad hump is visible at room temperature with no crystal features. The hump disappears at 225°C, suggesting that BP4mPy can flow like a liquid when heated past

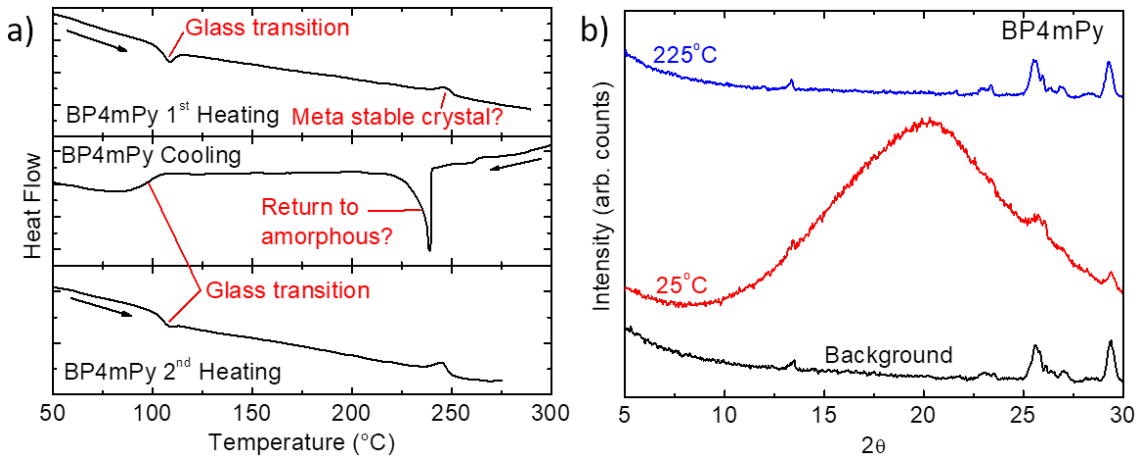

Figure 5.3: **BP4mPy DSC and powder XRD spectra | a)** Differential scanning calorimetry on a BP4mPy powder sample, with the glass transition indicated. The origin of the exothermic peak at 245°C in both heating cycles is unknown, but may correspond to a meta stable crystallization, in which case the endothermic peak during cooling is the meta stable crystal returning to the amorphous phase. **b)** Powder x-ray diffraction spectra of a B4mPy powder at room temperature and 225°C (approaching the exothermic DSC peak at 245°C).

its T_G. The lack of crystallinity in BP4mPy is consistent with its bulky non-planar structure, as was shown in Fig. 4.1.

During its 1st heating, no T_G is observed in TPBi, as shown in Fig. 5.4, suggesting that the powder is almost entirely crystalline. Slightly above 200°C, an exothermic peak is observed, suggesting that TPBi recrystallizes. Comparing the XRD spectrum at room temperature to the spectra just beyond this transition at 220°C, the crystal structure changes, indicating that this exothermic feature corresponds to a polymorphic transition. At 245°C, there is an endothermic transition that appears to be the polymorphic phase melting. The x-ray spectra taken just above this transition at 260°C has elements of both of the lower temperature spectra. At 274°C, TPBi melts, thus no features are visible in the XRD spectra at 280°C. After cooling, TPBi forms an amorphous phase, which has a glass transition at 120°C—visible in both the cooling and 2nd heating DSC ramps.

Recall from §5.1 that three parameters are indicative of morphologically stable

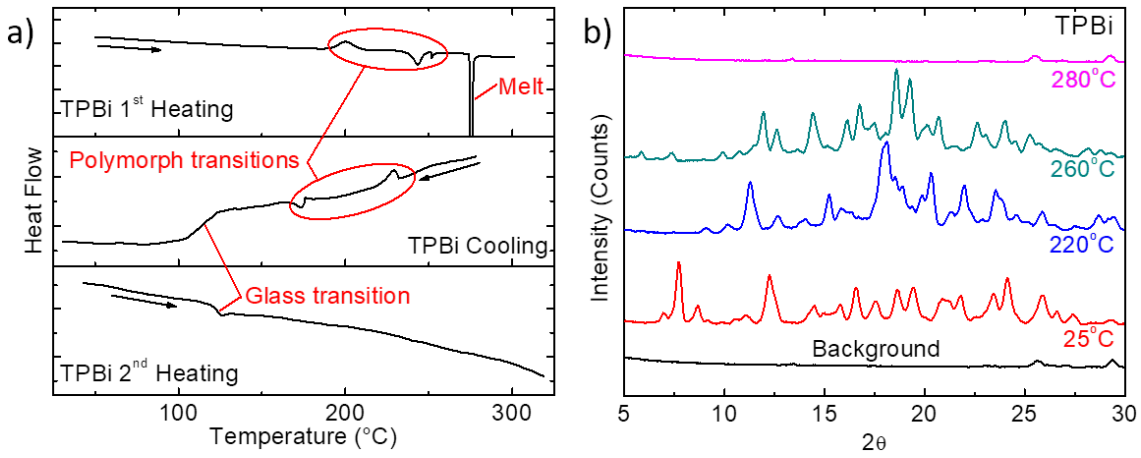

Figure 5.4: **TPBi DSC and powder XRD spectra** | **a)** Differential scanning calorimetry on a TPBi powder sample, with the glass transition and melt indicated. In addition to these features, polymorph crystallization and melting features are observed between 150 and 250°C. **b)** Powder x-ray diffraction spectra of a TPBi powder at several temperatures: room temperature, 220°C = just beyond the polymorph recrystallization feature, 220°C = just beyond the endothermic polymorph feature (possibly a melt), and 280°C = just after melting.

amorphous phases: high T_G, high T_m, and low ΔH_f. For the three exciton blocking compounds shown, the glass transitions are evident, as are the melting temperatures of BPhen and TPBi, reproduced in Table 5.1. To calculate ΔH_f, the DSC melting peaks were integrated over temperature and converted to kJ/mol using the molecular weights and masses of each sample. Using this method, the ΔH_f of BPhen was found to be significantly higher than that of TPBi (ΔH_f = 79.9 to 46.6 kJ/mol). This low T_G, T_m, and large ΔH_f all suggest that BPhen crystallizes, while TPBi and BP4mPy are significantly more stable. In addition to these three compounds, literature values of T_G for BCP and 3TPYMB are also shown in Table 5.1, along with the approximate sublimation/evaporation temperatures of BPhen, BP4mPy, TPBi, and 3TPYMB measured with a thermocouple at 10^{-6} Torr in a vacuum thermal evaporator at the onset of deposition.

Table 5.1: **Thermal properties of OPV cathode buffer compounds.**

	T_G (°C)	T_m (°C)	ΔH_f (kJ/mol)	$T_{evap/sub}$ (°C)
3TPYMB[81]	106	-	-	240
BCP[146]	89	-	-	-
BP4mPy[81]	105	-	-	350
BPhen[81]	61	218	79.9	230
TPBi[81]	120	274	46.6	320

5.3 Stability of DBP:C_{70} organic photovoltaics

In 2013, X. Xiao *et al.*[147] demonstrated a PMHJ OPV cell based on the DBP/C_{70} HJ with a neat BPhen buffer layer, which achieved a *PCE* of 6.4%. The lifetime of these cells was found to be poor due to crystallization of the BPhen layer—reaching T_{80} in less than 10 hr, and degrading by 50% within 125 hr.[87] To improve the efficiency of these devices, X. Xiao *et al.* (2014)[50] replaced the neat BPhen cathode buffer layer with BPhen:C_{60} EF-CBLs, which had been developed the previous year by A. Bartynski *et al.* (2013).[49] The EF-CBLs dramatically improved charge extraction efficiency, particularly at high intensities, leading to a *PCE* of 8.1% under simulated AM1.5G illumination. When we studied the lifetime of these devices using the setup described in §3.2, we found that blending C_{60} into the BPhen buffer also significantly improved the operational stability of the devices, as shown in Fig. 5.5. Compared to devices with neat BPhen buffers, the EF-CBL devices had T_{80}'s greater than 800 hr—especially considering that the J_{SC} degradation observed in Fig. 5.5 is primarily due to the spectral instability of the Xe aging lamp, as discussed in §3.2.

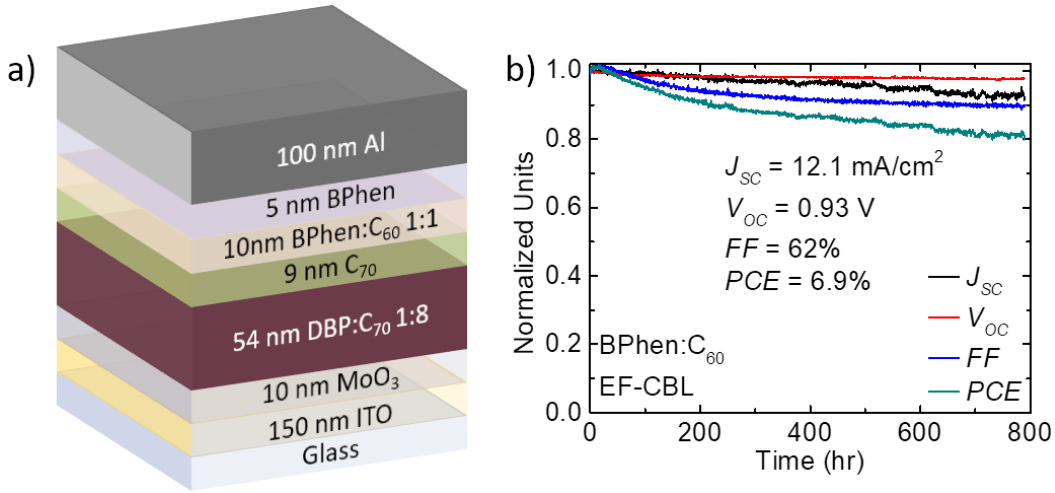

Figure 5.5: **Lifetime of DBP:C_{70} OPVs with BPhen:C_{60} EF-CBLs** | **a)** Device structure of a PMHJ DBP:C_{70} OPV with a BPhen:C_{60} EF-CBL. **b)** Evolution of the normalized photovoltaic characteristics: J_{SC}, V_{OC}, FF, and PCE as a function of time under 100 mW/cm^2 simulated AM1.5G illumination for the OPV shown in **a**. The observed loss in J_{SC} is primarily associated with the spectral instability of the Xe aging source rather than degradation of the OPV itself. Lifetime data from Q. Burlingame *et al.* (2016).[81]

5.3.1 Electron-filtering compound buffer layers

To further improve the lifetime of PMHJ DBP:C_{70} OPVs with EF-CBLs, we replaced the morphologically unstable BPhen layers with the alternative exciton blocking materials discussed in §5.2, as shown in Fig. 5.6. The C_{60} in the EF-CBL of one device was also replaced with C_{70} to avoid any possible long-term effects of C_{60} oligomerization (discussed in Chapter IV). Compared with the BPhen:C_{60} EF-CBL devices, the FF's and V_{OC}'s of the stabilized devices were significantly more robust, following the lifetime trend: TPBi:C_{70}>BP4mPy:C_{60}≈TPBi:C_{60}>3TPYMB:C_{60}. The PCEs of all of the devices were lower than the original BPhen:C_{60} EF-CBL OPV (PCE = 6.9%) as shown in each panel of Fig. 5.6, but only the BP4mPy:C_{60} device was significantly lower (PCE = 6.1%). The devices demonstrated here are less efficient than those originally published by X. Xiao *et al.* (2014),[50] due to their larger areas (0.11 cm^2 compared with 0.008 cm^2), and their cathodes, which are Al instead of Ag for

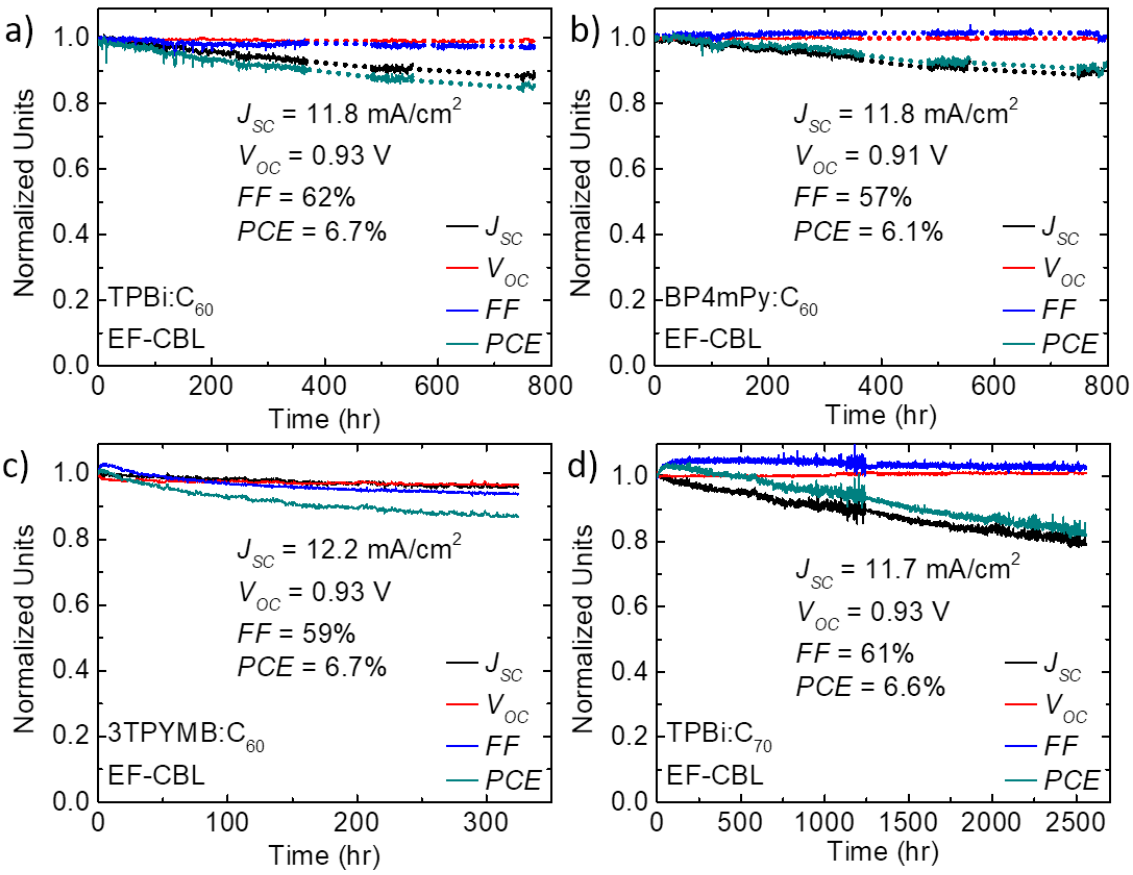

Figure 5.6: **Lifetime of DBP:C$_{70}$ OPVs with various EF-CBLs** | Evolution of the normalized photovoltaic characteristics: J_{SC}, V_{OC}, *FF*, and *PCE* as a function of time under 100 mW/cm^2 simulated AM1.5G illumination for OPV with the EF-CBL structure indicated in the bottom corner of each graph: **a)** TPBi:C$_{60}$; **b)** BP4mPy:C$_{60}$; **c)** 3TPYMB:C$_{60}$; and **d)** TPBi:C$_{70}$. The fresh photovoltaic performance parameters are shown in each panel. The observed loss in J_{SC} is primarily associated with the spectral instability of the Xe aging source rather than degradation of the OPV itself. Adapted from Q. Burlingame *et al.* (2016).[81]

increased stability and device yield. The primary difference between the performance of the BPhen:C$_{60}$ EF-CBL devices and the stabilized devices shown here is their lower *FF*, due to reduced conductivity and charge extraction efficiency.

The stability of these devices is consistent with the theoretical morphological stability of the exciton blocking layers themselves, with TPBi and BP4mPy devices having better stability than 3TPYMB:C$_{60}$ OPVs, which are more stable than BPhen:C$_{60}$ EF-CBL OPVs. However, as noted previously, the reliability of OPVs

with blended EF-CBLs is significantly higher than those with neat BPhen buffers due to the presence of the fullerene that pins the morphology of the other exciton blocking component. To assess the morphological stability of the exciton blocking materials when blended with fullerene, x-ray diffraction spectra were collected on 200 nm 1:1 blended films before and after aging for 1 week under simulated AM1.5G illumination, as shown in Fig. 5.7. As expected, the EF-CBLs with TPBi:C_{60}, TPBi:C_{70}, and BP4mPy:C_{60} show no evidence of crystallization or morphological change, except for perhaps BP4mPy:C_{60} which shows a change in the slope of the background. After aging, the background intensity at $2\theta < 10^\circ$ of the 3TPYMB:C_{60} film (Fig. 5.7a) was reduced, revealing a broad feature between $2\theta = 9$ and 12°. The least stable of the films was BPhen:C_{60}, which showed a diffraction peak at $2\theta = 13.7^\circ$ after aging, consistent with its relatively poor lifetime.

The most stable of all the devices studied (TPBi:C_{70}) saw its *FF* and V_{OC} improve slightly over its measured lifetime. However, its J_{SC} does appear to degrade by 20% over the 2500 hr measurement due to the spectral instability of the Xe arc lamp, as discussed previously. To determine the magnitude of the J_{SC} loss, a fresh TPBi:C_{70} device was aged for more than 1 year under continuous illumination, and its *EQE* was measured periodically, as shown in Fig. 5.8. After aging for 5000 hr, no discernible degradation in J_{SC} was observed—and *FF* and V_{OC} remained unchanged, consistent with the data in Fig. 5.6d. However, between 5000 and 7300 hr a 3% J_{SC} loss was observed, with an additional 2% J_{SC} loss and 3% relative *FF* loss between 7300 and 9000 hr leading to a total of 8% relative *PCE* loss after 9000 hr. The delayed onset of degradation observed after 5000 hr suggests that the loss may be due to extrinsic factors, such as permeation of O_2 or H_2O through the epoxy seal.[148] To convert the lifetimes from these continuous aging experiments to outdoor lifetime projections, we assume an average of 5 kWhr/m^2 of sunlight per day (equivalent to 5 hr of equivalent AM1.5G radiation as discussed in §1.1.12). The data at 9000 hr

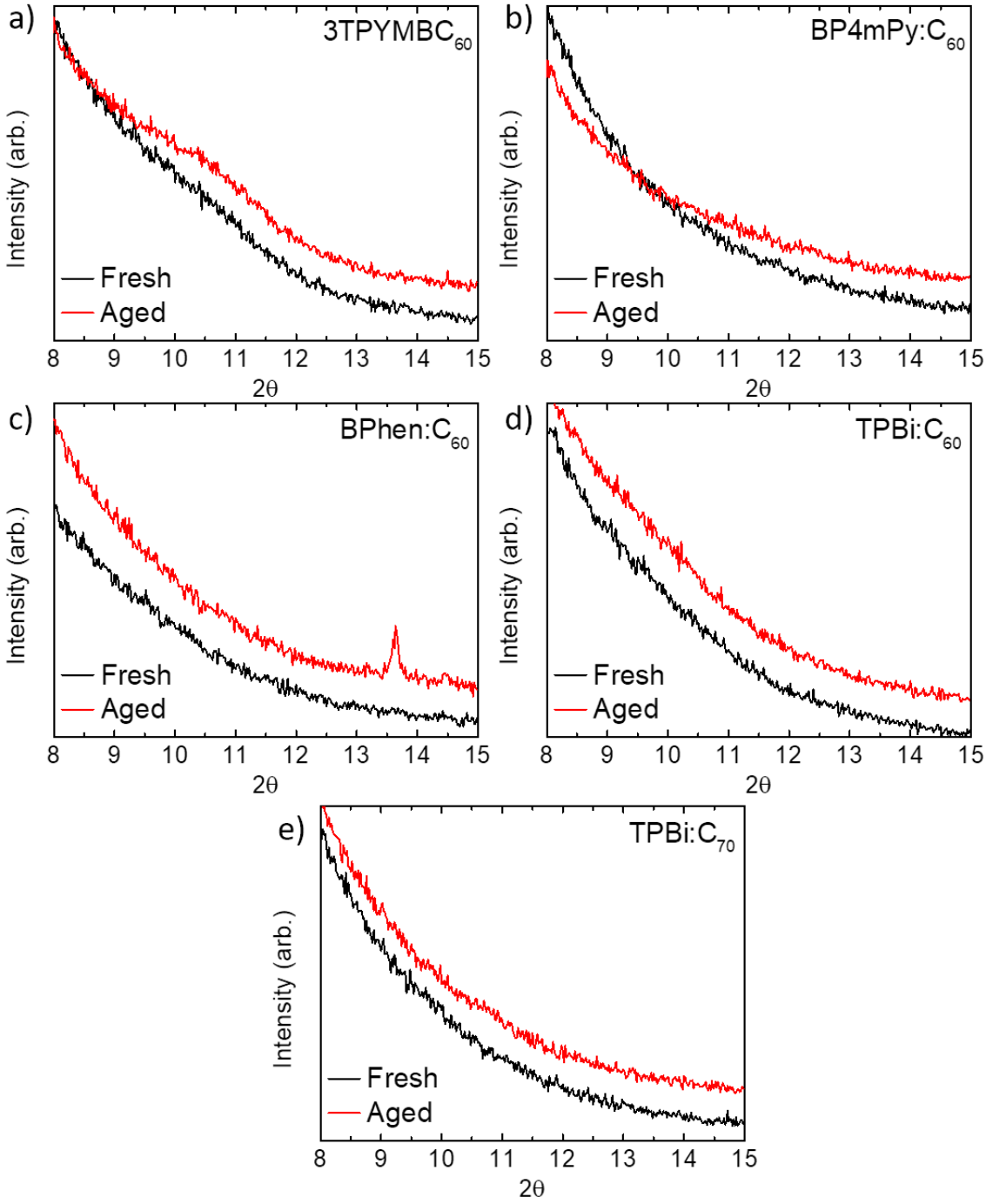

Figure 5.7: **XRD spectra of 200 nm thick blended organic films** | Powder x-ray spectra from 200 nm thick blended films of **a)** 3TPYMB:C_{60}; **b)** BP4mPy:C_{60}; **c)** BPhen:C_{60}; **d)** TPBi:C_{60}; and **e)** TPBi:C_{70} before and after aging for 1 week under 100 mW/cm^2 simulated AM1.5G illumination in N_2. The spectra were offset from each other along the y-axis for clarity. Partially adapted from Q. Burlingame *et al.* (2016);[81] the BP4mPy:C_{60} and TPBi:C_{60} data were not published previously.

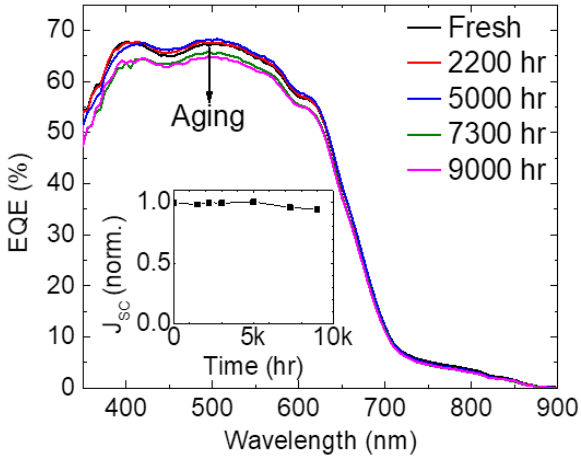

Figure 5.8: **Lifetime of DBP:C_{70} OPVs with TPBi:C_{70} EF-CBLs** | EQE spectra of a DBP:C_{70} PMHJ OPV with a TPBi:C_{70} EF-CBL before and during aging under 100 mW/cm^2 of simulated AM1.5G illumination for 9000 hr. Inset: J_{SC} calculated by integrating the *EQE* spectra over AM1.5G vs. time.

are therefore equivalent to 4.9 years outdoors. If package failure is indeed responsible for the loss observed after 5000 hr, then the intrinsic lifetime of the cells is very long, since the slope of performance loss prior to 5000 hr was nearly 0.

5.3.2 High temperature accelerated aging

As we have seen in §5.3.1, the morphological stability of the EF-CBL is predictive of the the overall stability of the OPVs. Additionally, no intrinsic degradation was observed in OPVs with TPBi:C_{70} EF-CBLs over 5000 hr, suggesting that their morphology was totally stable under the conditions measured. To accelerate aging, and to understand how morphological changes degrade *PCE*, populations of the most and least stable OPVs (TPBi:C_{70} and BPhen:C_{60}) were aged at elevated temperatures under simulated AM1.5G illumination using the setup described in §3.2 and §3.3. Due to the relatively low T_G of BPhen (61°C), BPhen:C_{60} devices were aged at 50, 60, 70, and 80°C while TPBi:C_{70} OPVs were aged at 55, 80, 105, and 130°C (the maximum temperature the aging apparatus could sustain). The elevated temperatures produced no systematic changes in J_{SC} or V_{OC}, thus only the *FF*'s of the

two populations of devices are shown in Fig. 5.9. The *FF* of devices with BPhen:C_{60} show a clear trend with increasing temperature, which can be fit by a biexponential function of the form:

$$FF(t) = \alpha_1 \exp(-k_{fast}t) + \alpha_2 \exp(-k_{slow}t) + \beta \tag{5.3}$$

where α_1, α_2, and β are constants, and k_{fast} and k_{slow} are degradation rates that follow the Arrhenius temperature relationship in Eq. 3.5. Remarkably, the OPVs with TPBi:C_{70} EF-CBLs show no trend with aging temperature other than a rapid annealing that occurs during the first 100 hr under test. Thus, even when operating well above its measured T_G, the low crystallization driving force (ΔG_v) of TPBi results in a stable morphology.

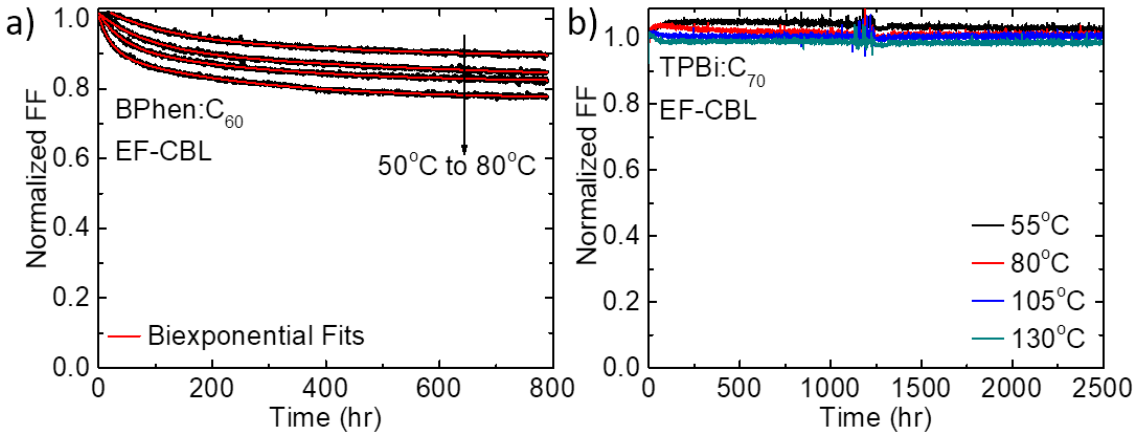

Figure 5.9: **Thermally accelerated aging of OPVs** | Normalized *FF* vs. time for a population of PMHJ DBP:C_{70} OPVs with **a)** BPhen:C_{60} EF-CBLs and **b)** TPBi:C_{70} EF-CBLs. Biexponential fits to the BPhen:C_{60} data are shown in **a**. Data from Q. Burlingame *et al.* (2016).[81]

5.3.3 Activation energies of thermally-induced degradation

Rearranging Eq. 3.5, the activation energy of the degradation rates, k_{fast} and k_{slow} in this case, are equivalent to the slope:

$$E_A = -\frac{\partial \ln\left(k_{deg}\right)}{\partial\left(\frac{1}{k_B T}\right)}. \tag{5.4}$$

The temperature-dependent degradation rates are therefore plotted in Fig. 5.10, and fit with Eq. 5.4. Interestingly, despite k_{fast} being significantly larger than k_{slow}, their activation energies are almost identical: 0.56±0.06 eV and 0.53±0.13 eV, respectively. This suggests that BPhen crystallization is degrading the *FF* in two decoupled ways.

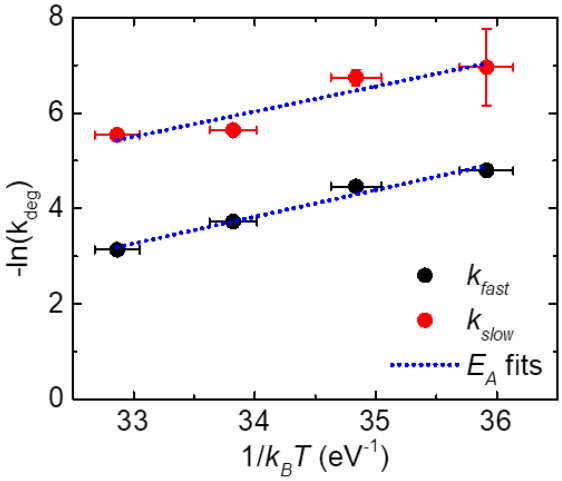

Figure 5.10: **Arrhenius plot of BPhen:C_{60} OPV degradation rates** | Logarithm of *FF* degradation rates extracted from the biexponential fits shown in Fig. 5.9 vs. inverse thermal energy at the aging temperature for BPhen:C_{60} EF-CBL devices. Adapted from Q. Burlingame *et al.* (2016).[81]

5.3.4 Dark current analysis

To understand the origin of *FF* degradation, device dark currents were measured after aging under illumination at elevated temperatures for 800 and 2500 hr

for BPhen:C_{60} and TPBi:C_{70} EF-CBL devices, respectively, as shown in Fig. 5.11. The magnitude of the dark current at < 0.8 V was considerably larger after aging in BPhen:C_{60} EF-CBL OPVs, and as a function of aging temperature, while the dark current of the TPBi:C_{70} OPVs aged at 130°C was almost identical to the as-grown J–V characteristics. Previously, we showed that BPhen crystallization could penetrate into the active layer of OPVs, carrying metal from the cathode.[87] This process is also likely responsible for the significant temperature-dependent decrease in shunt resistance, R_{SH}, with time—evident from the dark current increase in OPVs with BPhen:C_{60} EF-CBL layers.

In quadrant IV of the J–V characteristics, the increase in dark current counteracts the photocurrent, shifting the curve toward the origin, thus reducing FF and PCE. Interestingly, the increase in the dark current magnitude is not symmetric about $V = 0$ as would be expected if it were only due to a decreasing R_{SH}. The J–V characteristics in this region also depend strongly on charge recombination[149] which can be quantified by the diode ideality factor, m, from Eq. 1.27. To disentangle the factors degrading FF, we split the dark current contribution to the J–V char-

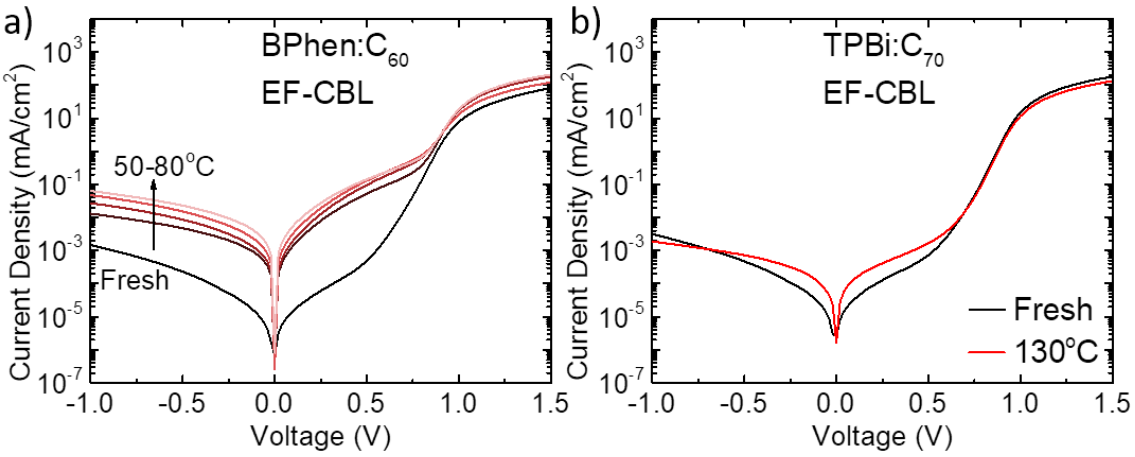

Figure 5.11: **Dark currents of OPVs aged at high temperature** | Dark current density vs. voltage for OPVs with **a)** BPhen:C_{60} EF-CBLs and **b)** TPBi:C_{70} EF-CBLs before and after aging under simulated 1-sun illumination at the elevated temperatures noted for 800 and 2500 hr respectively. Adapted from Q. Burlingame *et al.* (2016).[81]

acteristics into two components: J_{SH}, which is symmetric about $V = 0$; and J_{REC}, which is non-linear with voltage, presumably due to charge recombination. The first component, J_{SH}, is extracted from the illuminated J–V characteristics during aging by extrapolating the current near 0V in weak reverse bias. The non-symmetric component, J_{REC}, is taken to be the difference between the total current and J_{SH} at the MPP voltage (V_p). Plotting these currents at V_p and normalizing them to J_{SC}, as shown in Fig. 5.12, allows us to directly see the impact on FF—*e.g.*, a 1% increase in J_{SH}/J_{SC} or J_{REC}/J_{REC} corresponds to a 1% loss in FF. Furthermore, we find that J_{SH}/J_{SC} and J_{REC}/J_{SC} can be well fit at all temperatures with exponential or biexponential functions using the rates k_{fast} and k_{slow} extracted from the fits in Fig. 5.9, as shown in Fig. 5.12. This confirms that thermally activated crystallization of BPhen drives both a temperature-dependent shunting of the OPVs with aging and an increased charge recombination, which degrades FF at different rates. These two

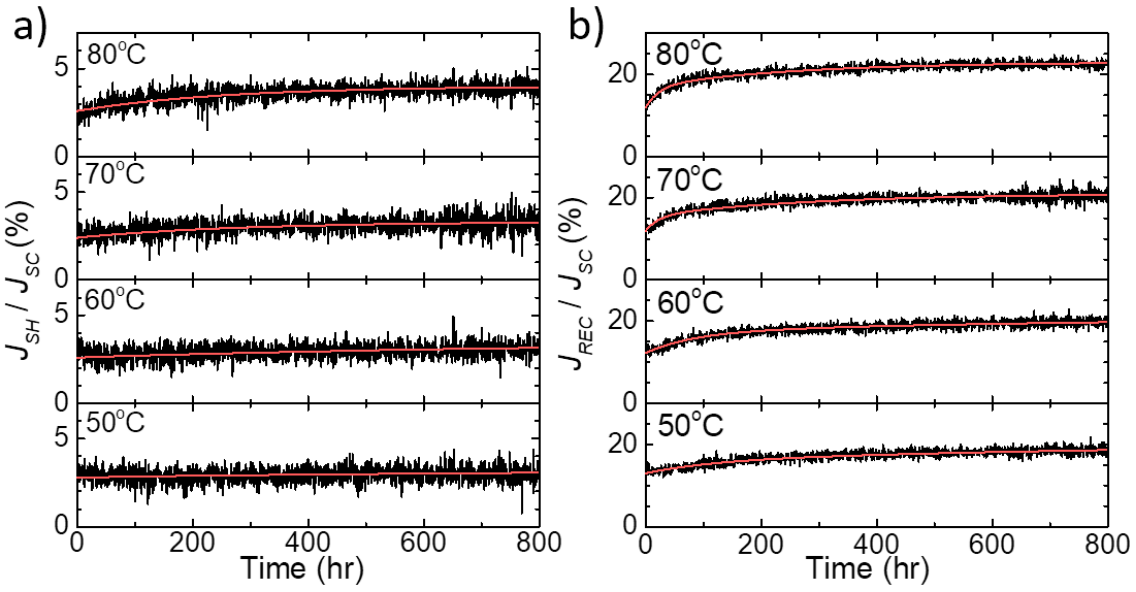

Figure 5.12: **Shunt and recombination currents during OPV aging | a)** J_{SH}/J_{SC} and **b)** J_{REC}/J_{SC} extracted from the J–V characteristics under illumination for OPVs with BPhen:C_{60} EF-CBLs aged at the temperatures indicated. The data are fit (lines) with biexponential functions using the rates k_{fast} and k_{slow} extracted from fits to FF vs. time in Fig. 5.9. Adapted from Q. Burlingame *et al.* (2016).[81]

processes account for a majority of the FF degradation observed in Fig. 5.9, with an additional 5% to 9% (depending on aging temperature) FF loss coming from a reduction in V_p during aging.

As can be seen from Fig. 5.12, the FF loss due to J_{REC} is generally greater than the loss due to shunting of the diode. It is therefore expected that the ideality factor of the diodes, m, should change significantly as a function of aging. To determine m experimentally, Voc can be plotted vs. the logarithm of J_{SC} as a function of intensity, as shown in Fig. 5.13. The slope of the curves using this method is proportional to m, as follows:

$$\frac{\partial V_{OC}}{\partial \ln(J_{SC})} \propto \frac{mk_BT}{q}, \tag{5.5}$$

The slope (and, therefore, m) of aged devices with BPhen:C_{60} EF-CBLs increases dramatically over time, consistent with the observed increase in J_{REC} and loss in FF. The devices with TPBi:C_{70} EF-CBLs show almost no change despite aging at significantly higher temperatures. In both populations of fresh devices, $m = 2.06$

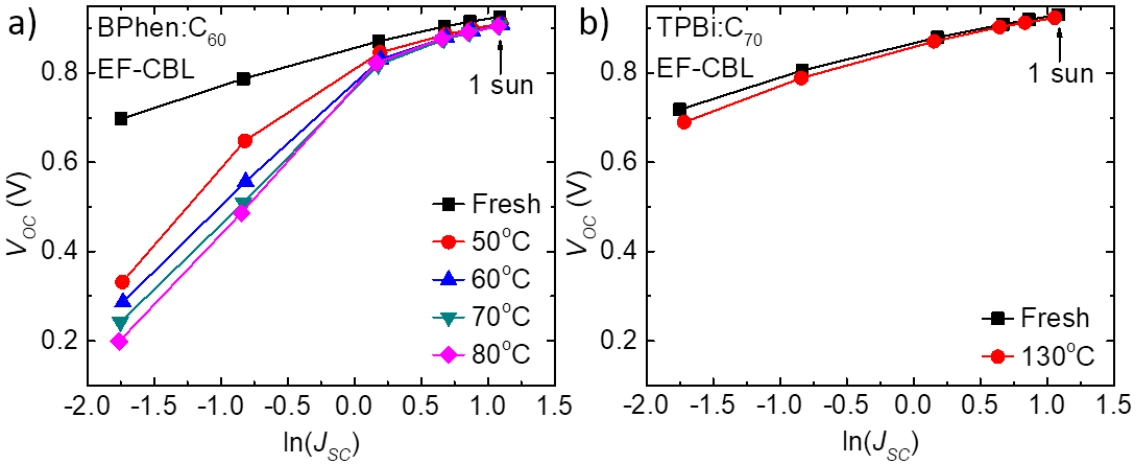

Figure 5.13: **Diode ideality factor extraction in aged OPVs** | Intensity-dependent V_{OC} vs. $\ln(J_{SC})$ from 0.1 mW/cm^2 to 100 mW/cm^2 incident simulated solar illumination for **a)** BPhen:C_{60} EF-CBL OPVs before and after aging for 800 hr and **b)** TPBi:C_{70} EF-CBL OPVs before and after aging for 2500 hr at the stated temperatures under 100 mW/cm^2 simulated AM1.5G illumination.

under 1 sun. After aging, m actually slightly decreased in TPBi:C_{70} EF-CBL OPVs, while increasing to $m = 2.33 - 2.61$ in BPhen:C_{60} OPVs depending on the aging temperature.

5.3.5 Outdoor aging measurements

The time-dependent performance characteristics of a population of four PMHJ DBP:C_{70} OPVs with TPBi:C_{70} EF-CBLs placed outdoors in Sede Boqer, Israel (30°51' N, 34°46' E) are shown in Fig. 5.14. The devices were mounted on a fixed-angle (30°,

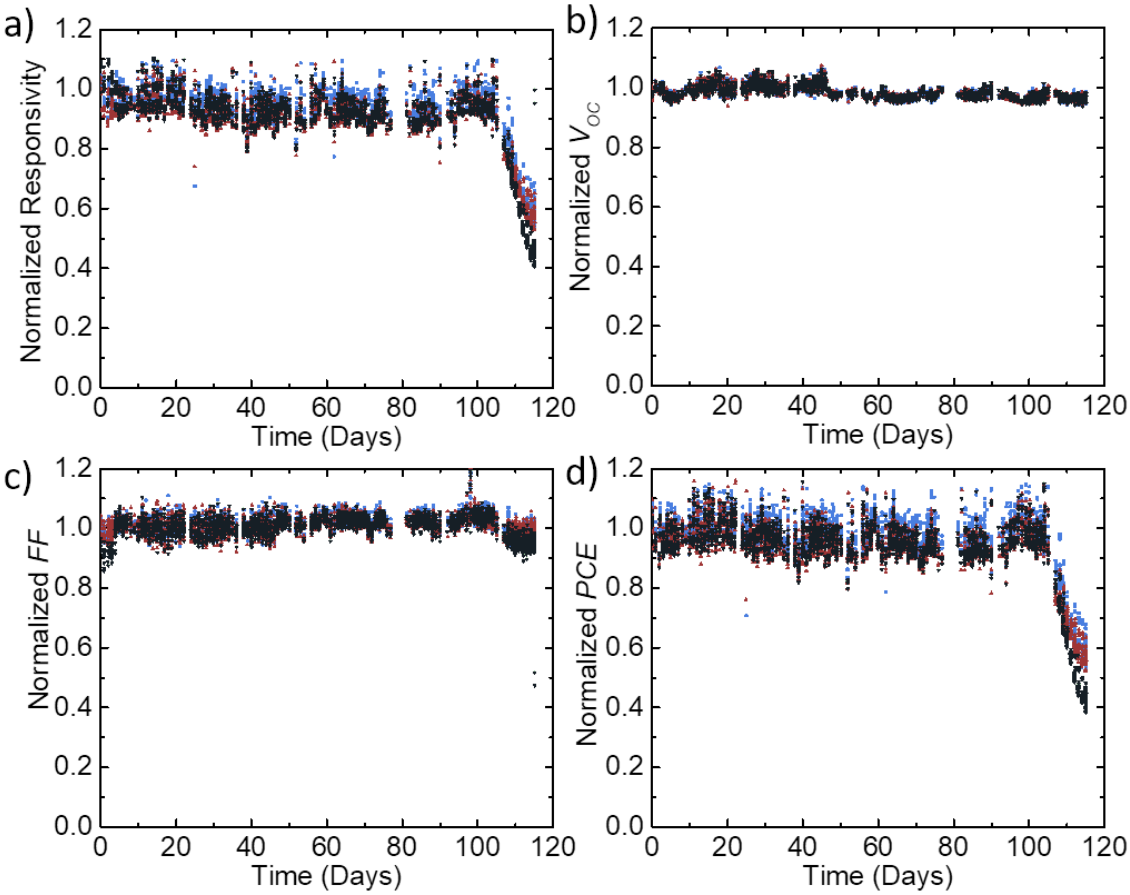

Figure 5.14: **Outdoor lifetime measurements of OPVs** | Normalized photovoltaic operational parameters: **a)** responsivity = J_{SC}/P_{in}; **b)** V_{OC}; **c)** *FF*; and **d)** *PCE* vs. time for four PMHJ DBP:C_{70} OPVs with TPBi:C_{70} EF-CBLs aged outdoors for 120 hr. The catastrophic failure observed after 100 days is due to failure of the encapsulation materials, and the resultant photooxidation of the organic materials.

as described in §3.2) from November 8th, 2015 to February 21st, 2016 (120 days), and their J–V characteristics were measured twice per hour during times when the solar irradiance exceeded 30 mW/cm^2. Cell temperatures and solar irradiance were monitored with a thermistor and calibrated Si photodiode, respectively, during the measurement. Prior to catastrophic failure at day 106, no intrinsic degradation was observed in their performance—consistent with their high stability under continuous illumination. The catastrophic failure was a result of package failure and primarily affected J_{SC} (responsivity = J_{SC}/P_{in}). Recall from §4.1, the photoactive materials (DBP and C_{70}) are both susceptible to photooxidation, as is TPBi, thus the organics likely photobleached rapidly when exposed to atmosphere.

5.3.6 Unencapsulated cells with BP4mPy:C_{60} buffers

While extrinsic OPV stability is generally outside of the scope of this thesis, recall from §4.1 that BP4mPy is an outlier among the materials studied in this work, as it showed no change in FTIR spectra even aging under 1-sun simulated illumination in atmosphere. As a result of BP4mPy's inert nature, it may be a promising thin film encapsulation material and may provide added resilience to atmospheric H_2O and O_2 that may permeate encapsulation materials during aging. A test of this concept is shown in Fig. 5.15, where OPVs with the BP4mPy:C_{60} EF-CBLs were aged for one month under 1-sun illumination in air with no encapsulation. After this test, the devices retained 73% of their starting efficiency, which is better than or comparable to the *dark* shelf life of many unencapsulated polymer OPVs.[104,150] The devices were also significantly more stable than the OPVs with TPBi:C_{70} EF-CBLs aged outdoors that lost more than 50% of their *PCE* within 10 days of package failure.

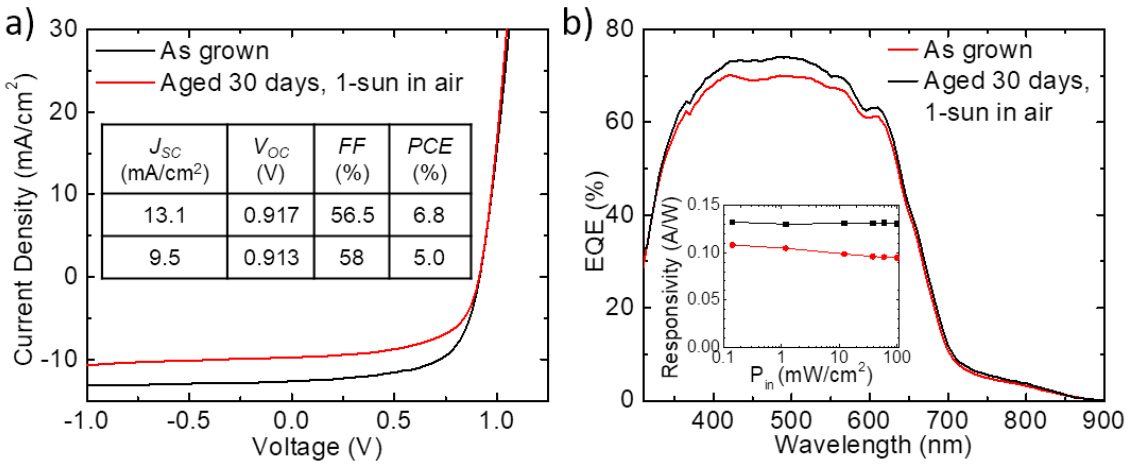

Figure 5.15: **Unencapsulated OPV stability with BP4mPy:C_{60} buffer layers** | **a)** J–V characteristics of a PMHJ DBP:C_{70} OPV with a BP4mPy:C_{60} EF-CBL before and after aging for 30 days under simulated 1-sun illumination with no encapsulation. inset: Table of photovoltaic performance metrics for the fresh (top row) and aged (bottom row) device. **b)** Wavelength-dependent EQE at the same conditions. After aging, the device had an intensity-dependent roll-off in EQE, as shown by the inset: responsivity = J_{SC}/P_{in} vs. P_{in}. The EQE spectra is taken at low intensity, and the photovoltaic performance metrics are reported under P_{in} =100 mW/cm^2.

5.3.7 Design rules for morphological stability

In addition to demonstrating the most stable OPVs reported to date (PMHJ DBP:C_{70} OPVs with TPBi:C_{70} EF-CBLs, this section suggests two general principles that can be applied to an OPV materials system to enhance its morphological stability. Blending organic materials can result in a morphology that is more stable than the separate constituents, consistent with previous reports on OLEDs.[151,152] The presence of the fullerene in BPhen:C_{60} EF-CBLs, for example, disrupts the π-stacking of BPhen molecules and limits their aggregation, which can rapidly degrade OPVs.[87] Nevertheless, degradation is still observed in these devices as a result of thermally activated BPhen morphological rearrangement, showing that blending alone is insufficient to ensure stability. To produce truly stable amorphous phases, T_G and T_m should be maximized, while ΔG_v is minimized for each of the constituents. These

properties can be measured outside of devices using thermal and structural characterization techniques, but can still be predictive of OPV stability as this work has shown.

Among OPVs with morphologically unstable EF-CBLs, we find that *FF* is the quantity that is most sensitive to degradation. Crystallization of the EF-CBL produced low resistance shunt pathways through the diodes, and caused a significant increase in charge recombination. These degradation mechanisms were each thermally activated with activation energies within error of each other, $E_A = 0.56 \pm 0.06$ eV and 0.53 ± 0.13 eV, confirming that they are caused by the same failure process. Due to their thermal stability, elevated temperature was not found to be an effective accelerated aging stressor for OPVs with TPBiC_{70} EF-CBLs, as no long-term change in degradation rate was produced despite operating at up to 130°C for 2500 hr. However, this makes DBP:C_{70} OPVs with TPBi:C_{70} EF-CBLs excellent model systems for the study of OPV performance under extreme conditions such as high temperatures and light intensities, which will be shown in Chapters VI and VII. The results are promising for the future of OPV technology as they indicate that OPVs with commercially viable lifetimes are possible with the appropriate selection of materials and device architectures.

CHAPTER VI

Outdoor operation of organic photovoltaic cells

The efficiency of an OPV varies as a function of temperature and intensity due to the complex dependencies of bimolecular recombination, exciton dissociation, polaron mobility, resistive power loss, electron–phonon coupling, and absorption on these variables.[129,130,149,153–157] These dependencies have direct practical ramifications for the operation of OPVs outdoors, as cell temperatures and the intensity, angle, and spectrum of the incident sunlight vary dynamically throughout the day. Understanding the diurnal performance of OPVs (*i.e.*, how their performance changes throughout the day) is therefore essential to evaluate their potential efficacy as a practical source of electrical power. Such studies are common for inorganic photovoltaics[158,159] as they have already been widely commercially deployed, while few studies exist for polymer OPVs[118,153] and this work contains the only known report of the diurnal behavior of small molecule OPVs.[130] The OPVs described in Chapter V of this work are uniquely suited to such studies due to their remarkable tolerance to high temperature,[81] which allows them to be studied across a broad range of intensities and temperatures without irreversibly degrading.

6.1 Diurnal performance characterization

To measure their diurnal performance, OPVs were placed oudoors in Sede Boqer, Israel on a fixed angle platform. At the beginning of each each hour, the J–V characteristics of the cells were measured five times and averaged to account for fluctuations in solar irradiance. The temperature of the cell was measured with a surface-mounted thermocouple and the incident solar intensity was measured with a calibrated Si photodiode as described in §3.2. Diurnal performance data from a clear sky day (November 8, 2015) are shown in Fig. 6.1. As expected, the solar irradiance follows a cosine dependence as the angle of the sun progresses throughout the day. The temperature of the cell increased until 1:00 pm, reaching a peak of 38°C. The photovoltaic efficiency parameters of the OPV, shown in Fig. 6.1b-c, were rela-

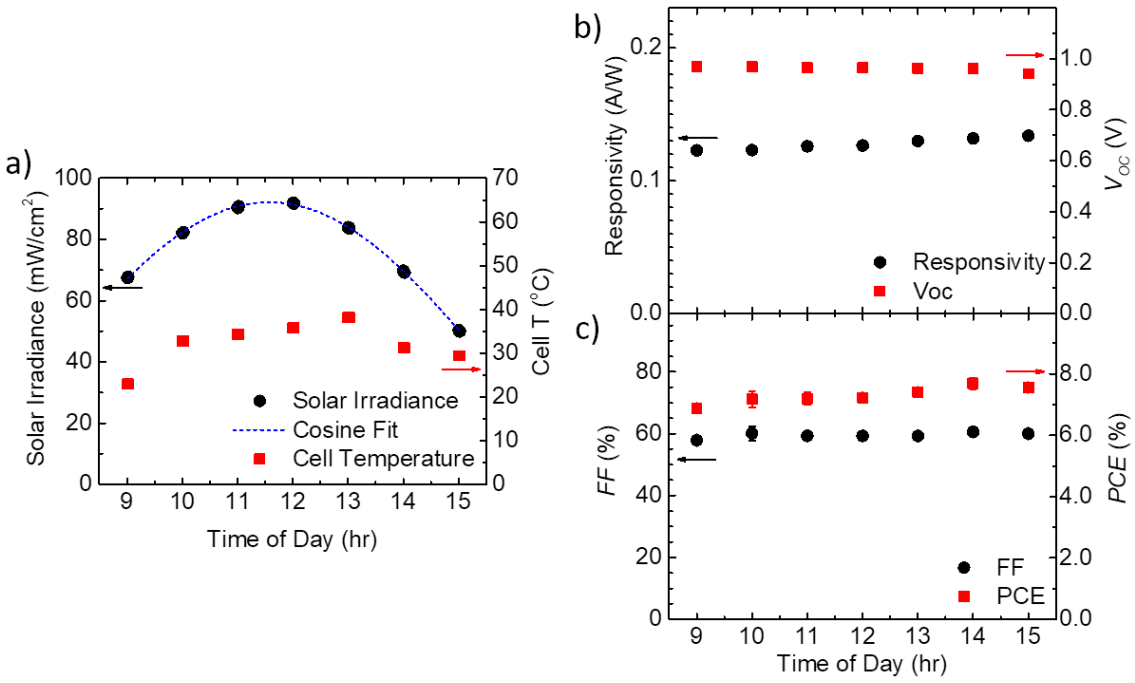

Figure 6.1: **Diurnal OPV performance** | **a)** Solar irradiance (left axis), OPV surface temperature (right axis); **b)** responsivity = J_{SC}/P_{in} (left axis), V_{OC} (right axis); **c)** FF (left axis), and PCE (right axis) measured outdoors on a PMHJ DBP:C_{70} OPV cell with a TPBi:C_{70} EF-CBL from 9:00 am to 3:00 pm on November 8, 2015 in Sede Boqer Israel. From Q. Burlingame *et al.* (2017).[130]

tively stable throughout the day with responsivity and, thus, *PCE* increasing slightly throughout the day. In the morning, the *PCE* of the OPV was $6.8 \pm 0.3\%$, increasing to a maximum of $7.7 \pm 0.3\%$ at 2:00 pm.

6.1.1 Intensity dependent performance

Intensity dependent performance of the OPVs was measured from 0.2-27 suns indoors using the solar concentrating scheme described in §3.2, with the results shown in Fig. 6.2. The *J*–*V* characteristics show a linear increase in J_{SC} with intensity up to $\sim$ 20 suns, before rolling off. The V_{OC} increases logarithmically, as shown by the fit

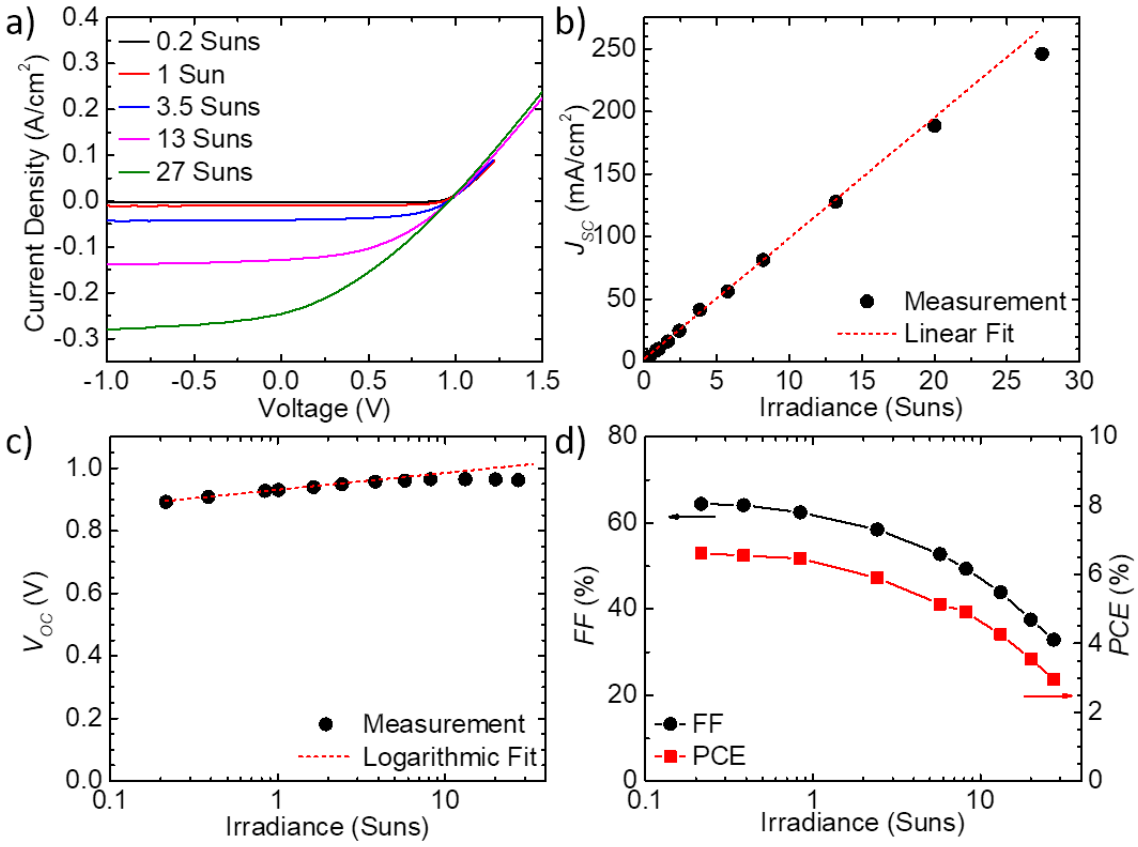

Figure 6.2: **Intensity-dependent OPV performance** | **a)** Select intensity-dependent *J*–*V* characteristics for a DBP:C_{70} PMHJ OPV under concentrated solar illumination. **b)** J_{SC}; **c)** V_{OC}; **d)** *FF* (left axis); and *PCE* (right axis) of the same cell as a function of incident irradiance. Adapted from Q. Burlingame *et al.* (2017).[130]

line in Fig. 6.2c, before rolling off at high intensities, while FF continuously decreases as intensity increases—dominating the trend in PCE. As intensity increases, FF is the first parameter to decrease due to resistive power losses that follow $P_{loss} = I^2R$. Considering the equivalent circuit for an OPV as was shown in Fig. 1.14, the voltage drop over R_S resulting from the photocurrent effectively forward biases the diode, which becomes significant at high intensities.[160] If we assume $R_S = 1\Omega$ (typical of these devices), the photocurrent generated by the 0.11 cm^2 OPV at 27 suns is nearly 30 mA, which creates a voltage drop of 30 mV over R_S. As a result, the exponential turn-on of the diode J–V appears to shift to the left in Fig. 6.2a. In addition, bimolecular recombination scales as the square of intensity,[161] which eventually causes the roll-off observed in J_{SC} at high intensities. Finally, the deviation in V_{OC} from its logarithmic trend at high intensities may be a result of increased charge recombination, although it is more likely due to heating during the high intensity measurements.

6.1.2 Temperature dependent performance

To measure their temperature dependence, OPVs were mounted on an automatic two-axis solar tracking panel outdoors. A copper heat spreader and thermoelectric heater/cooler were affixed to the back of the OPV, and its temperature was measured at the surface. The J–V characteristics of the cell were measured at 1-2°C intervals from 15-140° near solar noon, when the incident irradiance and spectrum were near to AM1.5G. Several representative quadrant IV J–V characteristics are plotted in Fig. 6.3a, and the photovoltaic performance parameters were extracted at all temperatures and plotted in Figs. 6.3b-d. The photocurrent generated by the OPV increased linearly, while V_{OC} linearly decreased. Fill factor increases with temperature up to $\sim$ 50°c, before remaining flat until $\sim$ 100°, and then decreasing at higher temperatures. At $T < 40$°C, the temperature-induced increases in J_{SC} and FF outweigh the loss in V_{OC}, producing a slight positive slope of 0.02%/°C. As the slope of FF(t) flattens

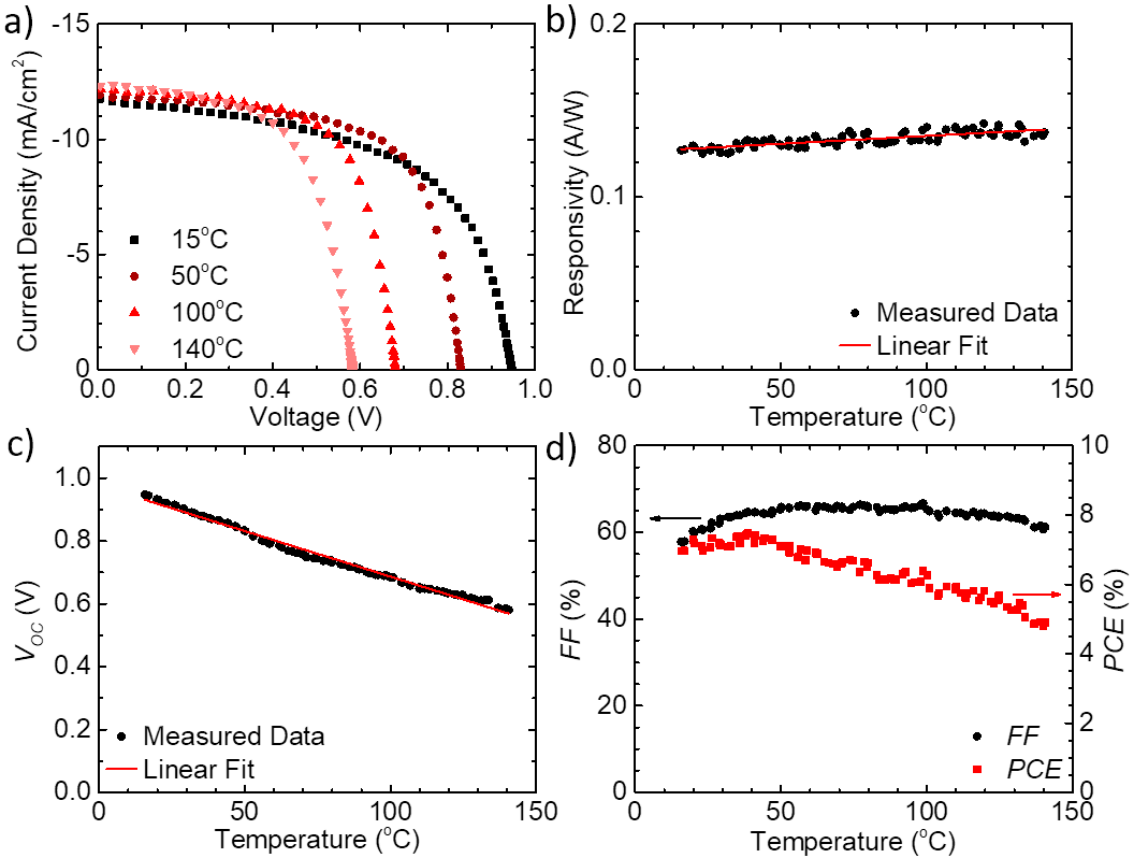

Figure 6.3: **Temperature dependent OPV performance** | **a)** Temperature dependent J–V characteristics for a DBP:C_{70} PMHJ OPV at the stated temperatures. **b)** Responsivity=J_{SC}/P_{in}; **c)** V_{OC}; **d)** FF (left axis); and PCE (right axis) of the same cell as a function of temperature. Adapted from Q. Burlingame *et al.* (2017).[130]

out, temperature-induced V_{OC} loss dominates PCE above 40° causing it to decrease linearly at higher temperatures.

The measured linear decrease in V_{OC} is consistent with theoretical expectations from Eq. 1.33. The temperature-dependence of FF is primarily determined by the resistance of the organic layers, which decreases with temperature as shown in §1.1.4. By fitting the linear region of the forward bias J–V characteristics, we find that R_S decreases from $1.05 \pm 0.04\ \Omega$ at $T = 15$°C to $0.73 \pm 0.03\ \Omega$ at $T = 50$°C. However, beyond $T = 50$°C the change in R_S is small ($R_S = 0.71 \pm 0.03\ \Omega$ at $T = 140$°C), presumably since the contribution of the organic resistances becomes small compared

to the contacts and interfaces. The *FF* therefore saturates beyond $T = 50°C$, and eventually decreases above 100°C, possibly due to recombination.

6.2 Temperature dependent absorption broadening

While no known reports of temperature dependent *EQE* exist for OPVs, several reports have shown that J_{SC} increases with temperature in both polymer[129,153,162] and small molecule cells[163], as shown in Fig. 6.3b. This has been attributed to thermally activated mobility of polarons, which increases with temperature.[27,164] To investigate this phenomena further, the *EQE* spectra of the OPV were measured as a function of temperature as shown in Fig. 6.4a, and the ratio of these spectra to the *EQE* at $T = 30°C$ are plotted in Fig. 6.4b. The spectra show a strong wavelength dependence, suggesting that the increase in J_{SC} with temperature comes from a change in charge generation rather than an increase in charge mobility.[130] To confirm this, the reflectance of the OPV was measured as a function of temperature using a beam 6° from normal incidence using a calibrated UV-vis spectrometer. Decreases in reflectance (due to increased absorption) are clearly observed at wavelengths where the *EQE* spectra increased: $\lambda = 540$ nm, 590 nm, 700 nm, and > 800 nm—confirming that charge generation is responsible for the temperature dependence of J_{SC}.

6.2.1 Electron-phonon coupling

Previously, phonon-electron coupling has been shown to cause broadening and red-shifting in the absorption of optical materials.[165–168] Spectral linewidth broadening and the energy shift follow semi-empirical relationships based on the Bose-Einstein distribution:

$$\Gamma(T) = \Gamma_0 \left(1 + \frac{2}{\exp(\Theta/T) - 1}\right) + \Gamma_{HB} \tag{6.1}$$

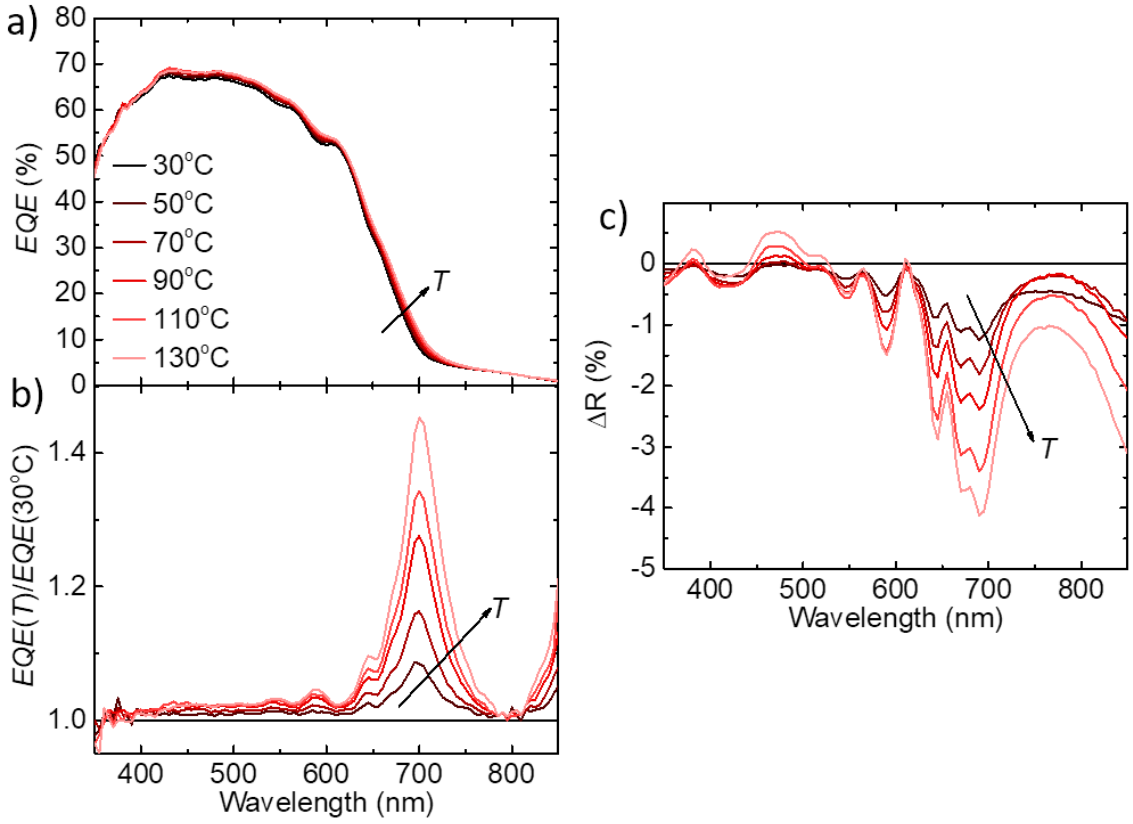

Figure 6.4: **Temperature dependence of *EQE* spectra** | **a)** Temperature dependent *EQE* spectra for a DBP:C_{70} PMHJ OPV. **b)** Wavelength-dependent ratio of the *EQE* at the stated temperature to the *EQE* at 30°C. **c)** Change in reflectance (ΔR) of the OPV at the stated temperature compared with its reflectance at 25°C. Adapted from Q. Burlingame *et al.* (2017).[130]

and

$$E(T) = E_0 - \alpha \left(1 + \frac{2}{\exp(\Theta/T) - 1}\right) \tag{6.2}$$

where $\Gamma(T)$ is the spectral linewidth, $E(T)$ is the energy of the absorption peak, Γ_{HB} is the absorption linewidth due to homogeneous broadening and configurational disorder, E_0 is the peak position at $T = 0$K, Θ is the average phonon temperature, and Γ_0 and α are constants related to the strength of electron-phonon coupling. The low-energy tail of the *EQE* spectra can be closely fit using a sum of three Gaussians (two for monomer absorption, and one for absorption of the DBP:C_{70} CT state), as shown in Fig. 6.5a for $T = 30$°C, from which the FWHMs and peak energies were

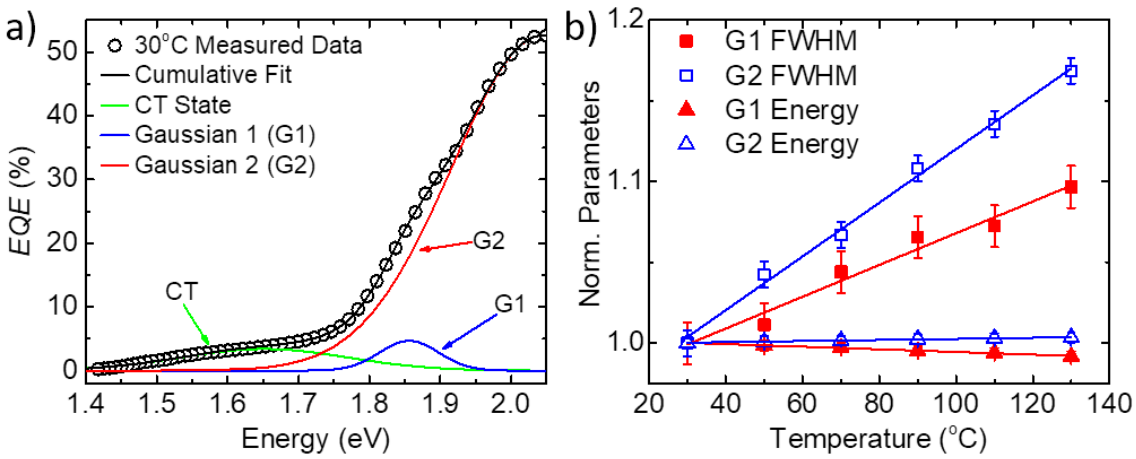

Figure 6.5: **Electron-phonon coupling *EQE* model fits | a)** *EQE* spectra vs. energy at 30°C fitted with a sum of three gaussians: two for monomeric DBP or C_{70} absorption, and a CT state absorption gaussian (green). **b)** FWHM and peak energy extracted from the Gaussians in **a** with fits to Eqs. 6.2 and 6.1. From Q. Burlingame *et al.* (2017).[130]

extracted. Plotting these parameters as a function of temperature, as shown in Fig. 6.5b, we find that they qualitatively agree with fits to Eqs. 6.1 and 6.2, suggesting that phonon-electron coupling is indeed responsible for the temperature dependent increase in J_{SC}. We note however, that $E(T)$ and $\Gamma(T)$ are expected to be nearly linear with temperature at the temperature range explored here,[167,168] thus the high quality of the fits is suggestive of phonon-electron coupling, but not conclusive.

6.2.2 Implications for practical operation

Overall, we find that the diurnal dependence of the OPVs is an aggregate effect of their intensity and temperature dependence. The *FF* and V_{OC} have opposing dependencies on temperature and intensity, *i.e.*, *FF* decreases with intensity and increases with temperature below $T = 50$°C, while V_{OC} decreases with temperature and increases with intensity. Over the course of the day, cell temperature follows a similar shape to the irradiance in Fig. 6.1a, thus the effects of intensity and temperature counteract each other, and *FF* and V_{OC} are flat. The slight increase in responsivity throughout the day leads to a maximum *PCE* at 2:00 pm, which is unexpected

since responsivity should decrease past solar noon as the cell cools. This unexplained increase at dusk may therefore be due to the change in solar spectrum as the sun sets.[169] The intensity and temperature dependencies of the OPVs studied are ideal for outdoor operation, since *PCE* is maximized near 40°C at intensities slightly below 100 mW/cm^2 intensity—identical to the measured outdoor operating conditions.

CHAPTER VII

Accelerated aging of organic photovoltaic cells under high intensity illumination

As discussed in §3.3, accelerated aging methods are critical for the assessment of device operational lifetimes on a practical timescale, particularly for devices such as the PMHJ DBP:C_{70} OPVs described in Chapters V and VI, which show little or no degradation after > 1 year of continuous aging. As Chapter V showed, temperature was ineffective in accelerating the degradation of these OPVs, due to the morphological stability of the active layers and TPBi:C_{70} EF-CBL. In this chapter, we employ high intensity illumination from two sources to accelerate the degradation of OPVs: concentrated solar illumination and high intensity white light LEDs. In general, decoupling the impact of light intensity and temperature on degradation can be a challenge.[127] However, in the devices studied here, their remarkable thermal stability ensures that the irreversible performance degradation observed is purely a result of high intensity light.

7.1 Concentrated solar aging

Encapsulated 54 nm DBP:C_{70} 1:8 HJs and OPVs were exposed to concentrated solar illumination in Sede Boqer, Israel, using the two-axis solar tracking panel, solar

concentrator, and thermoelectric cooling stage described in §3.3. The calibrated J–V characteristics of the OPV under AM1.5G simulated illumination were measured before and after aging for 5 hr under 100 suns of equivalent intensity and are shown in Fig. 7.1a. The V_{OC} showed no change, while J_{SC} decreased by 2% and FF degraded by 5%. The EQE spectra of the cell were also measured before and after this test, as shown in Fig. 7.1b (right axis). A small loss was observed across all wavelengths corresponding to a 2% decrease in J_{SC} calculated from the EQE spectrum using Eq. 1.31. The absorbance of the 54 nm DBPC_{70} 1:8 HJ thin-film showed no change after aging, as shown in Fig. 7.1b (left axis), suggesting that the loss in J_{SC} is a result of decreased charge extraction rather than charge generation. A decreased charge extraction efficiency is consistent with the 5% loss in FF that was also observed.

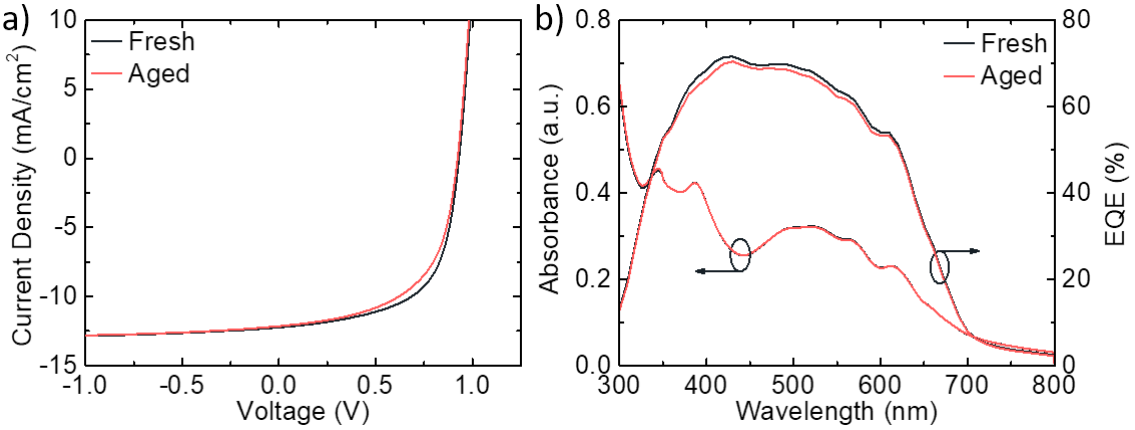

Figure 7.1: **100-sun concentrated solar OPV aging | a)** J–V characteristics of a PMHJ DBP:C_{70} OPV under 100 mW/cm^2 simulated AM1.5G illumination before and after aging for 5 hr under 100 suns of concentrated solar illumination. **b)** Optical absorbance (left-axis) of a 54 nm DBP:C_{70} 1:8 thin film aged under the same condition as **a**, and EQE (right axis) of the device in **a** before and after aging. From Q. Burlingame *et al.* (2016).[81]

7.2 Aging under high intensity white light emitting diodes

Several populations of PMHJ DBP:C_{70} OPVs with TPBi:C_{70} EF-CBLs were aged under high intensity illumination from LEDs while being water cooled as described

in §3.3. The first population of devices was tested at several intensities, with devices under two different electrical load conditions: open-circuit, and in series/parallel with a 100 Ω resistor to bias the OPV near the MPP. The results of these experiments showed no difference in degradation rate between electrical load conditions, thus going forward all devices were aged at V_{OC}. In addition, two undesired degradation modes were observed during aging: the epoxy seal around the periphery of the encapsulated OPV became over-exposed—yellowing with time and, between measurements at 20 days and 50 days, the encapsulation of all devices failed catastrophically. The data shown in this chapter were therefore taken more densely during early times when rapid changes were observed, but still maintained a reasonably close spacing (3 days between points) during longer times to monitor for catastrophic failure. Additionally, the epoxy was covered with a reflective Al foil during aging to protect it from the high intensity illumination, and to ensure that all degradation was confined to the OPV itself.

The OPVs were aged under equivalent solar intensities of 9.5 ± 1.4, 20 ± 3.0, and 37 ± 5.5 suns and periodically removed from the aging setup for measurement. The photovoltaic performance parameters for devices at each intensity were measured under simulated AM1.5G illumination after light soaking intervals and averaged as shown in Fig. 7.2. All devices showed a *PCE* drop of $2-4\%$ within the first 100 hr of aging depending on the intensity. The majority of the total degradation occurred in J_{SC} and *FF*, with *FF* accounting for a majority of the loss at $t > 100$ hr. Nevertheless, all of the devices maintained $> 87\%$ of their initial *PCE* after 1056 hr (44 days) of testing. If we assume an average of 5 kWhr/m^2 of sunlight per day (*e.g.*, 5 hr of equivalent AM1.5G radiation), the 1056 hr of testing at 9.5, 20, and 37 suns corresponds to 5.5, 11.6, and 21.4 years outdoors respectively. Each *PCE* vs. time

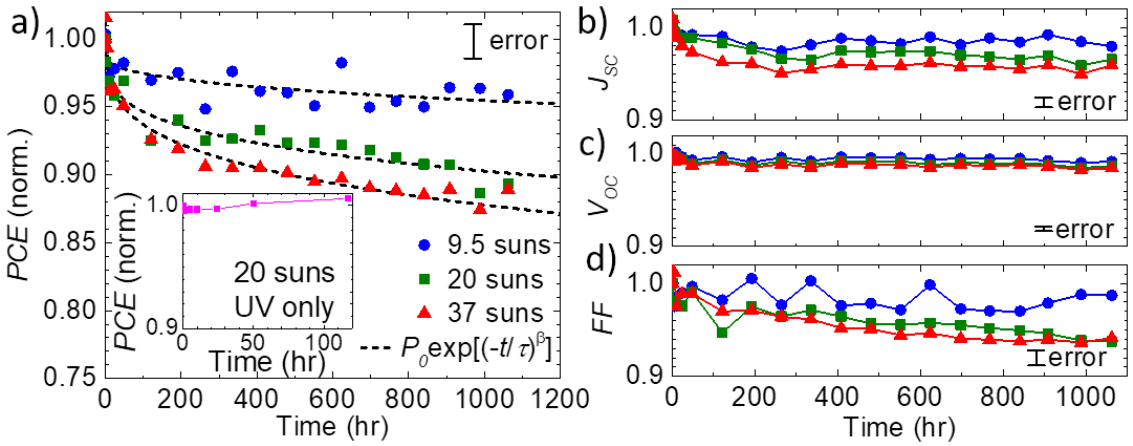

Figure 7.2: **Accelerated OPV aging with high intensity LEDs** | Normalized **a)** *PCE*, **b)** J_{SC}, **c)** V_{OC}, and **d)** *FF* vs. aging time under 9.5, 20, and 37 suns of equivalent illumination from white LEDs. The *PCE* data are each fit with a stretched exponential function. The inset in **a** shows the *PCE* of an OPV aged for 117 hr under 20 suns of equivalent UV radiation.

curve was fit to a stretched exponential function with the form:

$$PCE(t) = P_0 \exp\left[\left(-\frac{t}{\tau}\right)^{\beta}\right], \tag{7.1}$$

as shown in Fig. 7.2a. A potential flaw with the white LED accelerated aging experiments is the lack of UV radiation in their spectra. To test the UV stability of the OPVs, a device was placed under 20 suns of equivalent UV illumination and periodically measured as shown in the inset of Fig. 7.2. No degradation was observed over the 117 hr duration of the experiment, equivalent to the UV dose an OPV would experience after 1.3 years outdoors.

7.2.1 Extrapolated lifetimes and acceleration factor

The implicit goal of accelerated aging is to reliably predict the lifetime of a device under its intended operation conditions and to understand its active degradation modes. To determine the acceleration factor of the devices tested here, we employ Eq. 3.6. As discussed in Chapter V, temperature did not noticably accelerate aging,

thus we ignore the thermally activated term, leaving only:

$$\gamma = \frac{k_{acc}}{k_{ref}} = \left(\frac{I_{acc}}{I_{ref}}\right)^{\xi}. \tag{7.2}$$

The high intensity degradation rate, k_{acc}, is taken from the stretched exponential *PCE* fits to be $1/T_{80}$. The exponential factor ξ can then be determined by fitting $1/T_{80}$ vs. intensity to a simplified function:

$$\frac{1}{T_{80}} = AI_{acc}^{\xi}, \tag{7.3}$$

as shown in Fig. 7.3. Here A is a fitted parameter equal to k_{ref}/I_{ref}^{ξ}. Due to the significant error on the intensity dependent T_{80} fits, both $\xi = 1$ and $\xi = 2$ are within the fitting bounds, making it difficult to precisely determine the acceleration factor. This can also be seen from Fig. 7.4, where the *PCE* data from all intensities are plotted on a time × intensity x-axis and a time × intensity^2 x-axis, corresponding to $\xi = 1$ and $\xi = 2$, respectively. The fact that both plots appear to reasonably represent the trend in the data, and can be well fit with a stretched exponential, is consistent

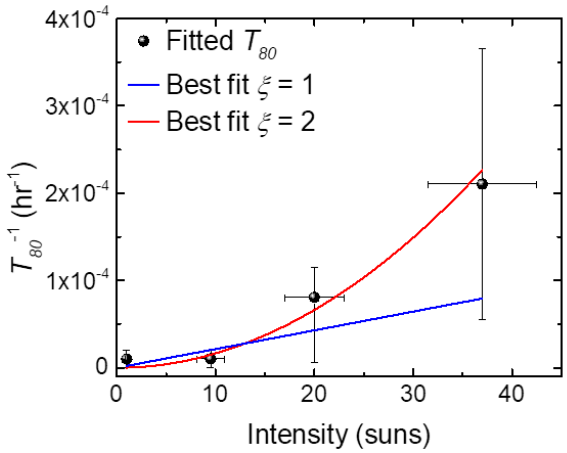

Figure 7.3: **High intensity aging acceleration factor** | $1/T_{80}$ extracted from the stretched exponential fits to *PCE* vs. time in Fig. 7.2a vs. intensity. Best fits to Eq. 7.3 with $\xi = 1$ and $\xi = 2$ are shown.

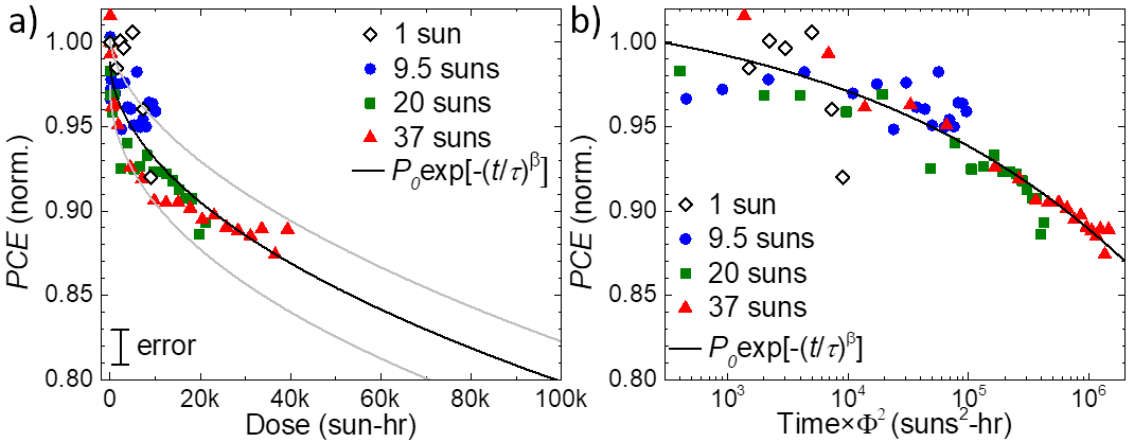

Figure 7.4: **Extrapolated OPV lifetimes from high intensity aging | a)** Irradiation dose (defined as the product of time on test in hr and test intensity (Φ in suns) vs. normalized *PCE* and **b)** intensity^2 $\times$ time vs. normalized *PCE* under 9.5, 20, or 37 suns of equivalent illumination from white LEDs with stretched exponential fits.

with the lack of a well-defined acceleration factor. To extrapolate the lower-bound of lifetime under 1-sun intensity, we therefore assume $\xi = 1$, and extrpolate T_{80} from the stretched exponential fit in Fig. 7.4a. Even this lower bound produces a T_{80} equivalent to 54 ± 14 years outdoors, assuming 5 hr of AM1.5G illumination per day, which far exceeds the longest reported OPV lifetimes to date.

7.2.2 Wavelength-dependent losses

In addition to the illuminated J–V characteristics, the *EQE* of the OPV were measured after each aging interval. The spectra after 44 days of aging are plotted in Fig. 7.5a, along with the change in *EQE* compared to the as-grown device (inset). As we can see, the *EQE* trend has a strong spectral dependence, degrading more at longer wavelengths and increasing slightly at $\lambda < 450$ nm. The direct CT state absorption feature (beyond $\lambda = 700$ nm) is the most strongly affected region of the spectrum, though its contribution to J_{SC} is small. Encapsulated 50 nm thin films of C_{70}, DBP, and a DBP:C_{70} 1:8 blend were also aged for 48 hr under 37 suns on quartz. Transmission of the C_{70} and DBP films remained within 0.5% of their starting values

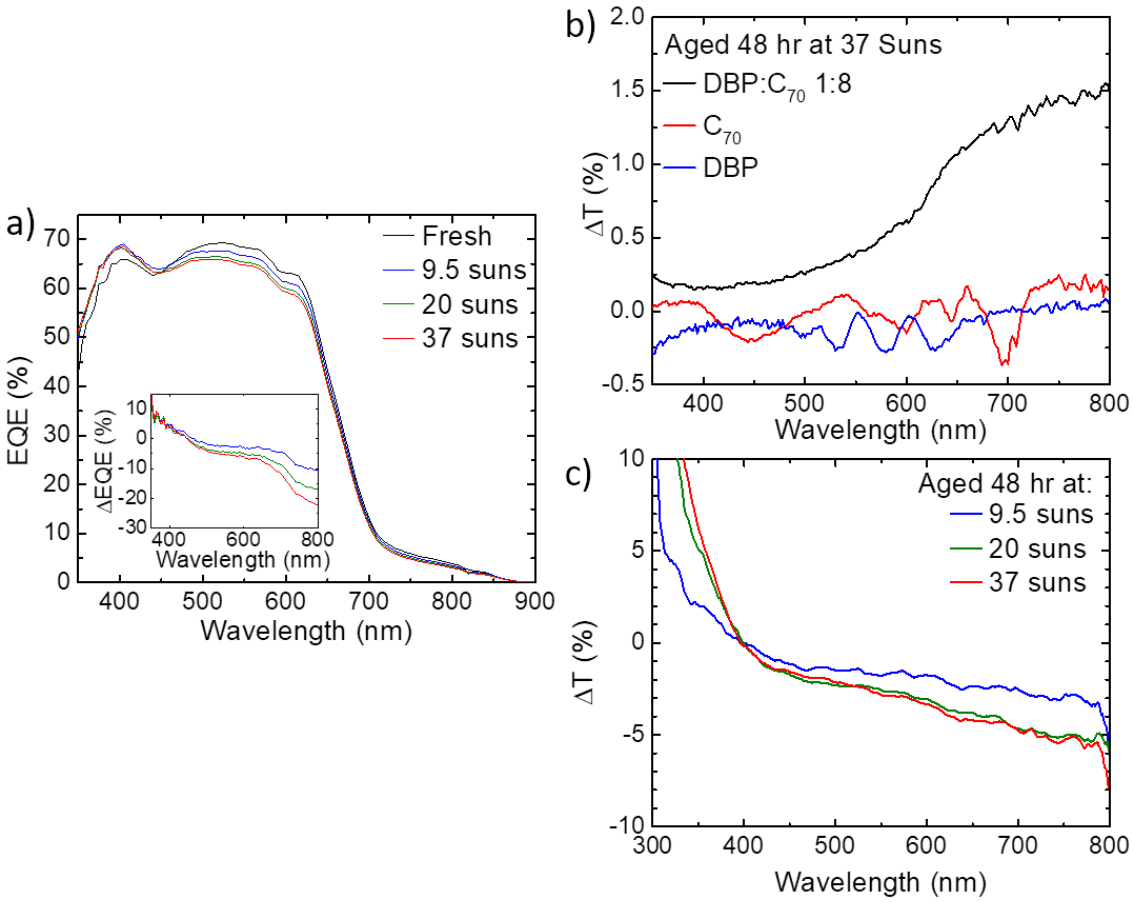

Figure 7.5: ***EQE* and absorption loss after high intensity aging** | **a)** *EQE* spectra of DBP:C_{70} OPVs before and after aging for 44 days under the stated equivalent solar intensity. Inset: percentage change in EQE compared to the as-grown result. **b)** Transmission difference spectra of 50 nm thin films of DBP, C_{70}, and DBP:C_{70} 1:8 on quartz before and after aging for 48 hr at 37 suns. **c)** Transmission difference spectra of ITO-coated substrates with 10 nm of MoO_3 aged under 9.5, 20, and 37 suns equivalent intensity for 48 hr.

across the visible spectrum, as shown in Fig. 7.5b, which is below the 1% resolution of the spectrometer. The DBP:C_{70} HJ thin film showed slightly increased transmission, mirroring the *EQE* loss observed in Fig. 7.5a. While the proximate cause of this absorption loss is not known, AFM micrographs on the films showed that the root-mean-square (RMS) roughness of the aged DBP:C_{70} HJ film was slightly increased after aging (0.8 nm to 1.3 nm), suggesting that morphology shifted slightly. A change in DBP:C_{70} interface area could account for part of the observed loss. However, the

change in absorption is significantly smaller than the change in *EQE* in this region. In addition to the change in absorption of the OPV photoactive materials, the absorption of the anode contact materials (ITO and MoO_3) changed significantly after aging for 48 hr at high intensity as shown in Fig. 7.5c. The MoO_3 appears to be particularly susceptible to degradation, consistent with previous observations by H. Zhang *et al.* (2014).[122] The spectral shape of the transmission change is reflected in the *EQE* spectrum, producing the *EQE* loss at long wavelengths and *EQE* increase at short wavelengths. Interestingly, the losses observed in these inorganic anode materials is significantly larger than the change in transmission of the organics.

7.2.3 Charge extraction efficiency

Applying reverse bias to an OPV assists in charge extraction by reducing the residence time of charges within the device, and liberating charges from shallow traps. However, this effect diminishes with the application of larger voltage since only a certain number of charges are photogenerated, eventually saturating at $J_{photo,sat}$. The voltage-dependent photocurrent of an OPV can therefore be used to determine its $J_{photo,sat}$ and therefore its charge extraction efficiency at J_{SC}, by taking the ratio of $J_{photo}(V = 0)$ to $J_{photo,sat}$. Since the OPVs in this work have relatively thin organic active layers (< 100 nm), we found that they can be easily damaged at sufficiently large reverse bias ($\sim 2 - 3$ V). Since the OPVs were intended to be tested many times over a period of months, their photocurrent generation was only measured to -1.5 V reverse bias to avoid damage, and an exponential fitting function was used to determine their $J_{photo,sat}$:

$$J_{photo}(V) = J_{photo,sat} + c_1 \exp(V/c_2), \tag{7.4}$$

where c_1 and c_2 are constants. Voltage-dependent photocurrent was measured on each device in response to chopped 500 nm illumination using a current amplifier and lock-in amplifier between high intensity aging periods. Data from an as-grown cell and an OPV after aging for 44 days at high intensity are shown in Fig. 7.6a. The data from all aging times and intensities were fit to Eq. 7.4 to calculate the charge extraction efficiency at J_{SC} as shown in Fig. 7.6b. This voltage-dependent loss in charge extraction efficiency produces a J_{SC} loss, and an even more severe FF loss, as the slope of the J–V curves is increasing with time despite the dark R_{SH} remaining almost constant.

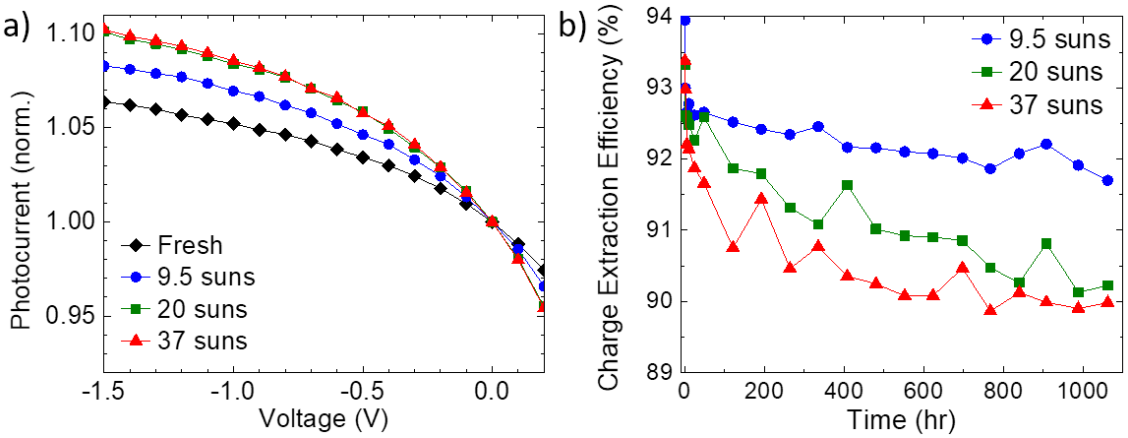

Figure 7.6: **Reverse bias photocurrent generation of aged OPVs | a)** Voltage-dependent photocurrent scans on OPVs aged for 20 days at 9.5, 20, and 37 suns equivalent intensity. All photocurrents were normalized to their value at $V = 0$. **b)** Charge extraction efficiencies as a function of time calculated from the voltage-dependent photocurrent spectra using Eq. 7.4.

The theoretical J_{SC} loss due to the change in ITO/MoO_3 transmission and OPV charge extraction efficiency was simulated as shown in Fig. 7.7. This prediction follows the measured trend in J_{SC} within error, suggesting that these two mechanisms account for a significant majority of the total loss.

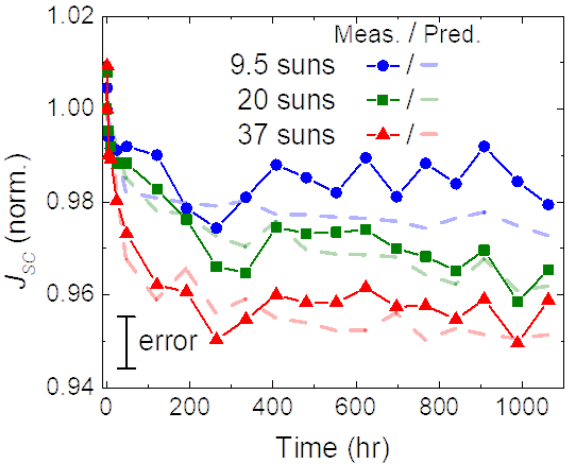

Figure 7.7: **Predicted J_{SC} loss vs. time** | Measured trend in J_{SC} compared to the predicted loss in J_{SC} resulting from the change in ITO/MoO_3 transmission and decrease in charge extraction efficiency vs. time.

7.2.4 Charge-transfer state characterization

The donor-acceptor CT state plays a critical role across many facets of OPV operation, as it typically mediates charge generation from excitons, bimolecular recombination, and can directly absorb and emit photons. In an OPV, CT states can be lost *via* three mechanisms: dissociation into free charge (with rate, k_{diss}), radiative recombination (with a rate, k_{rad}), and non-radiative recombination (with a rate, k_{NR}). The efficiency of CT state dissociation, η_{diss} from Eq. 1.20, should be as high as possible for efficient OPV operation, and can be expressed as a function of the rates above:

$$\eta_{diss} = \frac{k_{diss}}{k_{diss} + k_{rad} + k_{NR}}. \tag{7.5}$$

When operating near open circuit, electrons and holes are forced to recombine—primarily through the CT state. The relationship between radiative and non-radiative recombination can therefore be quantified by measuring electroluminescence quantum efficiency (η_{EL}), defined as the number of photons emitted per charge injected into the device. Between high intensity aging periods, the EL spectra were collected from all OPVs in response to a forward bias current density of 4 mA/cm^2. The spectra

for OPVs aged at 9.5, 20, and 37 suns were normalized to the intensity of the as-grown EL, and are plotted in Fig. 7.8a-c. The peak heights were extracted from these spectra and are plotted as functions of time in Fig. 7.8d. The data show an intensity-dependent burn-in period that saturates within 1-2 days, before stabilizing to a slower degradation rate over the remainder of the 44 day measurement. Only emission from the DBP:C_{70} CT state is observed,[170] and the shape of the spectra are identical regardless of the aging time. This suggests that the emissive species is unchanged with time, while non-radiative recombination competes more favorably with CT emission as the devices age. The emission from the CT states was very dim

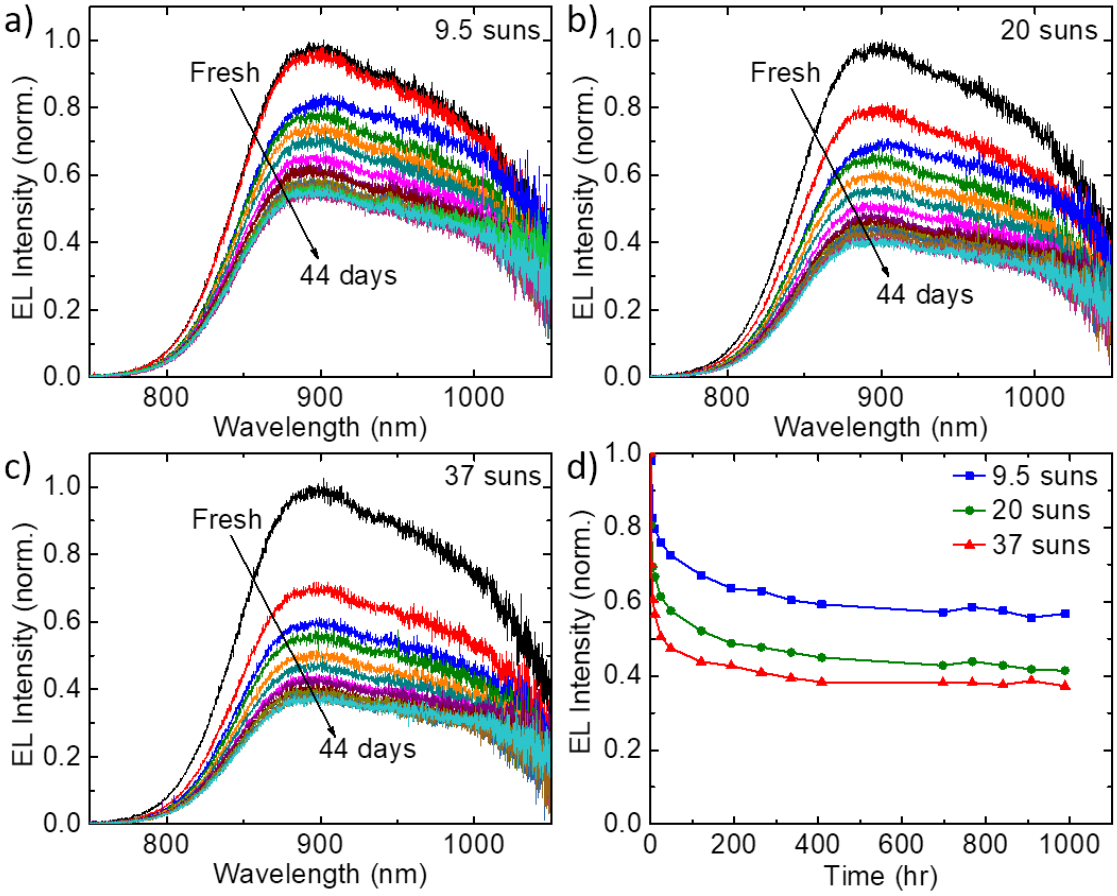

Figure 7.8: **CT state EL spectra vs. time** | EL spectra collected from DBP:C_{70} CT state emission in response to 4 mA/cm^2 forward-bias current as a function of aging under **a)** 9.5 suns, **b)** 20 suns, and **c)** 37 suns. The spectra are normalized to the peak intensity of the as-grown EL spectrum. **d)** Peak heights extracted from these spectra as a function of time.

with an η_{EL} of $7 \times 10^{-4}\%$ in the fresh device.

Despite losing $> 40\%$ of their starting EL intensity, the V_{OC} of the OPVs (as shown in Fig. 7.2) was comparatively stable. From the principal of detailed balance, a solar cell operating at open circuit must radiate a power equivalent to what it absorbs in equilibrium. Since the voltage of a cell increases with its charge density, solar cells that build up a large steady-state charge density before reaching equilibrium will produce a larger V_{OC}. The upper limit of the time required to reach this equilibrium is set by the intrinsic radiative lifetime of each material system, except in cases where photons can be trapped in the device and recycled.[171,172] Any recombination which occurs in addition to intrinsic radiative decay reduces the equilibrium charge density at open circuit and therefore reduces V_{OC}. As a result, it has been shown many times both in theory and practice that V_{OC} is approximately proportional to $\ln(\eta_{EL})$.[171–175] Here, we quantify the expected change in V_{OC} due to the change in η_{EL} using the equation:

$$\Delta V_{OC}(t) = \frac{k_B T}{q} A \ln\left(\frac{\eta_{EL}(t=0)}{\eta_{EL}(t)}\right), \tag{7.6}$$

where A is a fitting prefactor related to J_{SC}, the injection current at the measurement condition, and the equilibrium charge density generated in the OPV from black body absorption. The ΔV_{OC} using this approach and the measured ΔV_{OC} are plotted in Fig. 7.9, with $A = 0.41$. While the overall change in V_{OC} with time is very small (< 20 mV at all intensities), its trend is closely matched by this analysis, confirming that increased non-radiative recombination is likely responsible.

7.2.5 Probes of chemical degradation

As we observed in Fig. 7.5b, the transmission spectra of DBP and C_{70} films are stable after high intensity aging. However, such measurements are ineffective at resolving chemical changes that affect $< 1\%$ of molecules in the film. To look with higher sensitivity, we employ two additional techniques to evaluate 50 nm thin films on

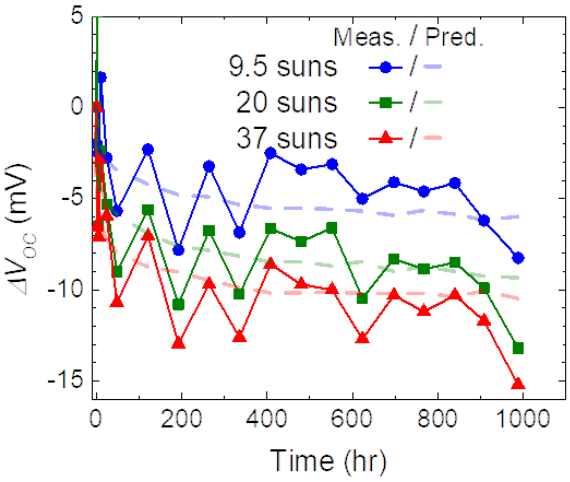

Figure 7.9: ***V_{OC}* degradation under high intensity** | Measured change in V_{OC} as a function of time compared to its predicted value from the change in η_{EL} using Eq. 7.6.

quartz after high intensity aging: photoluminescence (PL) lifetime measurements and LDI-TOF mass spectrometry, as shown in Fig. 7.10. Time-resolved PL measurements were performed using a time-correlated single photon counter coupled to a Si single photon avalanche detector. The excitation wavelength was 500 nm, applied in 150 fs pulses with a 1 kHz repetition rate from a Ti:sapphire laser pumped optical parametric amplifier (OPA). Light from the laser was blocked from the detector with a 550 nm long-pass filter. The PL lifetime of C_{70} was 413 ± 6 ps and showed no change after aging as shown in Fig. 7.10a, while the lifetime of DBP PL emission decreased significantly from 893 ± 8 to 599 ± 6 ps. The chemical origins of this PL lifetime decrease are clear from the mass spectra shown in Fig. 7.10b, where a significant increase in peak heights at 727 m/z and 649 m/z was observed relative to the DBP monomer peak at 805 m/z. These peaks correspond to the mass of DBP with 1 or 2 of its peripheral phenyl groups removed. No changes were observed in the mass spectra of the C_{70} film, consistent with its unchanged PL lifetime.

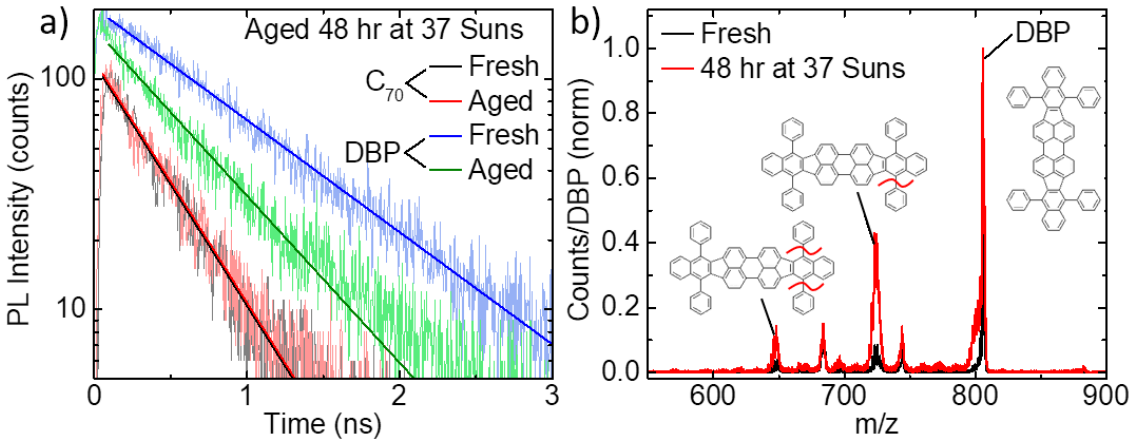

Figure 7.10: **Aged film transient PL and mass spectrometry** | **a)** Transient PL from 50 nm films of DBP and C_{70} on quartz after aging for 48 hr at 37 suns of equivalent intensity from white LEDs. **b)** Normalized mass spectra from a DBP thin film before and after aging under the same conditions. Inset: chemical structure of DBP.

7.2.6 Transient DBP:C_{70} photoluminescence

Transient PL spectra were also collected from CT emission from an aged DBP:C_{70} 1:8 HJ film, using the same setup described above. Due to the weak emission of the CT state, the signal was integrated for $>$ 3 hr and plotted for the fresh and aged film as shown in Fig. 7.11. While the signal is noisy, no change was observed in PL lifetime. Thus blending DBP into C_{70} either reduces its tendency to photochemically degrade, or the degraded DBP fragments do not affect the lifetime of CT states.

7.2.7 Summary of high intensity aging

The high intensity aging results in this chapter show the remarkable potential of OPVs to be a highly reliable source of electricity after optimization with the right chemicals and device architecture. Indeed, the least stable component of the PMHJ DBP:C_{70} OPVs with TPBi:C_{70} EF-CBLs explored here were the inorganic anode materials: ITO and MoO_3.

Unlike temperature in Chapter V, intensity was found to be effective at accelerating OPV degradation. Both J_{SC} and V_{OC} decreased monotonically with intensity,

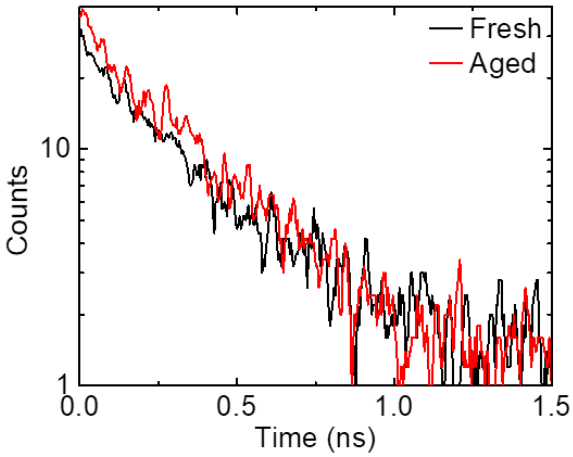

Figure 7.11: **Transient PL from aged HJ films** | CT state transient PL collected from a 50 nm DBP:C_{70} thin film aged for 48 hr under 37 suns on quartz.

which was due to a combination of decreased charge extraction efficiency, parasitic absorption of the anode materials, and increased non-radiative recombination as evidenced by the decrease in electroluminescence with time. The *FF* was primarily responsible for long-term degradation, as charge extraction became increasingly voltage dependent with time due to the increase in recombination. The acceleration factor of degradation could not be precisely resolved due to the spread of the data, thus to extrapolate lifetime we employed the most conservative approach with $\xi = 1$ in Eq. 7.2. The T_{80} from this analysis was found to be 54 ± 14 years, by far the longest reported for any OPV. However, unlike some reports,[176] the measured data here cover a significant range of the extrapolation (nearly 1/2), since aging continuously for 44 days at 37 suns gives a photon dose equivalent to what an OPV would absorb in 21.4 years outdoors. The fact that OPVs aged under such conditions retain nearly 90% of their initial *PCE*, suggests that this extrapolation of intrinsic lifetime is indeed reliable.

CHAPTER VIII

Outlook for highly stable organic photovoltaic cells and future work

Table 8.1 shows the number of publications utilizing several small molecule photoactive materials and HJ architectures since 2005. As we can see, a number of trends are present: Pc-based donors are being gradually replaced with novel donor materials; C_{70}, $PC_{71}BM$, and NFAs are increasingly dominating over C_{60} and $PC_{61}BM$; and blended HJs have become increasingly popular over planar HJs. Not shown in Table 8.1 are the results from polymer OPVs with solution-processed NFAs, which have garnered perhaps the most attention from the OPV lifetime community over the past 2-3 years. In general, though, the real driver of trends in OPV material and architecture choices is efficiency. Each of the trends listed above also correlates with improved efficiency. This is an encouraging sign for the viability of OPVs, as there appears to be a generally positive correlation between efficiency and reliability. However, the *PCE* gap between the most efficient OPVs ($PCE > 15\%$) and OPVs with a published lifetime ($PCE = 7 - 8\%$) has never been larger. Reports of device lifetime seem to lag several months or years behind the publication of a new device architecture with improved efficiency. Given that literature reports have demonstrated that OPVs are capable of commercially-viable efficiencies[3,4] and semi-transparent performance,[12] and that this thesis has established the potential for OPVs to be extremely robust—

Table 8.1: **Trends in the small molecule OPV literature** | Number of published results utilizing various monomeric materials and HJ architectures.[41,81,84,87,89–96,98–100,102,103,111,115,140–142,177–184] Compiled from Clarivate Analytics Web of Science in September, 2018, using the search terms: "Organic photovoltaic small molecule," and "reliability," "stability," "lifetime," or "degradation," References that included data or references to shelf-life, thermal aging, or illuminated aging of OPV devices were included. Data from unique material systems that were included in the same reference are counted individually. *S.P.=solution-processed.

		Publication Year (20xx)													
		'05	-	-	-	-	'10	-	-	-	-	'15	-	-	'18
Donor	CuPc	1	1	1			3	2	1		2		1		
	ZnPc				1		1	2	2		1	1			
	SubPc						1			1	2	3			
	Other Pc						1				2				
	S.P.*										1	2	5	6	2
	DTDCPB										1				
	cHBC													2	
	DBP												1	1	1
Acceptor	C_{60}	1	1	1	1		4	3	3	1	6	4	1	1	
	C_{70}						1			1	2	3	1	1	1
	$PC_{61}BM$							1					4	2	
	$PC_{71}BM$										1	2	4	4	2
	NFA										1		1		
	cHBC										1			1	
HJ Arch.	Planar	1	1	1			4	1	2	1	4	3	1	2	
	Mixed				1			3	1	1	5	5	6	7	3
	Tandem				1										

closing the efficiency-stability gap is the key to the commercialization of OPVs. This chapter will discuss the design considerations that have led to the observed increase

in OPV lifetimes, and how these may be integrated into high efficiency devices. In addition, this chapter will speculate about the potential lifetime of novel materials and architectures, and propose future work that has not yet been addressed by the OPV community.

8.1 General design principles for stability

As Chapters IV, V, and VII have shown, the photochemical and morphological stabilities of the materials that comprise OPVs play a critical role in determining device reliability. Surprisingly, the data from Appendix A (summarized in Table 4.1) indicate that most thermally-evaporated small molecule films are stable under continuous solar illumination within the $\sim 1\%$ resolution of FTIR and optical absorption measurements. Morphological stability is much more variant, with some (*e.g.*, TPBi and BP4mPy) demonstrating high stability, and others (*e.g.*, BPhen, DTDCPB, and DTDCTB) readily crystallizing under standard operating conditions. The most morphologically stable molecules share particular traits, such as their bulky, non-planar structure, and high transition temperatures (T_G and T_m) that reduce π-stacking and molecular motion in thin films. Blending of dissimilar materials also appears to provide a substantial benefit to device stability—limiting the size of crystalline domain growth, and impeding molecular diffusion.[81,98] While each material must be evaluated on a case-by-case basis, morphological and photochemical stability can be assessed prior to device fabrication, and are predictive of operational stability.

Based on optical simulations,[18] the PMHJ DBP:C_{70} OPVs in this work absorb approximately 30% of the incident solar power. A majority of this is absorbed by the photoactive layers, with a small percentage absorbed by the contacts, transport layers, and substrate.[130] Of the absorbed energy, only 22% is converted into usable electricity; thus 78% is dissipated through other means, primarily through heat generation and re-radiation. Under 1-sun intensity, the excess energy amounts to 26

mW/cm^2 that can drive degradation. The key to extending OPV reliability therefore, is management of this excess energy and rapidly converting it into forms that are non-destructive to the device. By far the most beneficial way to do this is by increasing the *PCE* of the OPV, as this limits the excess energy available for degradation. While there will always be excess energy converted to heat in an OPV, this can be overcome through morphological stabilization of the organic materials as discussed above.

The most potentially destructive form of energy is therefore "hot" excitations, which can be generated by absorption of blue/UV photons, or through Auger annihilation processes (*e.g.*, exciton–exciton, polaron–polaron, or exciton–polaron). These excitations can significantly exceed the requisite energy to break chemical bonds and dissociate molecules, which will proceed with a rate: $k_{destruction}N_x$, where $k_{destruction}$ is the rate at which high energy excitations cleave bonds, and N_x is the density of high energy excitations. If such states are found to be a primary driver of OPV degradation, two strategies are available to limit their impact: reducing N_x by filtering high energy light or rapidly quenching the excitations; and ensuring that non-destructive relaxation pathways are available to compete favorably with $k_{destruction}$. Blended HJ architectures are suited to this purpose, as they significantly reduce the lifetime of excited states by quenching them through charge transfer processes. Another approach proposed by J. S. Lee *et al.* (2017)[185] for use in OLEDs is to mix a sacrificial "manager" molecule into the active layer. The manager is designed to collect high energy excitations and prevent them from dissociating materials in the active layer. Finally, diluting the populations of excitons and charges over a larger area is also beneficial. Thus, increasing active layer thicknesses, and utilizing multi-junction cells can provide additional benefits to OPV lifetime.

8.1.1 Diagnosing failure mechanisms

Fully characterizing OPV degradation requires understanding three distinct aspects: what component within the device is degrading and how; the energy source driving the degradation; and how the underlying degradation process couples to device performance. As this thesis has shown, characterization of individual thin films that comprise an OPV can help isolate weak points in the device. In addition to these measurements, studying the wavelength-dependent *EQE* of the OPV as it ages can be instructive. Degradation that disproportionately affects some wavelengths is likely due to a loss in charge generation (*e.g.*, absorption or exciton diffusion), and may appear predominately where the acceptor or donor absorb, thus implicating that element. Degradation that occurs equally across all wavelengths is more likely a result of decreased charge extraction, due perhaps to the appearance of charge traps or interfacial energy barriers. Determining the energy source responsible for degradation requires a series of controlled experiments that test the OPV's stability under different stressors, such as elevated temperatures, various electrical load conditions, or light sources with different spectral content (*e.g.*, with or without UV filtering). The aging acceleration factor from Eq. 3.6 under high intensity can help to disentangle the contributions of photons, excitons, and charges on device lifetime, with photochemical processes accelerating linearly with photon flux and Auger processes proceeding quadratically.

8.2 Outlook for next generation organic solar cells

Next generation non-transparent OPVs with $> 20\%$ *PCE* and semi-transparent OPVs with high *PCE* and intense absorption in the UV and IR portions of the solar spectrum are sure to appear within the next several years, given the rapid progress in these areas over the past several years. Based on current trends in the technology,

series-connected multi-junction OPVs and semi-transparent, near-IR/UV absorbing cells will almost surely be utilized toward these goals. This section will speculate on the possible challenges each of these classes of device will face in terms of its stability, and how these challenges might be overcome.

8.2.1 Multi-junctions

The fundamental nature of semiconductors absorbing light from a spectrally broad source imposes a theoretical limit on the efficiency of a solar cell. This is because photons below the energy gap cannot be absorbed, and photons absorbed with energies larger than the semiconductor's energy gap will dissipate their excess energy into phonons. For a given illuminant, there will therefore be a single ideal energy gap to produce the best tradeoff between lost low-energy absorption and high-energy thermalization. Using detailed balance, W. Shockley and H.J. Queisser (1960)[186] calculated this limit for a blackbody illuminant with a CCT of 6000 K (similar to that of the sun), finding a maximum *PCE* of 30% at $E_G = 1.1$ eV. If instead, the standard AM1.5G spectrum is used as the illuminant, a peak *PCE* of 33.16% can be achieved at an energy gap of 1.34 eV,[187] which is typically referred to as the Shockley-Queisser or SQ limit. For an OPV with an exciton binding energy and decreased free energy at the HJ, the SQ limit becomes 27% according to N.C. Giebink *et al.* (2011).[188]

To overcome this fundamental limit, multiple junctions can make more efficient use of photons in several spectral bands. For example, a tandem with two junctions can absorb green/blue photons using a junction with an energy gap of 1.6 eV, and can absorb red/near-IR photons in a second junction with an energy gap of 0.8 eV. In this case, photons absorbed by the green/blue cell retain twice the energy that would have thermalized otherwise if absorbed by the red/near-IR cell, while the red/near-IR subcell significantly expands the absorption of the cell. Part of the appeal of organ-

ics for solar cell applications is how readily they can be integrated into monolithic multi-junction cells with series connections between subcells, allowing them to reduce thermalization losses while maintaining a high optical absorption. When optimized, each subcell generates the same photocurrent under illumination, and thus the efficiency of the tandem is proportional to the sum of the voltages from each cell. As was discussed in the previous section, spreading the charge and exciton populations more broadly throughout an OPV and making more efficient use of absorbed energy should provide a significant benefit to reliability.

To test this hypothesis, the lifetime of a series of subcells and multi-junction cells were tested as shown in Fig. 8.1. The green-absorbing subcell was a modified PMHJ DBP:C_{70} cell with the structure: 6 nm MoO_3 / 30 nm DBP:C_{70} 1:10 / 7 nm C_{70} / 10 nm TPBi:C_{70}, and the red-absorbing cell had the structure: 10 nm MoO_3 / 60 nm DTDCTB:C_{60} / 6 nm TPBi:C_{70} / 2nm PTCBI. The lifetime of each of these subcells was measured with a 100 nm Al cathode as shown in Fig. 8.1a-b, and tandem cells were fabricated by growing the green-absorbing subcell directly on top of the red-absorbing subcell with a 0.1 nm layer of Ag between them and a 100 nm Al cathode on top as shown in Fig. 8.1c. The 3-junction cell shown in Fig. 8.1d used two green-absorbing cells sandwiching a red-absorbing cell with a 100 nm Al cathode on top and 0.1 nm Ag layers between each subcell. The green-absorbing DBP:C_{70} cell is highly stable as discussed in Chapters V and VII, with the J_{SC} loss coming entirely from the spectral shift of the Xe lamp. The red-absorbing subcell is considerably less stable, with all three paramaters degrading by 12-21% of their starting values by 1500 hr. When integrating these subcells into the tandem and 3-junction OPVs, the lifetime significantly improves. This suggests that multi-junction structures can be employed (even with slightly unstable subcells) to stabilize their performance for long-term operation.

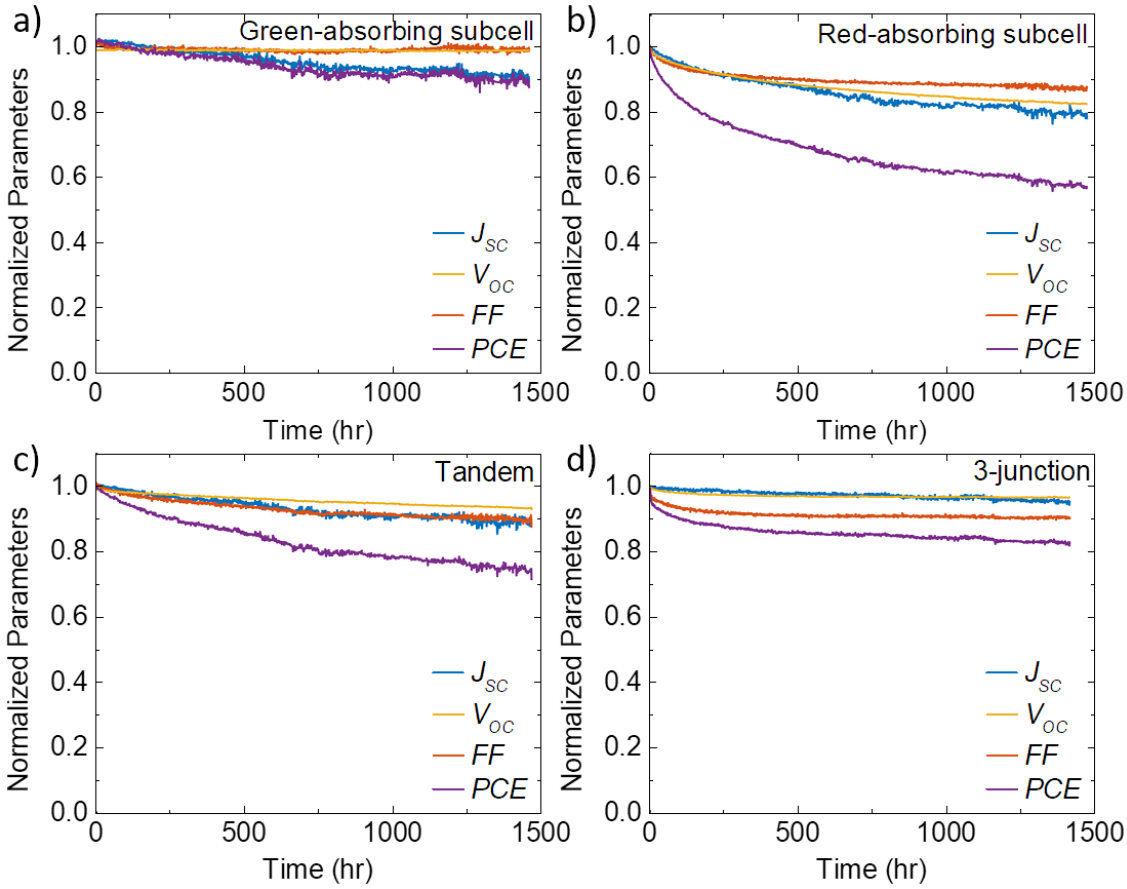

Figure 8.1: **Tandem and 3-junction OPV lifetimes** | Evolution of the normalized photovoltaic characteristics: J_{SC}, V_{OC}, FF, and PCE as a function of time under 100 mW/cm^2 simulated AM1.5G illumination for a **a)** green-absorbing DBPC$_{70}$ subcell, **b)** red-absorbing DTDCTB:C$_{60}$ subcell, **c)** tandem cell employing one of each subcell, and textbfd) 3-junction OPV with two green-absorbing cells sandwiching a red-absorbing cell.

8.2.2 Semi-transparent organic photovoltaic cells

Unlike conventional semiconductor solar cells, organic molecules are almost infinitely tunable, and can be made to absorb (and transmit) light in different portions of the spectrum. One of the most promising applications for this unique property is integration into windows that generate electrical power while remaining aesthetically pleasing and semi-transparent. In terms of energy generation, the vertical orientation of windows is a drawback, since (in the continental U.S.) the incidence angle of the sun is around 65° in the winter and only around 18° in the summer when the solar

flux is highest. This corresponds to a $9\% - 69\%$ incident power loss compared to a panel oriented normal to the sun's irradiance. In addition, adjacent structures and trees can potentially shade vertical panels further reducing the flux they receive. A significant portion of their power is therefore generated from diffuse light. However, the reduced solar flux on vertical panels is potentially a beneficial property for device lifetimes—particularly if the degradation is accelerated by high intensity, as was the case for the OPVs shown in this thesis.

The near-infrared portion of the solar spectrum contains a large share of its photons, thus OPVs that only absorb wavelengths beyond 650 nm can still easily surpass 10% *PCE*, while remaining almost completely transparent to visible light. Preliminary results in our group on the lifetimes of such cells with solution-processed NFAs have thus far been disappointing: typically $T_{80} < 300$ hr, as shown in Fig. 8.2. One possible reason for this is the presence of thiophene (C_4H_4S) groups in the near-IR absorbing active materials. The carbon–sulfur bond is relative weak compared to carbon–carbon and carbon–hydrogen bonds, which may introduce photochemical instability in these systems. Filtering out high energy light may be a partial solution to

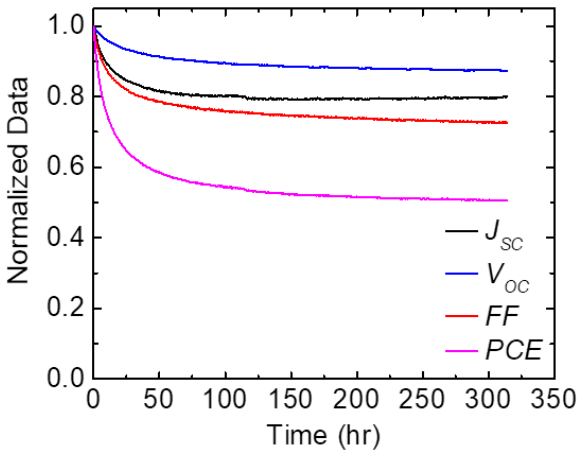

Figure 8.2: **Semi-transparent OPV lifetime** | Evolution of the normalized photovoltaic characteristics: J_{SC}, V_{OC}, *FF*, and *PCE* for a solution-processed semi-transparent OPV with polymer PCE-10 as the donor and NFA BT-CIC as the acceptor.

this problem,[48,105,176,189] but it is likely that further chemical modification will also be required. Additionally, solution-processed small molecules are difficult to purify, and thus likely introduce unintended impurities on the order of 0.01-1%, which may also negatively impact lifetime.[190] Making thermally-evaporable, near-IR absorbing molecules and eliminating sulfur would likely improve their stability, but this may be a challenge as the molecules are typically quite large and have relatively low molecular dissociation temperatures.

An alternative approach to near-IR absorbing semi-transparent cells is to generate power from the near-UV portion of the solar spectrum. While there are far fewer photons in this spectral region, each has a much higher energy that can produce a large output voltage in devices. The molecules that absorb in this region can also be made thermally-evaporable and almost entirely from hydrocarbons, which is favorable for photochemical stability. Lifetime reports on near-UV absorbing OPVs with contorted hexabenzocoronene (cHBC) derivative active regions show a strong burn-in during the first 30 hr of illumination, where $\sim$ 27% of the initial efficiency is lost before stabilizing.[41] However, those devices include a planar BCP cathode buffer layer, which is likely to morphologically degrade over time as has been shown in conventional non-transparent OPVs.[141] Semi-transparent, near-UV absorbing OPVs may therefore offer a longer intrinsic lifetime compared to near-IR absorbing OPVs, although their power output is limited by the low photon flux in the near-UV portion of the solar spectrum. Semi-transparent, series-connected tandems that include both near-IR and near-UV subcells are somewhat impractical, as the current mismatch is extremely large.

8.3 Proposed future work

The core challenge remaining for OPV research is to unify high efficiency and high reliability into a single device architecture and materials system. One approach to this

challenge is to study and optimize the lifetime of existing OPVs with a high reported efficiency. However, the impact of such studies beyond the particular materials system used is difficult to gauge, as each material system and device architecture undergo a unique combination of failure mechanisms. The primary aim of the work in Chapters IV, V, and VII was to develop models, methodologies, and principles that can be applied to an arbitrary materials system and inform the design of high stability OPVs. The remainder of this chapter will propose several potential routes for the stabilization of future OPV materials and devices.

8.3.1 Low free energy organic thin film growth

The primary causes of morphological degradation, as discussed in Chapter V, are molecular mobility and a large free energy difference between the as-grown and crystalline phases of a film. Consider a material with a T_G that is comparable to the operating temperature of an OPV. If grown into an amorphous film, and the driving force, ΔG_v, is sufficiently large, then molecules will become mobile at temperatures near T_G and will reorient to minimize their potential energy. Other than changing the material itself, or blending it with a dissimilar molecule, morphological rearrangement of the amorphous film is inevitable. One possible solution to this problem is to grow the initial film in a more stable semi-crystalline morphology. In 2015, B. Song *et al.*[87] demonstrated that growth using organic vapor phase deposition (OVPD) produces increased crystallinity in a co-deposited DBP:C_{70}. In that work, the roughened active layer was used to pin the morphology of a BPhen cathode buffer layer grown on top of it. Given that DBP:C_{70} films appear to be morphologically stable even when grown by VTE, no increase in active layer stability was noted in that work. However, if this technique were applied to a different materials system that does suffer from morphological instability (for example OPVs with DTDCTB or DTDCPB as the donor), then the increased crystallinity of the HJ film could stabilize its long-term

morphology. In principle, this method could be applied to any thermally-evaporable materials system, and may allow for materials systems that would be impractical from a reliability standpoint when grown by standard VTE to be sufficiently stable when grown in a less unstable phase.

8.3.2 Morphological stabilization with a ternary element

Solution-processed ternary OPVs have recently produced some of the highest recorded solar cell efficiencies,[47,48] which is often attributed to the morphological benefit and tunability that the third element provides.[191] However, such results have not yet been reported in vacuum-deposited OPVs, particularly with respect to their lifetime. It may therefore be possible to add a third component to the photoactive HJ of an OPV that contributes a small amount of photocurrent by acting as a 2nd donor or acceptor, while favorably stabilizing the as-grown morphology of the blend. From a morphological perspective, co-depositing a third element that is not photoactive yet highly dissimilar to the existing donor and acceptor, may stabilize the morphology of the blend without disrupting photogeneration and charge transfer, comparable to what was observed in Chapter V when blending a fullerene into BPhen to form an EF-CBL. The best candidates for this purpose are likely bulky molecules with a highly stable amorphous phase such as BP4mPy.

8.3.3 Design of sterically hindered buffer materials

Where possible, chemical modification of particular chemicals in an OPV structure may provide a significant benefit to reliability without significantly reducing performance. One such modification is to develop molecules that are sterically inhibited from crystallization. Such modifications may be difficult within the photoactive and transport materials, as close coupling between nearest-neighbor molecules is essential to high electrical conductivity. However, buffer layers, such as exciton blockers may

be candidates for modification—particularly since several of these compounds have been shown to have significant morphological instabilities. Here, we propose a deplanarized exciton blocking molecule based on BPhen that includes two peripheral fluorene ($C_{13}H_{10}$) groups, which will orient themselves perpendicular to the plane of the backbone of the molecule. This proposed compound is called 9,9'-spirobifluorenyl-bathophenanthroline (sF-BPhen), and is shown in Fig. 8.3 alongside BPhen. The bulky structure of sF-BPhen should significantly impede its crystallization, leading to a stabilized thin-film morphology compared to BPhen.

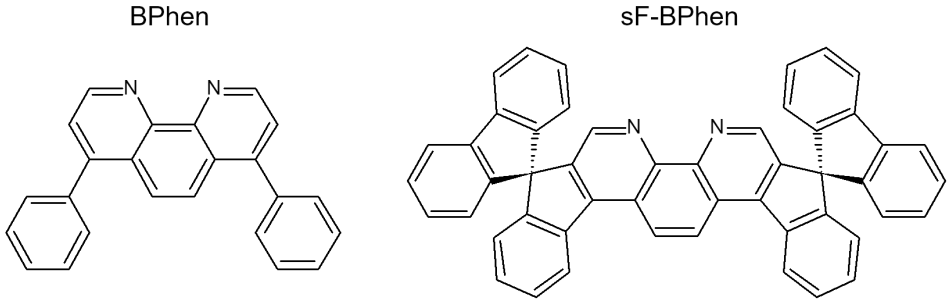

Figure 8.3: **Proposed structure of 9,9'-spirobifluorenyl-BPhen** | Chemical structural formulae of BPhen, and a proposed modified version 9,9'-spirobifluorenyl-BPhen (sF-BPhen) with two added fluorene groups to deplanarize its structure and impede crystallization.

8.3.4 Reliable cold-weld bonded laminate encapsulation

While this dissertation has focused on the intrinsic failure of OPVs, robust packaging is equally important for the long-term viability of OPV technology. Rigid glass-glass packages sealed with epoxy can achieve the robustness required for OPV encapsulation. However, the cost, weight, and inflexibility of these packages is not compatible with the desired form factor of many OPVs applications that look to make use of their light weight and flexibility. The ideal encapsulant is therefore flexible and low cost, without sacrificing robustness. The most common proposed materials for this application are multi-layer composite films, with alternating flexible polymer and

thin inorganic barrier layers, such as SiN_x. To join such a barrier layer to an OPV module, direct lamination with a tacky adhesive could be used to align the substrate and encapsulation film, as shown in Fig. 8.4. However, the edge seal using such a barrier would have high water vapor transmission rate ($WVTR$). To seal the edge, a thin layer of metal (such as Au) could be deposited around the periphery of both the substrate and encapsulation film. Maintaining a clean interface between these materials, the cap and substrate could be bonded by passing the roll through a cold-weld bonding press.[192] A cold-weld bond joins the two metal surfaces together as if they were one continuous metal, under sufficent pressure, heat, and time. Such a bond could provide an excellent hermetic seal to the edge of the OPV package.

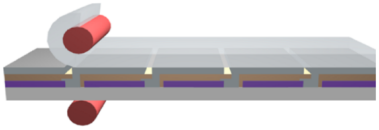

Figure 8.4: **Roll-to-roll encapsulation scheme** | The barrier film (pre-coated with an adhesive) is rolled and pressed into contact with the OPV module substrate.

APPENDIX

APPENDIX A

FTIR spectra of aged organic thin films

Thin films of each of the organic compounds used in this work were aged for 1 week under the following conditions: in N_2 in the dark; in air in the dark; in N_2 under 100 mW/cm^2 Xe arc lamp illumination; and in air under 100 mW/cm^2 Xe arc lamp illumination. In addition to these conditions, C_{60} thin films were aged under 1-sun in air through a PC window to filter out the UV portion of the Xe arc lamp spectrum and in the dark in air on a hotplate at 65°C. Infrared absorption spectra were collected before and after aging as shown in Figs. A.1-A.13. The FTIR spectrometer was purged with N_2 during the measurement to limit the atmosphere O_2, CO_2, and H_2O. The spectra were manually baseline corrected after the measurement. The CO_2 absorption band from $\sim$ 600 to $\sim$ 700 cm^{-1} is omitted from all spectra for clarity. These results are also summarized in Table 4.1.

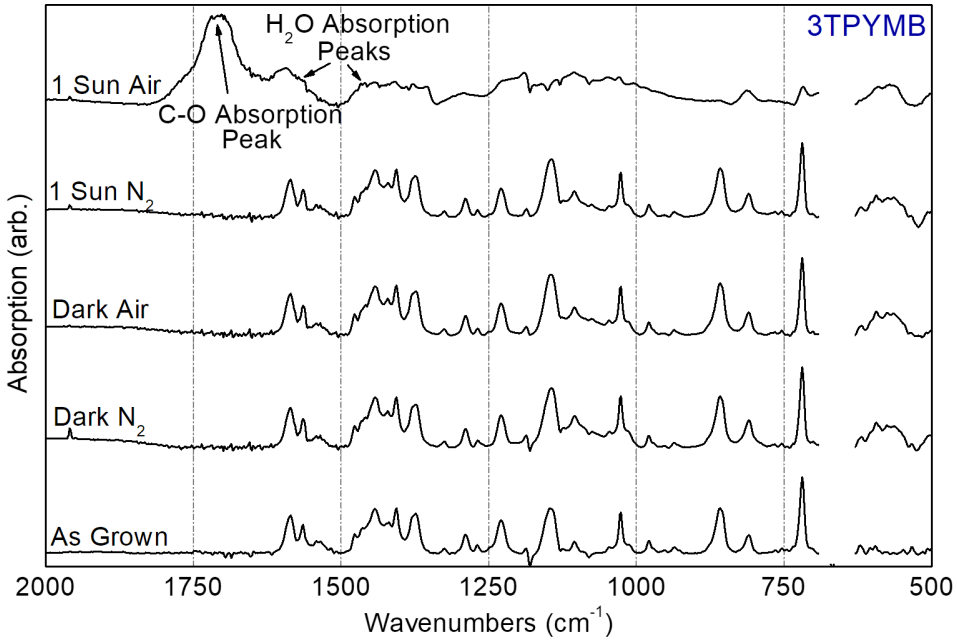

Figure A.1: **3TPYMB FTIR spectra** | FTIR absorption spectra of 100 nm 3TPYMB thin films before and after aging for 1 week at the stated conditions.

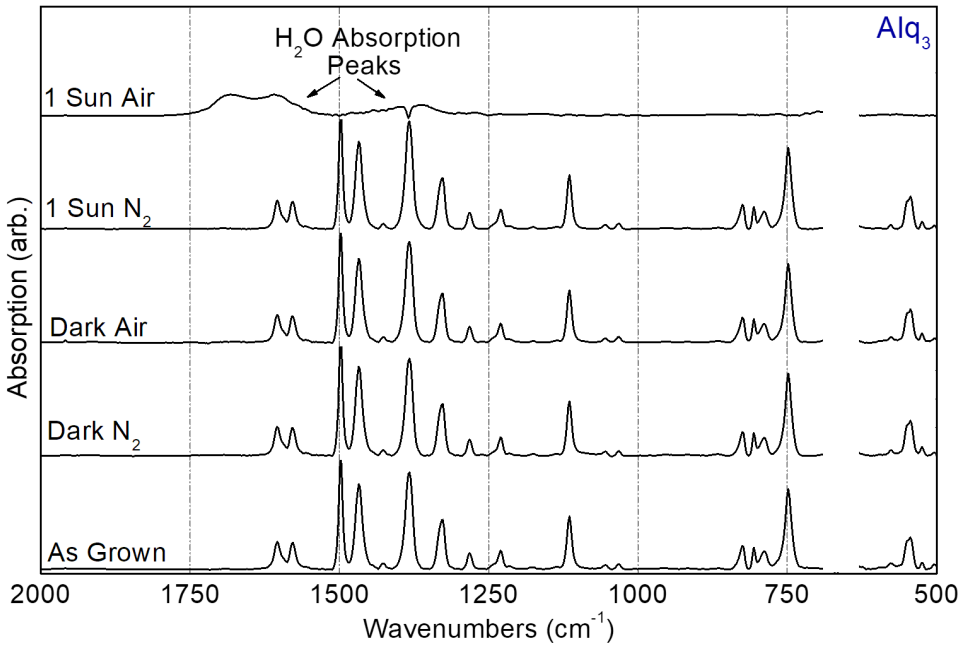

Figure A.2: **Alq_3 FTIR spectra** | FTIR absorption spectra of 100 nm Alq_3 thin films before and after aging for 1 week at the stated conditions.

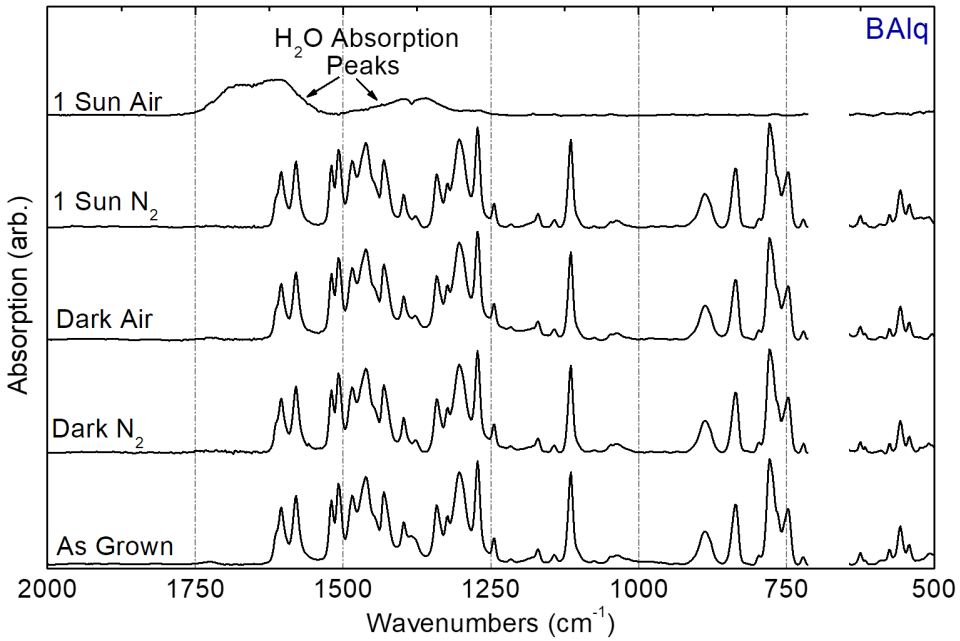

Figure A.3: **BAlq FTIR spectra** | FTIR absorption spectra of 100 nm BAlq thin films before and after aging for 1 week at the stated conditions.

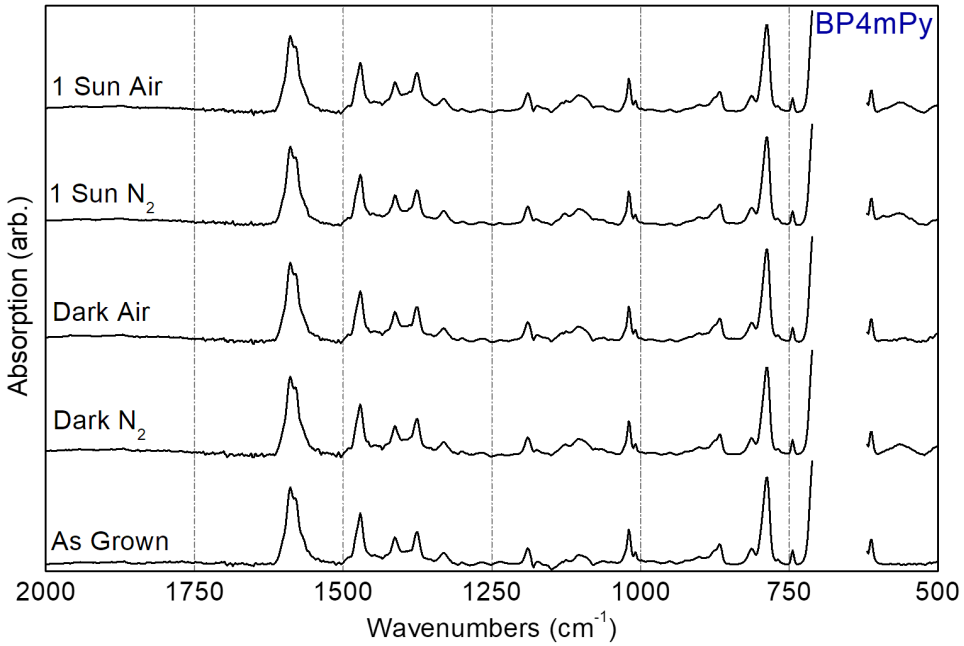

Figure A.4: **BP4mPy FTIR spectra** | FTIR absorption spectra of 100 nm BP4mPy thin films before and after aging for 1 week at the stated conditions.

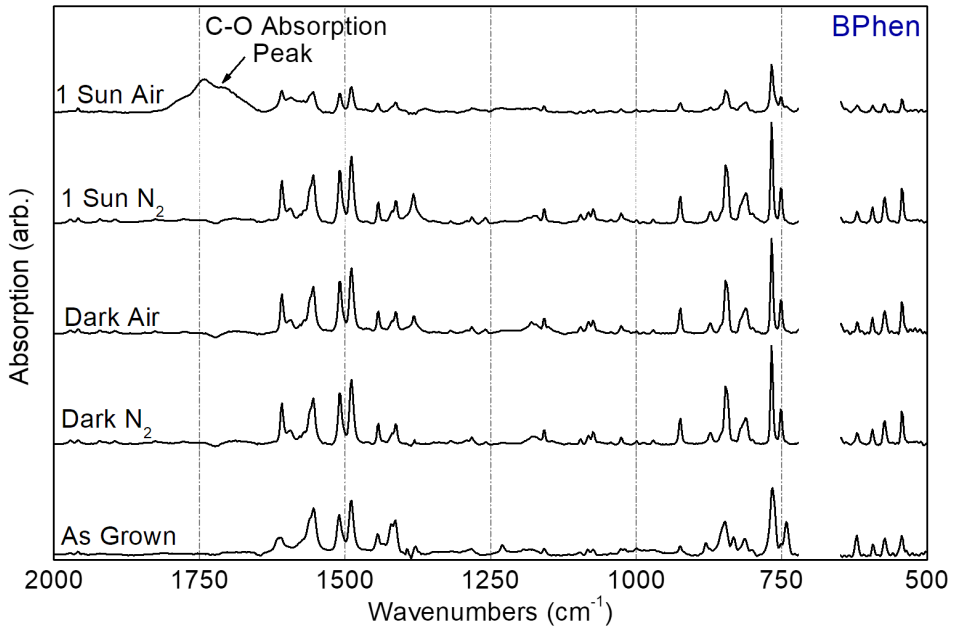

Figure A.5: **BPhen FTIR spectra** | FTIR absorption spectra of 100 nm BPhen thin films before and after aging for 1 week at the stated conditions.

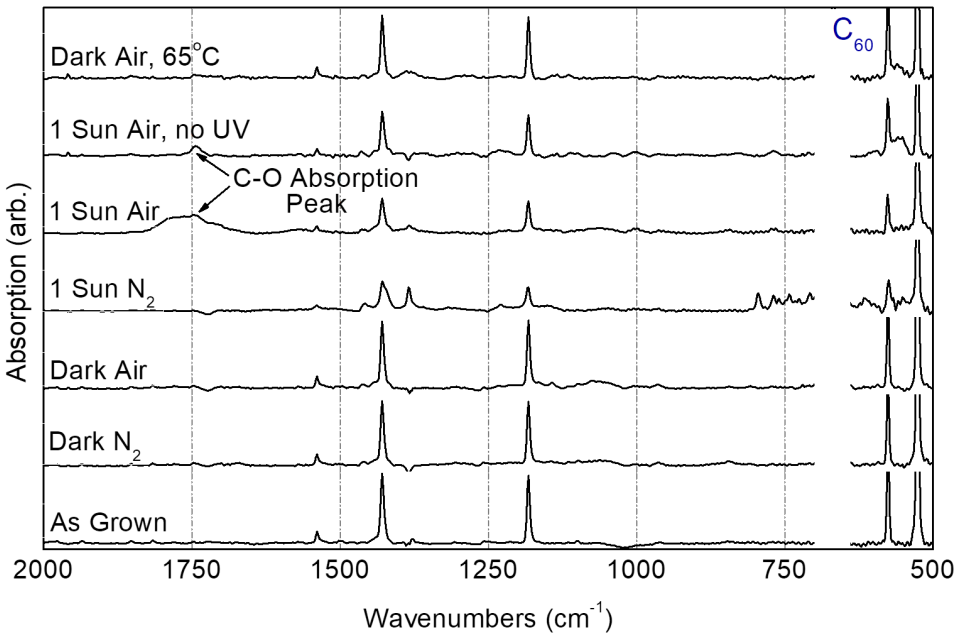

Figure A.6: **C_{60} FTIR spectra** | FTIR absorption spectra of 100 nm C_{60} thin films before and after aging for 1 week at the stated conditions.

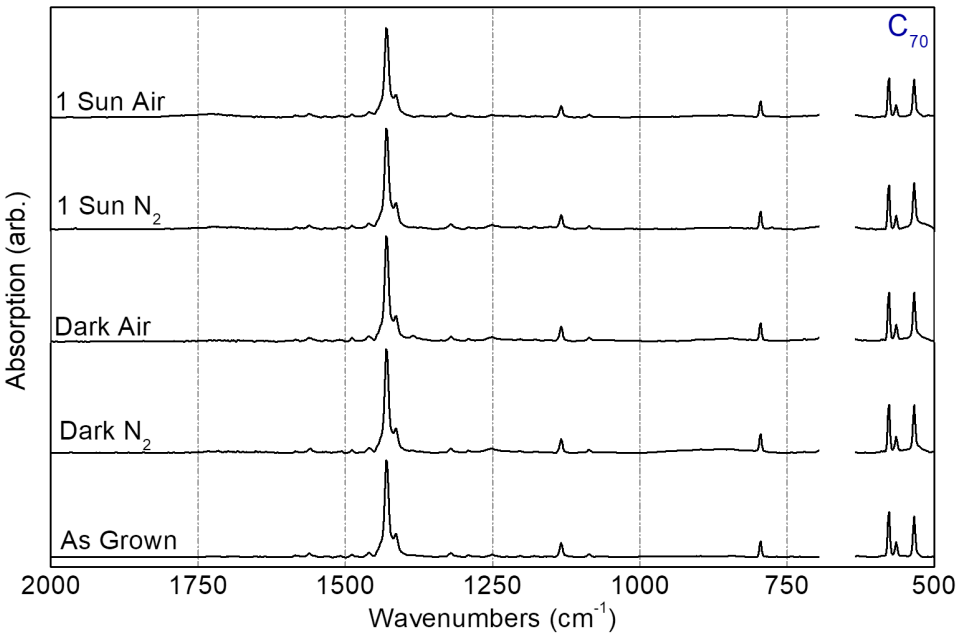

Figure A.7: **C_{70} FTIR spectra** | FTIR absorption spectra of 100 nm C_{70} thin films before and after aging for 1 week at the stated conditions.

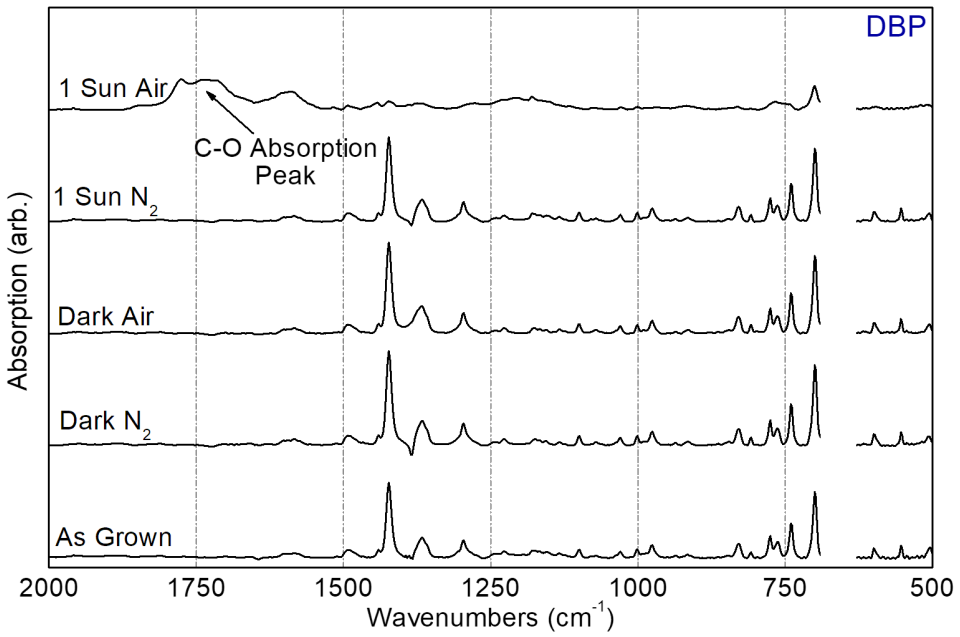

Figure A.8: **DBP FTIR spectra** | FTIR absorption spectra of 100 nm DBP thin films before and after aging for 1 week at the stated conditions.

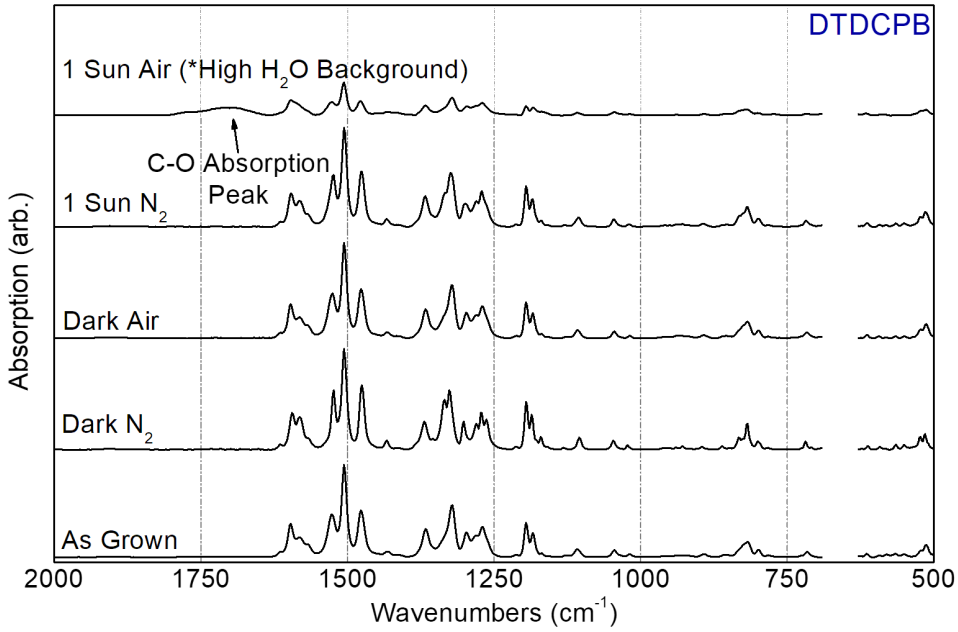

Figure A.9: **DTDCPB FTIR spectra** | FTIR absorption spectra of 100 nm DTDCPB thin films before and after aging for 1 week at the stated conditions.

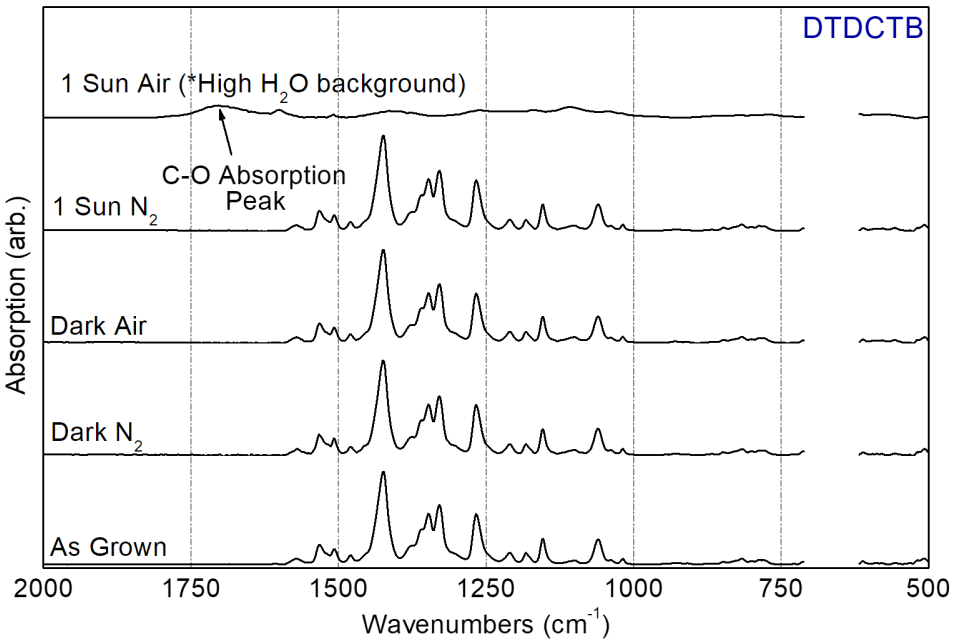

Figure A.10: **DTDCTB FTIR spectra** | FTIR absorption spectra of 100 nm DTDCTB thin films before and after aging for 1 week at the stated conditions.

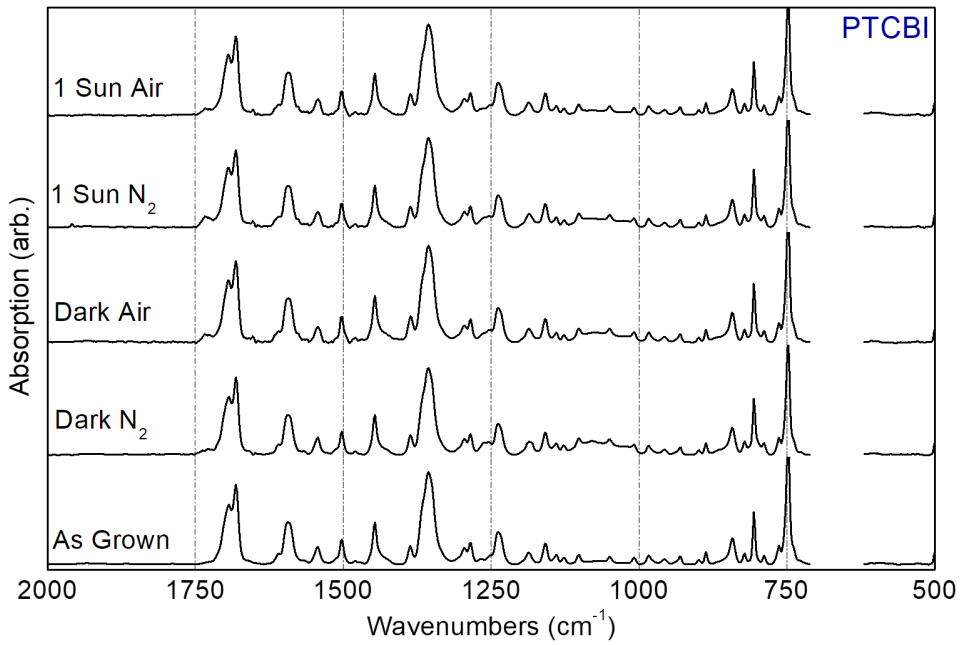

Figure A.11: **PTCBI FTIR spectra** | FTIR absorption spectra of 100 nm PTCBI thin films before and after aging for 1 week at the stated conditions.

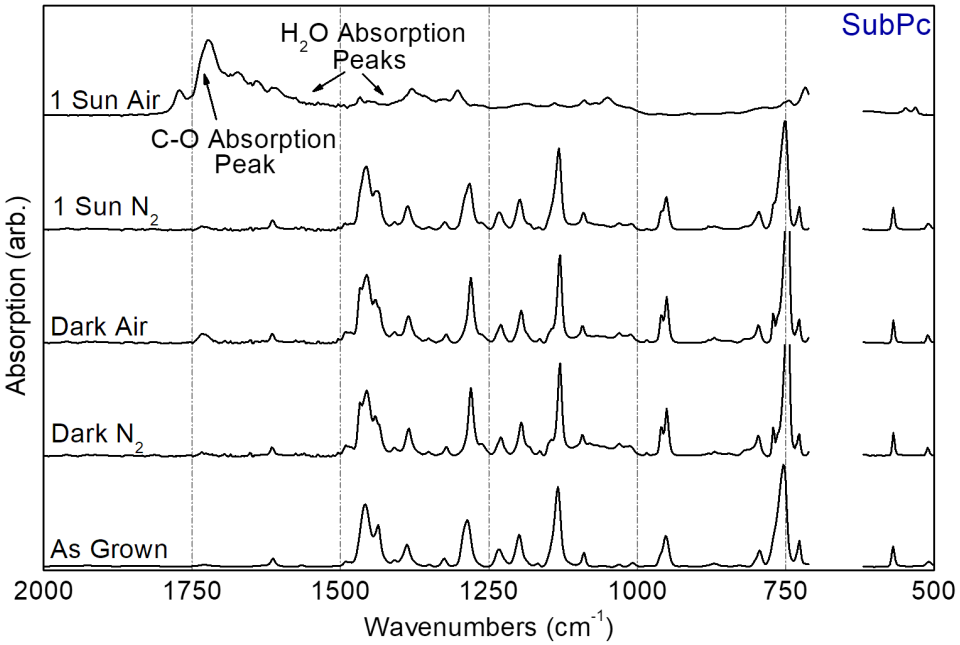

Figure A.12: **SubPc FTIR spectra** | FTIR absorption spectra of 100 nm SubPc thin films before and after aging for 1 week at the stated conditions.

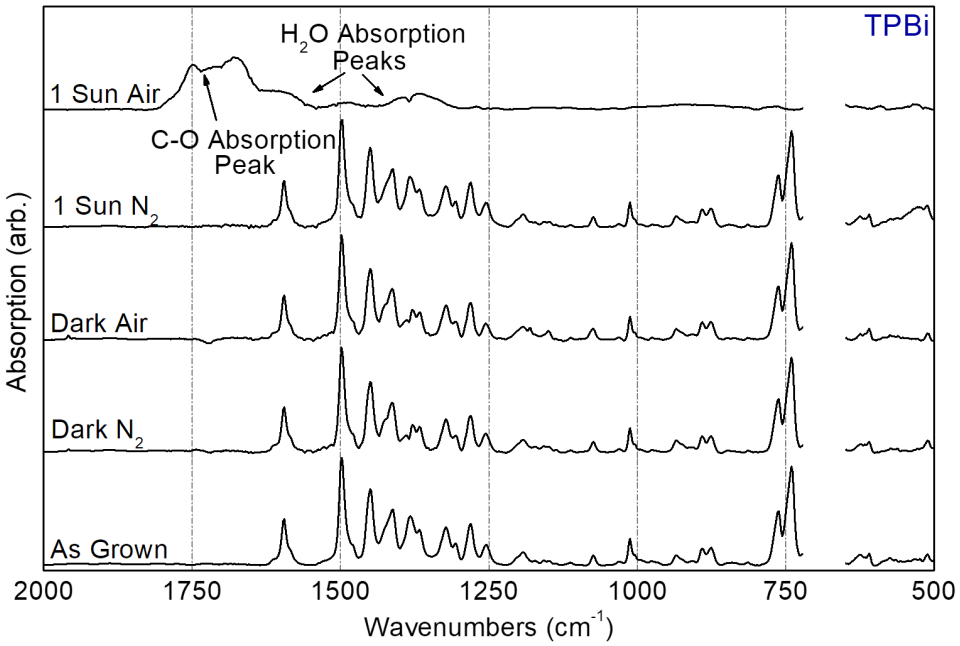

Figure A.13: **TPBi FTIR spectra** | FTIR absorption spectra of 100 nm TPBi thin films before and after aging for 1 week at the stated conditions.

BIBLIOGRAPHY

[1] Forrest, S. R. The path to ubiquitous and low-cost organic electronic appliances on plastic. *Nature* **428**, 911–918 (2004).

[2] Tang, C. W. Two-layer organic photovoltaic cell. *Applied Physics Letters* **48**, 183–185 (1986).

[3] Che, X., Li, Y., Qu, Y. & Forrest, S. R. High fabrication yield organic tandem photovoltaics combining vacuum- and solution-processed subcells with 15% efficiency. *Nature Energy* **3**, 422–427 (2018).

[4] Meng, L. *et al.* Organic and solution-processed tandem solar cells with 17.3% efficiency. *Science* (2018).

[5] Polman, A., Knight, M., Garnett, E. C., Ehrler, B. & Sinke, W. C. Photovoltaic materials: Present efficiencies and future challenges. *Science* **352**, 307 (2016).

[6] Mathew, S. *et al.* Dye-sensitized solar cells with 13% efficiency achieved through the molecular engineering of porphyrin sensitizers. *Nature Chemistry* **6**, 242–247 (2014).

[7] Chuang, C.-H. M., Brown, P. R., Bulović, V. & Bawendi, M. G. Improved performance and stability in quantum dot solar cells through band alignment engineering. *Nature Materials* **13**, 796–801 (2014).

[8] Sai, H., Matsui, T., Matsubara, K., Kondo, M. & Yoshida, I. 11.0%-efficient thin-milm microcrystalline silicon solar cells with honeycomb textured substrates. *IEEE Journal of Photovoltaics* **4**, 1349–1353 (2014).

[9] Tan, H. *et al.* Efficient and stable solution-processed planar perovskite solar cells *via* contact passivation. *Science* **355**, 722–726 (2017).

[10] Jackson, P. *et al.* Properties of Cu(In,Ga)Se_2 solar cells with new record efficiencies up to 21.7%. *Physica Status Solidi (RRL) Rapid Research Letters* **9**, 28–31 (2015).

[11] Yoshikawa, K. *et al.* Silicon heterojunction solar cell with interdigitated back contacts for a photoconversion efficiency over 26%. *Nature Energy* **2**, 17032 (2017).

[12] Li, Y. *et al.* High efficiency near-infrared and semitransparent non-fullerene acceptor organic photovoltaic cells. *Journal of the American Chemical Society* **139**, 17114–17119 (2017).

[13] Søndergaard, R., Hösel, M., Angmo, D., Larsen-Olsen, T. T. & Krebs, F. C. Roll-to-roll fabrication of polymer solar cells. *Materials Today* **15**, 36–49 (2012).

[14] Gu, X. *et al.* Roll-to-roll printed large-area all-polymer solar cells with 5% efficiency based on a low crystallinity conjugated polymer blend. *Advanced Energy Materials* **7**, 1602742 (2017).

[15] Qu, B. & Forrest, S. R. Continuous roll-to-roll fabrication of organic photovoltaic cells *via* interconnected high-vacuum and low-pressure organic vapor phase deposition systems. *Applied Physics Letters* **113**, 053302 (2018).

[16] Brabec, C. J., Egelhaaf, H.-J. & Salvador, M. The path to ubiquitous organic electronics hinges on its stability. *Journal of Materials Research* **33**, 1839–1840 (2018).

[17] Tang, C. W. & Van Slyke, S. A. Organic electroluminescent diodes. *Applied Physics Letters* **51**, 913–915 (1987).

[18] Peumans, P., Yakimov, A. & Forrest, S. R. Small molecular weight organic thin-film photodetectors and solar cells. *Journal of Applied Physics* **93**, 3693–3723 (2003).

[19] Kozlov, V. G., Bulović, V., Burrows, P. E. & Forrest, S. R. Laser action in organic semiconductor waveguide and double-heterostructure devices. *Nature* **389**, 362–364 (1997).

[20] Marian, C. M. Spinorbit coupling and intersystem crossing in molecules. *Wiley Interdisciplinary Reviews: Computational Molecular Science* **2**, 187–203 (2012).

[21] Adachi, C., Baldo, M. A., Thompson, M. E. & Forrest, S. R. Nearly 100% internal phosphorescence efficiency in an organic light-emitting device. *Journal of Applied Physics* **90**, 5048–5051 (2001).

[22] Geacintov, N. E., Binder, M., Swenberg, C. E. & Pope, M. Exciton dynamics in α-particle tracks in organic crystals: Magnetic field study of the scintillation in tetracene crystals. *Physical Review B* **12**, 4113–4134 (1975).

[23] Förster, T. Zwischenmolekulare energiewanderung und fluoreszenz. *Annalen der Physik* **437**, 55–75 (1948).

[24] Dexter, D. L. A theory of sensitized luminescence in solids. *The Journal of Chemical Physics* **21**, 836–850 (1953).

[25] Gill, W. D. Drift mobilities in amorphous chargetransfer complexes of trinitrofluorenone and poly-n-vinylcarbazole. *Journal of Applied Physics* **43**, 5033–5040 (1972).

[26] Bässler, H. Hopping conduction in polymers. *International Journal of Modern Physics B* **8**, 847–854 (1994).

[27] Bässler, H. Charge transport in disordered organic photoconductors a Monte Carlo simulation study. *Physica Status Solidi B* **175**, 15–56 (1993).

[28] Roichman, Y. & Tessler, N. Generalized Einstein relation for disordered semiconductors—implications for device performance. *Applied Physics Letters* **80**, 1948–1950 (2002).

[29] Cahen, D., Kahn, A. & Umbach, E. Energetics of molecular interfaces. *Materials Today* **8**, 32–41 (2005).

[30] Graham, K. R. *et al.* The roles of structural order and intermolecular interactions in determining ionization energies and charge-transfer state energies in organic semiconductors. *Advanced Energy Materials* **6**, 1601211 (2016).

[31] Burlingame, Q. *et al.* Centimetre-scale electron diffusion in photoactive organic heterostructures. *Nature* **554**, 77–80 (2018).

[32] Gaynor, W., Burkhard, G. F., McGehee, M. D. & Peumans, P. Smooth nanowire/polymer composite transparent electrodes. *Advanced Materials* **23**, 2905–2910 (2011).

[33] Kim, A., Won, Y., Woo, K., Kim, C.-H. & Moon, J. Highly transparent low resistance ZnO/Ag nanowire/Zno composite electrode for thin film solar cells. *ACS Nano* **7**, 1081–1091 (2013).

[34] Yang, L. *et al.* Solution-processed flexible polymer solar cells with silver nanowire electrodes. *ACS Applied Materials & Interfaces* **3**, 4075–4084 (2011).

[35] Khan, A. *et al.* High-performance flexible transparent electrode with an embedded metal mesh fabricated by cost-effective solution process. *Small* **12**, 3021–3030 (2016).

[36] Tenent, R. C. *et al.* Ultrasmooth, large-area, high-uniformity, conductive transparent single-walled-carbon-nanotube films for photovoltaics produced by ultrasonic spraying. *Advanced Materials* **21**, 3210–3216 (2009).

[37] Barnes, T. M. *et al.* Carbon nanotube network electrodes enabling efficient organic solar cells without a hole transport layer. *Applied Physics Letters* **96**, 243309 (2010).

[38] Gomez De Arco, L. *et al.* Continuous, highly flexible, and transparent graphene films by chemical vapor deposition for organic photovoltaics. *ACS Nano* **4**, 2865–2873 (2010).

[39] Wu, J. *et al.* Organic solar cells with solution-processed graphene transparent electrodes. *Applied Physics Letters* **92**, 263302 (2008).

[40] Xiao, X., Lee, K. & Forrest, S. R. Scalability of multi-junction organic solar cells for large area organic solar modules. *Applied Physics Letters* **106**, 213301 (2015).

[41] Davy, N. C. *et al.* Pairing of near-ultraviolet solar cells with electrochromic windows for smart management of the solar spectrum. *Nature Energy* **2**, 17104 (2017).

[42] Lucera, L. *et al.* Printed semi-transparent large area organic photovoltaic modules with power conversion efficiencies of close to 5%. *Organic Electronics* **45**, 209–214 (2017).

[43] Zhou, Y. *et al.* A universal method to produce low–work function electrodes for organic electronics. *Science* **336**, 327–332 (2012).

[44] Yu, G., Gao, J., Hummelen, J. C., Wudl, F. & Heeger, A. J. Polymer photovoltaic cells: enhanced efficiencies *via* a network of internal donor-acceptor heterojunctions. *Science* **270**, 1789–1791 (1995).

[45] Halls, J. J. M. *et al.* Efficient photodiodes from interpenetrating polymer networks. *Nature* **376**, 498–500 (1995).

[46] Xue, J., Rand, B., Uchida, S. & Forrest, S. A hybrid planarmixed molecular heterojunction photovoltaic cell. *Advanced Materials* **17**, 66–71.

[47] Lu, L., Kelly, M. A., You, W. & Yu, L. Status and prospects for ternary organic photovoltaics. *Nature Photonics* **9**, 491–500 (2015).

[48] Baran, D. *et al.* Reducing the efficiency-stability-cost gap of organic photovoltaics with highly efficient and stable small molecule acceptor ternary solar cells. *Nature Materials* **16**, 363–369 (2017).

[49] Bartynski, A. N. *et al.* A fullerene-based organic exciton blocking layer with high electron conductivity. *Nano Letters* **13**, 3315–3320 (2013).

[50] Xiao, X., Bergemann, K. J., Zimmerman, J. D., Lee, K. & Forrest, S. R. Small-molecule planar-mixed heterojunction photovoltaic cells with fullerene-based electron filtering buffers. *Advanced Energy Materials* **4**, 1301557 (2014).

[51] Bergemann, K. J., Amonoo, J. A., Song, B. S., Green, P. F. & Forrest, S. R. Surprisingly high conductivity and efficient exciton blocking in fullerene/wide-energy-gap small molecule mixtures. *Nano Letters* **15**, 3994–3999 (2015).

[52] Giebink, N. C., Wiederrecht, G. P., Wasielewski, M. R. & Forrest, S. R. Ideal diode equation for organic heterojunctions. I. derivation and application. *Physical Review B* **82**, 155305 (2010).

[53] Giebink, N. C., Lassiter, B. E., Wiederrecht, G. P., Wasielewski, M. R. & Forrest, S. R. Ideal diode equation for organic heterojunctions. II. the role of polaron pair recombination. *Physical Review B* **82**, 155306 (2010).

[54] Besold, S. *et al.* Quantitative imaging of shunts in organic photovoltaic modules using lock-in thermography. *Solar Energy Materials and Solar Cells* **124**, 133–137 (2014).

[55] Servaites, J. D., Yeganeh, S., Marks, T. J. & Ratner, M. A. Efficiency enhancement in organic photovoltaic cells: Consequences of optimizing series resistance. *Advanced Functional Materials* **20**, 97–104 (2010).

[56] Gueymard, C. A. The sun's total and spectral irradiance for solar energy applications and solar radiation models. *Solar Energy* **76**, 423–453 (2004).

[57] Gueymard, C. A., Myers, D. & Emery, K. A. Proposed reference irradiance spectra for solar energy systems testing. *Solar Energy* **73**, 443–467 (2002).

[58] Krueger, A. J. & Minzner, R. A. A mid-latitude ozone model for the 1976 U.S. Standard Atmosphere. *Journal of Geophysical Research* **81**, 4477–4481 (1976).

[59] Marion, W. & Wilcox, S. *Solar radiation data manual for flat-plate and concentrating collectors* (National Renewable Energy Laboratory, 1994).

[60] Emery, K. A. Solar simulators and I-V measurement methods. *Solar Cells* **18**, 251–260 (1986).

[61] Osterwald, C. R. Translation of device performance measurements to reference conditions. *Solar Cells* **18**, 269–279 (1986).

[62] Shrotriya, V. *et al.* Accurate measurement and characterization of organic solar cells. *Advanced Functional Materials* **16**, 2016–2023 (2006).

[63] Zhang, Y., Ye, L. & Hou, J. Precise characterization of performance metrics of organic solar cells. *Small Methods* **1**, 1700159 (2017).

[64] McGhie, A. R., Garito, A. F. & Heeger, A. J. A gradient sublimer for purification and crystal growth of organic donor and acceptor molecules. *Journal of Crystal Growth* **22**, 295–297 (1974).

[65] Wang, N. *et al.* Snow cleaning of substrates increases yield of large-area organic photovoltaics. *Applied Physics Letters* **101**, 133901 (2012).

[66] Sugiyama, K., Ishii, H., Ouchi, Y. & Seki, K. Dependence of indium-tin-oxide work function on surface cleaning method as studied by ultraviolet and x-ray photoemission spectroscopies. *Journal of Applied Physics* **87**, 295–298 (2000).

[67] Cheyns, D., Kim, M., Verreet, B. & Rand, B. P. Accurate spectral response measurements of a complementary absorbing organic tandem cell with fill factor exceeding the subcells. *Applied Physics Letters* **104**, 093302 (2014).

[68] Ting, H.-C. *et al.* Benzochalcogenodiazole-based donor-acceptor-acceptor molecular donors for organic solar cells. *ChemSusChem* **7**, 457–465 (2014).

[69] Griffith, O. L. *et al.* Charge transport and exciton dissociation in organic solar cells consisting of dipolar donors mixed with C_{70}. *Physical Review B* **92**, 085404 (2015).

[70] Olthof, S. *et al.* Ultralow doping in organic semiconductors: Evidence of trap filling. *Physical Review Letters* **109**, 176601 (2012).

[71] Jarrett, C. P., Pichler, K., Newbould, R. & Friend, R. H. Transport studies in C_{60} and C_{60}/C_{70} thin films using metal-insulator-semiconductor field-effect transistors. *Synthetic Metals* **77**, 35–38 (1996).

[72] Haddon, R. C. C_{70} thin film transistors. *Journal of the American Chemical Society* **118**, 3041–3042 (1996).

[73] Itaka, K. *et al.* High-mobility C_{60} field-effect transistors fabricated on molecular-wetting controlled substrates. *Advanced Materials* **18**, 1713–1716 (2006).

[74] Anthopoulos, T. D. *et al.* High performance *n*-channel organic field-effect transistors and ring oscillators based on C_{60} fullerene films. *Applied Physics Letters* **89**, 213504 (2006).

[75] Jurchescu, O., Popinciuc, M., van Wees, B. & Palstra, T. Interface-controlled, high-mobility organic transistors. *Advanced Materials* **19**, 688–692 (2007).

[76] Sakanoue, T. & Sirringhaus, H. Band-like temperature dependence of mobility in a solution-processed organic semiconductor. *Nature Materials* **9**, 736740 (2010).

[77] Leijtens, T., Lim, J., Teuscher, J., Park, T. & Snaith, H. J. Charge density dependent mobility of organic hole-transporters and mesoporous TiO_2 determined by transient mobility spectroscopy: Implications to dye-sensitized and organic solar cells. *Advanced Materials* **25**, 3227–3233 (2013).

[78] Tummala, N. R., Zheng, Z., Aziz, S. G., Coropceanu, V. & Brédas, J.-L. Static and dynamic energetic sisorders in the C_{60}, $PC_{61}BM$, C_{70}, and $PC_{71}BM$ fullerenes. *The Journal of Physical Chemistry Letters* **6**, 3657–3662 (2015).

[79] Mateker, W. R. & McGehee, M. D. Progress in understanding degradation mechanisms and improving stability in organic photovoltaics. *Advanced Materials* **29**, 1603940 (2017).

[80] Gevorgyan, S. A. *et al.* Lifetime of organic photovoltaics: Status and predictions. *Advanced Energy Materials* **6**, 1501208 (2016).

[81] Burlingame, Q. *et al.* Reliability of small molecule organic photovoltaics with electron-filtering compound buffer layers. *Advanced Energy Materials* **6**, 1601094 (2016).

[82] Roesch, R. *et al.* Procedures and practices for evaluating thin-film solar cell stability. *Advanced Energy Materials* **5**, 1501407 (2015).

[83] Jordan, D. C. & Kurtz, S. R. Photovoltaic degradation rates–an analytical review. *Progress in Photovoltaics: Research and Applications* **21**, 12–29 (2013).

[84] Mateker, W. R. *et al.* Molecular packing and arrangement govern the photo-oxidative stability of organic photovoltaic materials. *Chemistry of Materials* **27**, 6345–6353 (2015).

[85] Curtin, I. J., Blaylock, D. W. & Holmes, R. J. Role of impurities in determining the exciton diffusion length in organic semiconductors. *Applied Physics Letters* **108**, 163301 (2016).

[86] Salzman, R. F. *et al.* The effects of copper phthalocyanine purity on organic solar cell performance. *Organic Electronics* **6**, 242–246 (2005).

[87] Song, B. S., Burlingame, Q., Lee, K. & Forrest, S. R. Reliability of mixed-heterojunction organic photovoltaics grown *via* organic vapor phase deposition. *Advanced Energy Materials* **5**, 1401952 (2015).

[88] Che, X., Xiao, X., Zimmerman, J. D., Fan, D. & Forrest, S. R. High-efficiency, vacuum-deposited, small-molecule organic tandem and triple-junction photovoltaic cells. *Advanced Energy Materials* **4**, 1400568 (2014).

[89] Franke, R., Maennig, B., Petrich, A. & Pfeiffer, M. Long-term stability of tandem solar cells containing small organic molecules. *Solar Energy Materials and Solar Cells* **92**, 732–735 (2008).

[90] Wang, L. *et al.* Correlation of the π-conjugation chain length and the property and photovoltaic performance of benzo[1,2-b:4,5-b']dithiophene-cored A-π-D-π-A type molecules. *Solar Energy Materials and Solar Cells* **157**, 831–843 (2016).

[91] Yamane, S. *et al.* Relationship between photostability and nanostructures in DTS($FBTTh_2$)$_2$:fullerene bulk-heterojunction films. *Solar Energy Materials and Solar Cells* **151**, 96–101 (2016).

[92] Jeon, I., Sakai, R., Nakagawa, T., Setoguchi, H. & Matsuo, Y. Stability of diketopyrrolopyrrole small-molecule inverted organic solar cells. *Organic Electronics* **35**, 193–198 (2016).

[93] Long, G. *et al.* Enhancement of performance and mechanism studies of all-solution processed small-molecule based solar cells with an inverted structure. *ACS Applied Materials & Interfaces* **7**, 21245–21253 (2015).

[94] Song, Q. L. *et al.* Degradation of small-molecule organic solar cells. *Applied Physics Letters* **89**, 251118 (2006).

[95] Xi, X. *et al.* A comparative study on the performances of small molecule organic solar cells based on CuPc/C_{60} and CuPc/C_{70}. *Solar Energy Materials and Solar Cells* **94**, 2435–2441 (2010).

[96] Lessmann, R. *et al.* Aging of flat heterojunction zinc phthalocyanine/fullerene C_{60} organic solar cells. *Organic Electronics* **11**, 539–543 (2010).

[97] Hermenau, M. *et al.* The effect of barrier performance on the lifetime of small-molecule organic solar cells. *Solar Energy Materials and Solar Cells* **97**, 102–108 (2012).

[98] Liu, S.-W. *et al.* Improving performance and lifetime of small-molecule organic photovoltaic devices by using bathocuproine–fullerene cathodic layer. *ACS Applied Materials & Interfaces* **7**, 9262–9273 (2015).

[99] Heumueller, T. *et al.* Morphological and electrical control of fullerene dimerization determines organic photovoltaic stability. *Energy & Environental Science* **9**, 247–256 (2016).

[100] Tong, X., Wang, N., Slootsky, M., Yu, J. & Forrest, S. R. Intrinsic burn-in efficiency loss of small-molecule organic photovoltaic cells due to exciton-induced trap formation. *Solar Energy Materials and Solar Cells* **118**, 116–123 (2013).

[101] Wang, N., Tong, X., Burlingame, Q., Yu, J. & Forrest, S. R. Photodegradation of small-molecule organic photovoltaics. *Solar Energy Materials and Solar Cells* **125**, 170–175 (2014).

[102] Burlingame, Q. *et al.* Photochemical origins of burn-in degradation in small molecular weight organic photovoltaic cells. *Energy & Environmental Science* **8**, 1005–1010 (2015).

[103] Badgujar, S. *et al.* Highly efficient and thermally stable fullerene-free organic solar cells based on a small molecule donor and acceptor. *Journal of Materials Chemistry A* **4**, 16335–16340 (2016).

[104] Holliday, S. *et al.* High-efficiency and air-stable P3HT-based polymer solar cells with a new non-fullerene acceptor. *Nature Communications* **7**, 11585 (2016).

[105] Gasparini, N. *et al.* Burn-in free nonfullerene-based organic solar cells. *Advanced Energy Materials* **7**, 1700770 (2017).

[106] Li, N. *et al.* Abnormal strong burn-in degradation of highly efficient polymer solar cells caused by spinodal donor-acceptor demixing. *Nature Communications* **8**, 14541 (2017).

[107] Li, N., McCulloch, I. & Brabec, C. J. Analyzing the efficiency, stability and cost potential for fullerene-free organic photovoltaics in one figure of merit. *Energy & Environmental Science* **11**, 1355–1361 (2018).

[108] Reese, M. O. *et al.* Consensus stability testing protocols for organic photovoltaic materials and devices. *Solar Energy Materials and Solar Cells* **95**, 1253–1267 (2011).

[109] Kawano, K. *et al.* Degradation of organic solar cells due to air exposure. *Solar Energy Materials and Solar Cells* **90**, 3520–3530 (2006).

[110] Peters, C. H. *et al.* High efficiency polymer solar cells with long operating lifetimes. *Advanced Energy Materials* **1**, 491–494 (2011).

[111] Hermenau, M. *et al.* Water and oxygen induced degradation of small molecule organic solar cells. *Solar Energy Materials and Solar Cells* **95**, 1268–1277 (2011).

[112] Teran-Escobar, G. *et al.* On the stability of a variety of organic photovoltaic devices by IPCE and *in situ* IPCE analyses - the ISOS-3 inter-laboratory collaboration. *Physical Chemistry Chemical Physics* 11824–11845 (2012).

[113] Roesch, R., Eberhardt, K.-R., Engmann, S., Gobsch, G. & Hoppe, H. Polymer solar cells with enhanced lifetime by improved electrode stability and sealing. *Solar Energy Materials and Solar Cells* **117**, 59–66 (2013).

[114] Sapkota, S. B., Spies, A., Zimmermann, B., Dürr, I. & Würfel, U. Promising long-term stability of encapsulated ITO-free bulk-heterojunction organic solar cells under different aging conditions. *Solar Energy Materials and Solar Cells* **130**, 144–150 (2014).

[115] Williams, G. & Aziz, H. Implications of the device structure on the photostability of organic solar cells. *Solar Energy Materials and Solar Cells* **128**, 320–329 (2014).

[116] Hauch, J. A. *et al.* Flexible organic P3HT:PCBM bulk-heterojunction modules with more than 1 year outdoor lifetime. *Solar Energy Materials and Solar Cells* **92**, 727–731 (2008).

[117] Gevorgyan, S. A. *et al.* Interlaboratory outdoor stability studies of flexible roll-to-roll coated organic photovoltaic modules: Stability over 10,000h. *Solar Energy Materials and Solar Cells* **116**, 187–196 (2013).

[118] Corazza, M., Krebs, F. C. & Gevorgyan, S. A. Lifetime of organic photovoltaics: Linking outdoor and indoor tests. *Solar Energy Materials and Solar Cells* **143**, 467–472 (2015).

[119] Ciammaruchi, L. *et al.* Stability of organic solar cells with PCDTBT donor polymer: An interlaboratory study. *Journal of Materials Research* **33**, 19091924 (2018).

[120] Haillant, O., Dumbleton, D. & Zielnik, A. An Arrhenius approach to estimating organic photovoltaic module weathering acceleration factors. *Solar Energy Materials and Solar Cells* **95**, 1889–1895 (2011).

[121] Eklund, P. C., Rao, A. M., Zhou, P., Wang, Y. & Holden, J. M. Photochemical transformation of C_{60} and C_{70} films. *Thin Solid Films* **257**, 185–203 (1995).

[122] Zhang, H. *et al.* Photochemical transformations in fullerene and molybdenum oxide affect the stability of bilayer organic solar cells. *Advanced Energy Materials* **5**, 1400734 (2014).

[123] Baldo, M. A., Adachi, C. & Forrest, S. R. Transient analysis of organic electrophosphorescence. II. transient analysis of triplet-triplet annihilation. *Physical Review B* **62**, 10967–10977 (2000).

[124] Tzabari, L., Zayats, V. & Tessler, N. Exciton annihilation as bimolecular loss in organic solar cells. *Journal of Applied Physics* **114**, 154514 (2013).

[125] Gärtner, C., Karnutsch, C., Lemmer, U. & Pflumm, C. The influence of annihilation processes on the threshold current density of organic laser diodes. *Journal of Applied Physics* **101**, 023107 (2007).

[126] Gordon, J. M., Katz, E. A., Feuermann, D. & Huleihil, M. Toward ultrahigh-flux photovoltaic concentration. *Applied Physics Letters* **84**, 3642–3644 (2004).

[127] Visoly-Fisher, I. *et al.* Concentrated sunlight for accelerated stability testing of organic photovoltaic materials: Towards decoupling light intensity and temperature. *Solar Energy Materials and Solar Cells* **134**, 99–107 (2015).

[128] Katz, E. A., Gordon, J. M., Tassew, W. & Feuermann, D. Photovoltaic characterization of concentrator solar cells by localized irradiation. *Journal of Applied Physics* **100**, 044514 (2006).

[129] Katz, E. A. *et al.* Temperature dependence for the photovoltaic device parameters of polymer-fullerene solar cells under operating conditions. *Journal of Applied Physics* **90**, 5343–5350 (2001).

[130] Burlingame, Q., Zanotti, G., Ciammaruchi, L., Katz, E. A. & Forrest, S. R. Outdoor operation of small-molecule organic photovoltaics. *Organic Electronics* **41**, 274–279 (2017).

[131] Rao, A. M. *et al.* Photoinduced polymerization of solid C_{60} films. *Science* **259**, 955–957 (1993).

[132] Neugebauer, J., Reiher, M., Kind, C. & Hess, B. A. Quantum chemical calculation of vibrational spectra of large molecules—Raman and IR spectra for Buckminsterfullerene. *Journal of Computational Chemistry* **23**, 895–910 (2002).

[133] Kuhnke, K., Becker, R., Epple, M. & Kern, K. C_{60} exciton quenching near metal surfaces. *Physical Review Letters* **79**, 3246–3249 (1997).

[134] Fujitsuka, M., Luo, C., Ito, O., Murata, Y. & Komatsu, K. Triplet properties and photoinduced electron-transfer reactions of C_{120}, the [2+2] dimer of fulllerene C_{60}. *The Journal of Physical Chemistry A* **103**, 7155–7160 (1999).

[135] Fujitsuka, M. *et al.* Properties of photoexcited states of C_{180}, a triangle trimer of C_{60}. *Chemistry Letters* **30**, 384–385 (2001).

[136] Bachilo, S. M., Benedetto, A. F. & Weisman, R. B. Triplet state dissociation of C_{120}, the dimer of C_{60}. *The Journal of Physical Chemistry A* **105**, 9845–9850 (2001).

[137] Pettersson, L. A. A., Roman, L. S. & Inganäs, O. Modeling photocurrent action spectra of photovoltaic devices based on organic thin films. *Journal of Applied Physics* **86**, 487–496 (1999).

[138] Luhman, W. A. & Holmes, R. J. Investigation of energy transfer in organic photovoltaic cells and impact on exciton diffusion length measurements. *Advanced Functional Materials* **21**, 764–771 (2011).

[139] Lunt, R. R., Giebink, N. C., Belak, A. A., Benziger, J. B. & Forrest, S. R. Exciton diffusion lengths of organic semiconductor thin films measured by spectrally resolved photoluminescence quenching. *Journal of Applied Physics* **105**, 053711 (2009).

[140] Kim, T.-M., Whan Kim, J., Shim, H.-S. & Kim, J.-J. High efficiency and high photo-stability zinc-phthalocyanine based planar heterojunction solar cells with a double interfacial layer. *Applied Physics Letters* **101**, 113301 (2012).

[141] Wu, H. R. *et al.* Stable small-molecule organic solar cells with 1,3,5-tris(2-*N*-phenylbenzimidazolyl) benzene as an organic buffer. *Thin Solid Films* **515**, 8050–8053 (2007).

[142] Wang, N., Yu, J., Zang, Y., Huang, J. & Jiang, Y. Effect of buffer layers on the performance of organic photovoltaic cells based on copper phthalocyanine and C_{60}. *Solar Energy Materials and Solar Cells* **94**, 263–266 (2010).

[143] Bhugra, C. & Pikal, M. J. Role of thermodynamic, molecular, and kinetic factors in crystallization from the amorphous state. *Journal of Pharmaceutical Sciences* **97**, 1329–1349 (2008).

[144] Andronis, V. & Zografi, G. Crystal nucleation and growth of indomethacin polymorphs from the amorphous state. *Journal of Non-Crystalline Solids* **271**, 236–248 (2000).

[145] Hoffman, J. D. Thermodynamic driving force in nucleation and growth processes. *The Journal of Chemical Physics* **29**, 1192–1193 (1958).

[146] Zhao, Y. *et al.* Trifluoromethyl-functionalized bathocuproine for polymer solar cells. *Journal of Materials Chemistry C* **4**, 4640–4646 (2016).

[147] Xiao, X., Zimmerman, J. D., Lassiter, B. E., Bergemann, K. J. & Forrest, S. R. A hybrid planar-mixed tetraphenyldibenzoperiflanthene/C_{70} photovoltaic cell. *Applied Physics Letters* **102**, 073302 (2013).

[148] Graff, G. L., Williford, R. E. & Burrows, P. E. Mechanisms of vapor permeation through multilayer barrier films: Lag time versus equilibrium permeation. *Journal of Applied Physics* **96**, 1840–1849 (2004).

[149] Bartesaghi, D. *et al.* Competition between recombination and extraction of free charges determines the fill factor of organic solar cells. *Nature Communications* **6**, 7083 (2015).

[150] Lee, S. J., Kim, B. S., Kim, J.-Y., Yusoff, A. & Jang, J. Stable organic photovoltaic with PEDOT:PSS and MoO_x mixture anode interfacial layer without encapsulation. *Organic Electronics* **19**, 140–146 (2015).

[151] D'Andrade, B. W., Forrest, S. R. & Chwang, A. B. Operational stability of electrophosphorescent devices containing *p* and *n* doped transport layers. *Applied Physics Letters* **83**, 3858–3860 (2003).

[152] Chen, S.-Y., Chu, T.-Y., Chen, J.-F., Su, C.-Y. & Chen, C. H. Stable inverted bottom-emitting organic electroluminescent devices with molecular doping and morphology improvement. *Applied Physics Letters* **89**, 053518 (2006).

[153] Bristow, N. & Kettle, J. Outdoor performance of organic photovoltaics: Diurnal analysis, dependence on temperature, irradiance, and degradation. *Journal of Renewable and Sustainable Energy* **7**, 013111 (2015).

[154] Lakhwani, G., Rao, A. & Friend, R. H. Bimolecular recombination in organic photovoltaics. *Annual Review of Physical Chemistry* **65**, 557–581 (2014).

[155] Elumalai, N. K. & Uddin, A. Open circuit voltage of organic solar cells: An in-depth review. *Energy & Environmental Science* **9**, 391–410 (2016).

[156] Tromholt, T., Katz, E. A., Hirsch, B., Vossier, A. & Krebs, F. C. Effects of concentrated sunlight on organic photovoltaics. *Applied Physics Letters* **96**, 073501 (2010).

[157] Thakur, A. K., Wantz, G., Garcia-Belmonte, G., Bisquert, J. & Hirsch, L. Temperature dependence of open-circuit voltage and recombination processes in polymer-fullerene based solar cells. *Solar Energy Materials and Solar Cells* **95**, 2131–2135 (2011).

[158] Malik, A. Q. & Damit, S. J. B. H. Outdoor testing of single crystal silicon solar cells. *Renewable Energy* **28**, 1433–1445 (2003).

[159] Gottschalg, R., Betts, T. R., Infield, D. G. & Kearney, M. J. The effect of spectral variations on the performance parameters of single and double junction amorphous silicon solar cells. *Solar Energy Materials and Solar Cells* **85**, 415–428 (2005).

[160] Manor, A., Katz, E. A., Tromholt, T., Hirsch, B. & Krebs, F. C. Origin of size effect on efficiency of organic photovoltaics. *Journal of Applied Physics* **109**, 074508 (2011).

[161] Koster, L. J. A., Mihailetchi, V. D. & Blom, P. W. M. Bimolecular recombination in polymer/fullerene bulk heterojunction solar cells. *Applied Physics Letters* **88** (2006).

[162] Riedel, I. *et al.* Effect of temperature and illumination on the electrical characteristics of polymer-fullerene bulk-heterojunction solar cells. *Advanced Functional Materials* **14**, 38–44 (2004).

[163] Hörmann, U. *et al.* Quantification of energy losses in organic solar cells from temperature-dependent device characteristics. *Physical Review B* **88**, 235307 (2013).

[164] Mihailetchi, V. D. *et al.* Electron transport in a methanofullerene. *Advanced Functional Materials* **13**, 43–46 (2003).

[165] Huang, K. & Rhys, A. Theory of light absorption and non-radiative transitions in F-centres. *Proceedings of the Royal Society of London A: Mathematical, Physical and Engineering Sciences* **204**, 406–423 (1950).

[166] Lautenschlager, P., Garriga, M., Logothetidis, S. & Cardona, M. Interband critical points of GaAs and their temperature dependence. *Physical Review B* **35**, 9174–9189 (1987).

[167] Viña, L., Logothetidis, S. & Cardona, M. Temperature dependence of the dielectric function of germanium. *Physical Review B* **30**, 1979–1991 (1984).

[168] O'Donnell, K. P. & Chen, X. Temperature dependence of semiconductor band gaps. *Applied Physics Letters* **58**, 2924–2926 (1991).

[169] Böer, K. W. The solar spectrum at typical clear weather days. *Solar Energy* **19**, 525–538 (1977).

[170] Liu, X., Ding, K., Panda, A. & Forrest, S. R. Charge transfer states in dilute donor-acceptor blend organic heterojunctions. *ACS Nano* **10**, 7619–7626 (2016).

[171] Durbin, S. M. & Gray, J. L. Numerical modeling of photon recycling in solar cells. *IEEE Transactions on Electron Devices* **41**, 239–245 (1994).

[172] Miller, O. D., Yablonovitch, E. & Kurtz, S. R. Strong internal and external luminescence as solar cells approach the Shockley-Queisser limit. *IEEE Journal of Photovoltaics* **2**, 303–311 (2012).

[173] Rau, U. Reciprocity relation between photovoltaic quantum efficiency and electroluminescent emission of solar cells. *Physical Review B* **76**, 085303 (2007).

[174] Kirchartz, T. & Rau, U. Detailed balance and reciprocity in solar cells. *Physica Status Solidi A* **205**, 2737–2751 (2008).

[175] Vandewal, K., Tvingstedt, K., Gadisa, A., Inganäs, O. & Manca, J. V. On the origin of the open-circuit voltage of polymer-fullerene solar cells. *Nature Materials* **8**, 904–909 (2009).

[176] Du, X. *et al.* Efficient polymer solar cells based on non-fullerene acceptors with potential device lifetime approaching 10 years. *Joule* (2018).

[177] Song, Q. L. *et al.* Small-molecule organic solar cells with improved stability. *Chemical Physics Letters* **416**, 42–46 (2005).

[178] Williams, G. & Aziz, H. The effect of charge extraction layers on the photostability of vacuum-deposited versus solution-coated organic solar cells. *Organic Electronics* **15**, 47–56 (2014).

[179] Min, J. *et al.* Interface design to improve the performance and stability of solution-processed small-molecule conventional solar cells. *Advanced Energy Materials* **4**, 1400816 (2014).

[180] Klumbies, H. *et al.* Water ingress into and climate dependent lifetime of organic photovoltaic cells investigated by calcium corrosion tests. *Solar Energy Materials and Solar Cells* **120**, 685–690 (2014).

[181] Hao, X., Wang, S., Sakurai, T., Masuda, S. & Akimoto, K. Improvement of stability for small molecule organic solar cells by suppressing the trap mediated recombination. *ACS Applied Materials & Interfaces* **7**, 18379–18386 (2015).

[182] Cheacharoen, R. *et al.* Assessing the stability of high performance solution processed small molecule solar cells. *Solar Energy Materials and Solar Cells* **161**, 368–376 (2017).

[183] Lanzi, M., Salatelli, E., Di-Nicola, F. P., Zuppiroli, L. & Pierini, F. A new photocrosslinkable oligothiophene for organic solar cells with enhanced stability. *Materials Chemistry and Physics* **186**, 98–107 (2017).

[184] Lee, K. C. *et al.* Influence of the crystalline nature of small donors molecules on the efficiency and stability of organic photovoltaic devices. *Solar RRL* **2**, 1700235 (2018).

[185] Lee, J. S. *et al.* Hot excited state management for long-lived blue phosphorescent organic light-emitting diodes. *Nature Communications* **8**, 15566 (2017).

[186] Shockley, W. & Queisser, H. J. Detailed balance limit of efficiency of *p-n* junction solar sells. *Journal of Applied Physics* **32**, 510–519 (1961).

[187] Rühle, S. Tabulated values of the Shockley-Queisser limit for single junction solar cells. *Solar Energy* **130**, 139–147 (2016).

[188] Giebink, N. C., Wiederrecht, P., G, Wasielewski, R., M & Forrest, R., S. Thermodynamic efficiency limit of excitonic solar cells. *Physical Review B* **83**, 195326 (2011).

[189] Baran, D. *et al.* Robust nonfullerene solar cells approaching unity external quantum efficiency enabled by suppression of geminate recombination. *Nature Communications* **9**, 2059 (2018).

[190] Xia, S. C., Kwong, R. C., Adamovich, V. I., Weaver, M. S. & Brown, J. J. Oled device operational lifetime: Insights and challenges. In *2007 IEEE International Reliability Physics Symposium Proceedings. 45th Annual*, 253–257 (2007).

[191] Campoy-Quiles, M., Kanai, Y., El-Basaty, A., Sakai, H. & Murata, H. Ternary mixing: A simple method to tailor the morphology of organic solar cells. *Organic Electronics* **10**, 1120–1132 (2009).

[192] Lee, K., Zimmerman, J. D., Hughes, T. W. & Forrest, S. R. Non-destructive wafer recycling for low-cost thin-film flexible optoelectronics. *Advanced Functional Materials* **24**, 4284–4291 (2014).